A Detailed Approach to Model Transport, Heterogeneous Chemistry, and Electrochemistry in Solid-Oxide Fuel Cells

Zur Erlangung des akademischen Grades eines

Doktors der Ingenieurwissenschaften (Dr.-Ing.)

von der Fakultät für Chemieingenieurwesen und
Verfahrenstechnik
der Universität Karlsruhe (TH)

eingereichte

Dissertation

von

Vinod M. Janardhanan, M.Tech
aus Kerala, Indien

Referent : Prof. Dr. Olaf Deutschmann
Korreferent : Prof. Dr.-Ing. Rainer Reimert

Tag des Kolloquiums 27.06.2007

A journey of a thousand miles begins with a single step
Lao Tzu

Acknowledgments

First and foremost, I am deeply indebted to my Prof. Dr. Olaf Deutschmann. His willingness to support my work and his guidance throughout my studies has allowed me to develop my skills as a researcher within a supportive team environment. I thank him for that opportunity. Also, I am highly obliged to Prof. Dr.-Ing. Rainer Reimert for being my co-mentor and for his fruitful advices throughout the course of preparing this thesis. Special thanks to Prof. Robert J. Kee and Dr. Huayang Zhu (Colorado School of Mines,Golden, USA) for the continuous support, advice, and discussions throughout the work. I also thank Dr. Wolfgang Bessler (University of Heidelberg, Germany) for the encouraging discussions.

I am highly indebted to the Department of Chemical Engineering for accepting me as a PhD student, even though the work is carried out at the Institute of Chemical Technology and Polymer Chemistry.

I would further like to thank the other members of my committee: Prof. Dr.-Ing. M. Kind, Prof. Dr.-Ing. H. Nirschl, and Prof. Dr.-Ing. M. Türk.

Within our research group, I owe many thanks to my colleagues. Specially, I thank Dr. Steffen Tischer for timely help and advices throughout the course of my work. I gratefully acknowledge Benjamin Schädel for translating the abstract in German. I thank Dr. Günter Schoch for proof reading my thesis. I am highly grateful to Nikolay Mladenov for the timely help in many circumstances. I also thank Dr. Renate Schwiedernoch for the discussions that have always motivated my work. I express my sincerest gratitude for the many conversations with my colleagues that have had a tremendous impact on my research and myself as a person. Minh, Luba, Nam, Aijun, Lothar, Jan, Nicole, Marco, Sven and Paolo thank you so much for creating a highly supportive work environment. My highest appreciation to Mrs. Cariboni for the constant help and affection throughout my stay in Germany. I am also grateful to my previous colleagues Dr. Hans-Heinrich Carstensen and Dr. Koyo Norinaga for many discussions. I highly appreciate the help and support of Stefan Kleditsch (Fluent, Germany) and Grahm Goldin (Fluent, NH).

My friends Siddu, Ayan, and Motte thanks for the joyful moments. Last but not the least I gratefully acknowledge my friends back in India, Anish and Rekha Chechi thank you so much for the encouragement during the bad times. Anil and Suresh I owe you for the tips on C++.

Abstract

This dissertation layes out detailed descriptions for heterogeneous chemistry, electrochemistry, and porous media transport models to simulate solid oxide fuel cells (SOFCs). An elementary like heterogeneous reaction mechanism for the steam reforming of CH_4 developed in our research group is used throughout this work. Based on assumption of hydrogen oxidation as the only electrochemical reaction and single step electron transfer reaction as rate limiting, a modified Butler-Volmer equation is used to model the electrochemistry. The pertinence of various porous media transport models such as Modified Fick Model (MFM), Dusty Gas Model (DGM), Mean Transport Pore Model (MTPM), Modified Maxwell Stefan Model (MMS), and Generalized Maxwell Stefan Model (GMS) under reaction conditions are studied. All model predictions are compared with experimental observations. In general MFM and DGM predictions are in good agreement with experimental data.

Physically realistic electrochemical model parameters are very important for fuel cell modeling. Button cell simulations are carried out to deduce the electrochemical model parameters, and those parameters are further used in the modeling of planar cells. Button cell simulations are carried out using the commercial CFD code FLUENT [1] coupled with DETCHEM [2]. For all temperature ranges the model works well in predicting the experimental observations in the high current density region. However, the model predicts much higher open circuit potentials than that observed in the experiments, mainly due to the absence of coking model in the elementary heterogeneous mechanism leading to non-equilibrium compositions. Furthermore, the study presented here employs Nernst equation for the calculation of reversible potential which is strictly valid only for electrochemical equilibrium. It is assumed that the electrochemical charge transfer reaction involving H_2 is fast enough to be in equilibrium. However, the comparison of model prediction with thermodynamic equilibrium reveals that this assumption is violated under very low current densities. The planar cell simulations are carried out for both isothermal as well as for adiabatic operating conditions. The influence of various operating and geometrical parameters, such as air flow rate, steam to carbon ratio (s/c) in the inlet fuel, extent of pre-reforming, anode thickness, and specific surface area of the catalyst on the cell performance is studied systematically. In certain cases adiabatic and isothermal operations lead to strikingly different results in efficiency and power density. Isothermal operation results in increased efficiency

with increasing air flow rate, while adiabatic operation results in decreased efficiency with increasing air flow rate. Increasing the anode thickness and specific surface area of the catalyst beyond certain limits leads to decreased efficiency and power density in the case of adiabatic operation, while isothermal operation results in increased efficiency and power density with increasing anode thickness and specific catalyst area.

Contents

Nomenclature

a_i	Pre-exponential constant in sticking coefficient expression
A_c	Area of cross section of flow channels (m^2)
A_{H_2}	Pre-exponential for H_2 desorption (cm^2/s mol)
A_i	Pre-exponential constant in Arrhenius expression (varies)
A_{O_2}	Pre-exponential for O_2 desorption (cm^2/s mol)
A_s	Specific area (1/m)
b_i	Temperature exponent in sticking coefficient expression
B_g	Permeability (m^2)
C_p	Specific heat (J/kg K)
d_p	Particle diameter (m)
$\mathcal{D}$	Diffusivity (m^2/s)
$\mathcal{D}_{\text{eff}}$	Effective Fickian diffusivity (m^2/s)
D_h	Hydraulic diameter (m)
$\mathscr{D}_{kj}$	Binary diffusivity species k in j (m^2/s)
$\mathcal{D}_{k,kn}$	Knudsen diffusivity (m^2/s)
$\mathcal{D}^{\text{e}}_{k,kn}$	Effective Knudsen diffusivity (m^2/s)
$\mathcal{D}_{km}$	Mixture diffusivity of species k in the mixture (m^2/s)
$\mathcal{D}^{\text{e}}_{km}$	Effective mixture diffusivity of species k in the mixture (m^2/s)
e	Emissivity
E_{ai}	Activation energy for reaction i (kJ/mol)
E_{cell}	Cell voltage (V)
E_{e}	Activation energy for ion transport (kJ/mol)
E^{eq}	Equilibrium potential (V)
E^{act}_f	Activation energy for the forward reaction (kJ/mol)
E_{H_2}	Activation energy for H_2 oxidation (kJ/mol)
$E^{\text{des}}_{H_2}$	Desorption energy for H_2 (kJ/mol)
E_{O_2}	Activation energy for O_2 reduction (kJ/mol)
$E^{\text{des}}_{O_2}$	Desorption energy for O_2 (kJ/mol)
E^{act}_r	Activation energy for the reverse reaction (kJ/mol)
E_{rev}	Reversible potential (V)
E_{th}	Thermoneutral voltage (V)
F	Faraday constant (C/mol)
Gz	Graetz number
ΔG^0	Standard Gibb's free energy change (kJ/mol)
h	Heat transfer coefficient (J/m^2s K)
h	Specific enthalpy (J/kg)
H_c	Channel height (m)

H_I	Thickness of interconnect (m)
H^0	Standard state enthalpy (J/mol)
ΔH	Enthalpy change (J/mol)
i	Current density (A/m^2)
i_0	Exchange current density (A/m^2)
J_k	Total flux of species k (mol/m^{2}s)
J_k^d	Flux due to diffusive transport for species k (mol/m^{2}s)
J_k^p	Flux due to viscous transport for species k (mol/m^{2}s)
k	Thermal conductivity (J/m s K)
k_{eff}	Effective thermal conductivity (J/m s K)
k_f	Forward rate constant (varies)
k_r	Reverse rate constant (varies)
k_B	Boltzmann's constant (J/K)
K_b	Total number of bulk species
K_c	Equilibrium constant in concentration units for reaction i (varies)
K_g	Total number of gas-phase species
K_p	Equilibrium constant in pressure units for reaction i
K_s	Total number of surface species
Kn	Knudsen number
l	Thickness (m)
L	Length (m)
M	Mass of molecule (Kg)
$\bar{M}$	Average molecular weight (kg/mol)
n_{e}	Number of electrons transferred in the electrochemical reaction
n_t^{s}	Total surface concentration (mol/m^2)
$\dot{n}$	Molar flow rate (mol/s)
N	Number of molecules
N_a	Avogadro number
Nu	Nusselt number
p	Pressure (Pa)
p^0	Standard state pressure (pa)
p_k	Partial pressure of species k (Pa)
p^*	Pressure term appearing in exchange current density formulation (Pa)
P_{e}	Electrochemically active perimeter (m)
Pr	Prandtl number
Q_e	Electrochemical heat source (J/m^{3}s)
Q_h	Convective heat source (J/m^{3}s)
Q_r	Radiative heat source (J/m^{3}s)
r_p	Particle radius (m)
R	Gas constant (J/mol K)
Re	Reynolds number
R_{tot}	Total area specific resistance (Ω m^2)
R_{contact}	Contact resistance (Ω m^2)
$\dot{s}_k$	Molar production rate of species k due to surface reaction (mol/m^{2}s^{-1})
S^0	Sticking coefficient

S^0	Standard state entropy (J/K)
ΔS	Entropy change (J/K)
t	time (s)
T	Temperature (K)
T^0	Reference temperature (K)
T_f	Fluid temperature (K)
T_I	Interconnect temperature (K)
u	Velocity (m/s)
$\vec{u}$	Velocity vector (m/s)
v	Diffusion velocity (m/s)
v_k	Axial diffusion velocity for species k (m/s)
v^*	Molar average velocity (m/s)
V	Volume (m^3)
W	Width of MEA (m)
W_k	Molecular weight of species k (kg/mol)
W^*	Reduced molar mass (kg/mol)
X_k	Mole fraction of species k
$[X]$	Concentration (mol/m^3) for gaseous species, (mol/m^2) for surface species
y	Co-ordinate direction
Y_k	Mass fraction of species k
z	Co-ordinate direction
Z	Rate of collision (mol/m^2 s)

Greek symbols

α_a	Anode charge transfer coefficient
α_c	Cathode charge transfer coefficient
β	Temperature exponent in Arrhenius expression
β_a	Anodic charge transfer coefficient
β_c	Cathodic charge transfer coefficient
δ	Kronecker symbol
δy	Discretization distance (m)
ϵ	Porosity
ϵ_{ki}	Parameter modeling coverage dependent activation energy in the rate constant expression for species k in the i'th reaction
η_a	Anode activation overpotential (V)
η_c	Cathode activation overpotential (V)
η	Net efficiency
η_{th}	Thermodynamic efficiency
η_{u}	Fuel utilization
η_{v}	Voltage efficiency
θ	surface coverage
λ	Air number
λ_{km}	Mean free path of species k in the mixture (m)
μ	Viscosity (Kg/m s)

μ_{ki}	Parameter modeling surface coverage in the rate constant expression for species k in the i'th reaction
μ	Chemical potential (J/mol)
ν'	Stoichiometric coefficient of reactants
ν''	Stoichiometric coefficient of products
ξ	Solution vector for variables in the electrochemistry model equations
ρ	Density (kg/m^3)
ρ	Resistivity (Ω m)
σ	Collision diameter (m)
σ_e	Electrolyte conductivity (S/m)
σ_0	Standard electrolyte conductivity (S/m)
σ	Standard deviation
σ_k	Co-ordination number for species k
τ	Tortuosity
ϕ	Potential (V)
Φ	Potential (V)
χ	Species Symbol
ψ	Solution vector for flow variables
ω	Parameter for wall slip
Γ	Surface site density (mol/m^2)

Subscripts

a	Anode
b	bulk species
c	Cathode
c	Channel
e	Electrolyte
e	Electrochemical
f	Fluid
g	gas-phase species
h	Convection
i	Reaction index
I	Interconnect
k	Species index
r	Radiation

Superscripts

0	Standard conditions
d	Diffusive
DGM	Dusty gas model
eq	Equilibrium
p	Viscous
e	Effective

Chapter 1

General Introduction

Fuel cell is an old concept, dating back to the nineteenth century work of British scientist Sir William Robert Grove [3]. Grove's experiment in 1839, electrolysis of water and his subsequent reasoning of reverse electrolysis to produce electricity and water, resulted in the device which we now refer as fuel cell. However, fuel cell took significant time to mature as a technology and is still not ready to exploit the niche domestic market. In the early days (1960s) the expense associated with the cell manufacturing prohibited them from terrestrial applications and was considered only for space applications (eg. Apollo space craft) where light weight and safety are of major concern. Nevertheless, over years the technology has grown significantly and has begun to look promising in offering inexpensive and clean energy. A recent survey of fuel cell activity and commercialization is reported in [4]. Today mainly five different types of fuel cells are under development,

- Alkaline fuel cells (AFCs)
- Polymer electrolyte membrane fuel cells (PEMFCs)
- Phosphoric acid fuel cells (PAFCs)
- Molten carbonate fuel cells (MCFCs)
- Solid oxide fuel cells (SOFCs)

All these cells differ in various respects like the type of electrolyte, fuel used, operating temperature etc. The work presented in this thesis focuses on solid oxide fuel cells and is explained in more detail in the following sections.

1.1 Solid oxide fuel cells

SOFCs are complete solid state devices, operating at high temperature [3]. The high operating temperature of SOFCs (500-1000°C), enables them to utilize hydrocarbons without

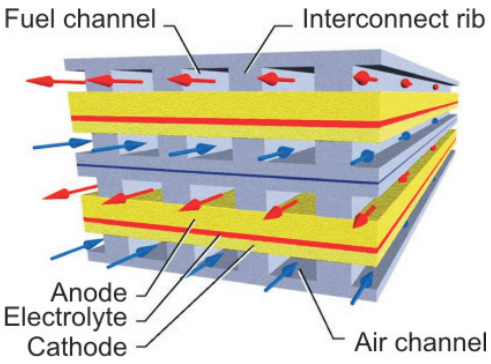

Figure 1.1: A three-dimensional schematic representation of counter flow SOFC stack (Courtesy of R. J. Kee, Colorado School of Mines.)

upstream fuel processing. This is definitely an attractive feature of SOFCs opening up a wide range of fuel choices, starting from hydrogen to natural gas and ethanol. Running efficiently on these fuel systems make SOFCs viable candidate for applications such as stationary power generation and auxiliary power units (APU). However, only pre-reformed fuel is utilized in the present installations due to coking issues. Like any other fuel cell system SOFCs are made up of different components. Before getting into the modeling and simulation of SOFC processes, which is the main focus of this dissertation, it is worthwhile to describe the various components and parts that make up a SOFC stack and the preferable fuels. However, the development and fabrication of electrode materials, interconnects, manifolds, and stacks are highly complex processes and are not within the scope of this thesis. A general discussion on SOFC materials is given by Weber at al. [5]. A schematic representation of SOFC stack for counter flow configuration is shown in Fig. 1.1

1.1.1 Anode

SOFC anodes is typically a complex inter-networks of ionically and electronically conducting phases, and gas-filled porosity. Control of the composition and micro-structure is critical for the activity of electrodes [6]. Percolating networks of three-phase boundaries formed by the electronic phase, ionic phase, and the gas-phase are important for high electrochemical performance of the cell. A three-dimensional reconstruction of a typical state of the art Ni/YSZ anode and its three-phase boundaries reproduced from [7] is shown in Fig. 1.2. There are numerous techniques by which the anodes can be fabricated [8, 9]. In all cases the NiO-YSZ active layer as fired is a dense material, and most of the porosity results during the reduction process [7]. Zhu et. al [10] reported that a continuous porosity of more than 30% is required to facilitate the transport of reactants and products to and away from the three-phase boundary (TPB).

Typical anodes are cermets composed of metals and ceramics. The metallic phase is required for the transport of electrons which are released at the three phase boundary (TPB), while the ceramic phase facilitates the transport of oxygen ions. The ceramic is often made of

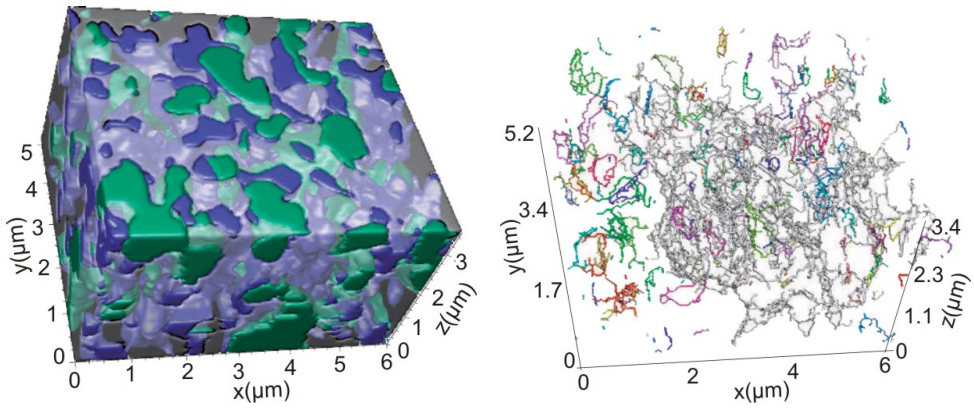

Figure 1.2: (a) A view of the 3D reconstruction showing the Ni (green), YSZ (translucent/gray), and pore (blue) phases. (b) 3D map of the three-phase boundaries in the anode. Each color represents a set of contiguous TPBs. 63% of the TPB length is connected (coloured while/gray) and the remaining length consists of shorter disconnected TPB segments. Reproduced from [7].

the same material as the electrolyte. Ni/YSZ is the conventionally used cermet anode, where Ni plays the dual role of hydrogen (or hydrocarbon) oxidation catalyst and electric current conductor. The anode of an SOFC in principle should meet a variety of requirements: it should be catalytically active, it should be an electronic conductor, should exhibit thermal expansion properties matching those of other components, it should be mechanically stable, and should transport the reactants and products to/from the three-phase boundary [11, 12]. Unfortunately none of the existing anode materials meet all of the requirements. Although, Ni/YSZ is the most commonly used anode cermet, there are serious issues for the direct utilization of hydrocarbons (HCs) on Ni-YSZ anodes due to the coking propensity of Ni for HCs [13]. Furthermore, Ni/YSZ anodes are found to deteriorate over time and are less tolerant to sulfur and suffer from volume instability due to poor redox cycling [14, 15]. Therefore, several materials and barrier layers resistant to coke formation during direct operation on HCs are investigated as anode materials [16, 17].

Ceria based anode

Ceria based anodes (Yttrium doped ceria (YDC)) are good choice for direct operation on HCs [18, 19]. Ceria based anodes are widely recognized for their ability to suppress coking, leading to the utilization of methane rich fuels at low steam to carbon ratio. Instead of Yttria, Samaria can be doped to ceria (SDC). However, the electronic conductivity of YDC anodes is higher than that of SDC. Both doped and undoped ceria display mixed ionic and electronic conduction at low oxygen partial pressure. However, the main draw back of ceria based anode is the lattice expansion at low oxygen partial pressures. This can lead to the formation of cracks at the electrode-electrolyte interface and subsequent delamination of the electrode from the electrolyte interface especially with YSZ electrolyte [10]. However, doping with

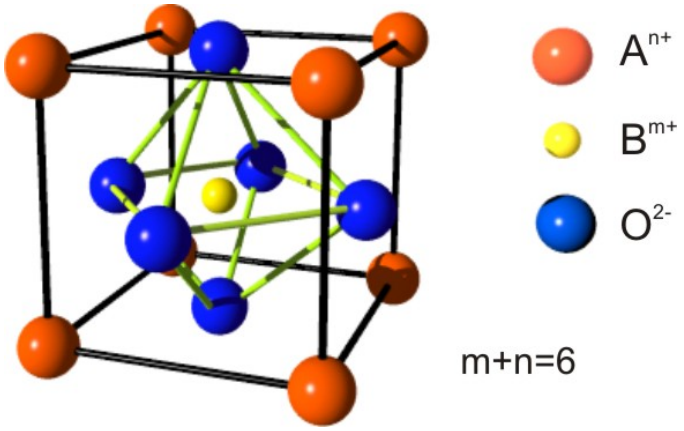

Figure 1.3: Unit cell of a perovskite material.

cations of Gadolinium (Gd^{3+}) or Samarium (Sm^{3+}) or Yttrium (Y^{3+}) can significantly reduce the dimensional contraction during reduction.

Perovskite anodes

Replacing Ni/YSZ by a material free of Ni exhibiting identical electro-catalytic properties to increase the durability is the focus of many research groups. Among many different material types, the perovskite-type ceramics have received special attention. The perovskite structure has the generic formula ABO_3 (Fig. 1.3). The A sites are occupied by large cations such as La, Sr, Ca, and Pb at the corners of the cubic unit cell and B sites at the cube centers are occupied by smaller cations such as Ti, Cr, Ni, Fe, Co and Zr [14]. These smaller cations are surrounded by six oxygen ions in an octahedral coordination. Varying levels of electronic and ionic conduction can be achieved by different combinations of cations. Another property of the perovskite materials is their mixed ionic and electronic conductivity, which can result in increased three-phase boundary length and hence enhanced electro oxidation. Tao et al. reported a Ni free perovskite anode material $La_{0.75}Sr_{0.25}Cr_{0.5}Mn_{0.5}O_3$, which has comparable electrochemical performance to conventional Ni/YSZ anode cermets [15]. Furthermore, the material is found to be more tolerant towards carbon deposition. However, each perovskite material shows different properties. For instance the electrochemical performance of $La_{0.7}Sr_{0.3}Cr_{0.8}Ti_{0.2}O_3$ and $SrTiO_3$ perovskite anodes is much inferior compared to conventional Ni/YSZ cermet anode [10]. Materials such as $La_{0.6}Sr_{0.4}Co_{0.2}Fe_{0.8}O_3$ and $LaNi_{1-x}M_xO_3$ (M: Ti, V, Nb, Mo, W) are not viable anode materials, because they are unstable in reducing atmosphere due to the generation of oxygen vacancies.

1.1.2 Cathode

At the cathode of a SOFC, the transfer of electrons to the oxygen as well as the transfer of anions (-negatively charged oxygen ions) to the electrolyte take place. The cathode transports

air from the cathode channel towards the three-phase boundary. In most cases the cathodes are made of perovskite materials like (strontium-doped lanthanum manganite) LSM [18, 20] or LSCF ($La_{0.84}Sr_{0.16}Co_{0.3}Fe_{0.7}O_3$) [21], which are effective catalysts for the dissociation of oxygen [14]. Since the O^{2-} ion formation is an energy demanding reaction, the activation loss at the cathode is much higher than that of anode and is often the main factor for limiting the performance of SOFC [22, 23]. Any material that can effectively catalyze the formation of O^{2-} ions can reduce activation overpotential . The application of multilayer LSM cathode has been reported to decrease the overpotential significantly [24]. In general, decreasing the grain size while maintaining a high porosity of the cathode results in a high current output. Therefore, multi-layered cathodes with larger grains on the outer layer and smaller grains on the inner layer can significantly increase the performance [25]. Multi-layered cathodes with graded transition from material to material are also reported. [26].

Many factors are known to affect the performance of the cathode such as the material composition, material processing, sintering conditions, density and surface morphology, and resistivity [23]. Moreover, the influence of these parameters on cathode performance is not static; rather it changes and evolves during fuel cell operation [27]. A critical SOFC component which adversely affects the cathode performance especially during high temperature operation is the metallic interconnect made of Cr alloys. Most of the high temperature resistant alloys form the oxide Cr_2O_3 on the surface, and hence, the generation of $CrO_2(OH)_2$ degrades the performance of cathode [28]. The lower oxygen partial pressure at the cathode electrolyte interface due to electrode polarization leads to the precipitation of Cr_2O_3 from $CrO_2(OH)_2$ near the three-phase interfaces. This leads to an increase in charge transfer and diffusion resistance, and thereby results in increased cathode overpotential, which further reduces performance. Irrespective of these facts increasing overpotential due to pore formation near the interface after several hours of operation (>2000h) is common to all cathode materials [22].

1.1.3 Electrolyte

The electrolyte in SOFC is a ceramic material sandwiched between the anode and the cathode, which is impervious to gas transport. Any gas transport would lead to the thermal oxidation of the fuel releasing heat, which otherwise would have resulted in electrical energy. In general the electrolyte should be a very good ionic conductor to facilitate the transport of oxygen ions formed at the cathode-electrolyte interface towards the electrolyte-anode interface. On the other hand the electrolyte should have no conductivity for electrons. Any electronic conductivity would let the electrons released at the anode to flow directly towards the cathode without reaching the external load. Moreover, the electrolyte should be stable in both oxidizing and reducing atmospheres. Though electrolytes basically can serve as structural support for SOFCs, (where electrolytes of thickness ~150 μm are used [5]) with more and more attention given to anode supported cells, thin film electrolytes (~10 μm [22]) are

the center of electrolyte research. The use of 10-20 μm thick electrolytes result in marked decrease in ohmic resistance contribution to the overall cell voltage loss [29].

The most common electrolyte material is zirconia with 8% yttria added as dopant known as yttrium-stabilized zirconia or YSZ, which is a polycrystalline ceramic, exhibiting excellent stability in both oxidizing and reducing atmospheres. However, electrolyte supported cells using YSZ as the electrolyte material face many problems during high temperature operation [6]. Therefore, other oxide ion conducting materials such as $LaGaO_3$ are preferable for electrolyte supported cells. Ceria based electrolytes such as Gd_2O_3 doped CeO_2 (GDC) have higher ionic conductivity than YSZ and therefore are preferred for intermediate temperature (700-800°C) applications [21]. For operating temperatures below 700°C scandia doped zirconia (SDZ) could be a better choice. At low temperatures (<550°C) ceria based electrolytes can be used [30].

1.1.4 Interconnect

The role of interconnects as a critical SOFC component is dual fold. It serves as electrical contact between the anode of one individual cell to the cathode of the neighboring cell. It also serves as a physical barrier to protect the cathode material of one individual cell from reducing environment of the fuel on the anode side of the neighboring one and vice versa [31]. Therefore, the interconnect materials must be stable both in oxidizing environments as well as in reducing environments [32]. In certain stack constructions, the interconnect also serves as a structural support material [33]. Interconnects generally form the major proportion of the cost of the stack [22]. However, the cost factor can vary depending on the operating temperature. In high temperature SOFC interconnects are made of ceramic materials, such as lanthanum chromate or sophisticated refractory alloy. The commonly used interconnect materials are doped $LaCrO_3$ based materials [15] and high-temperature oxidation resistant alloys. Compared to ceramic interconnects metallic interconnects offer high electrical conductivity and are less expensive. However, the electronic conductivity of metallic interconnects depends on the dopants and the doping level [34]. The two most common dopants added to lanthanum chromate are strontium and calcium. At high operating temperatures metallic interconnects such as Fe-based or Ni-based alloys are easily oxidized [35]. Therefore, it is inevitable that the formation of oxide is sluggish and strongly binds to the substrate during thermal cycling. The contact resistance of an oxidized metallic interconnect is usually characterized in terms of area specific resistance (ASR) and the generally accepted value is less than 0.1 Ωcm^2 [29]. When using thin film electrolytes, metallic interconnects are being viewed as highly practical in low temperature applications.

Chromium present in the alloy material of metallic interconnects is reported to have counter effects in the aging of SOFCs. On one hand Cr containing alloys lead to rapid degradation of electrical properties of SOFC due to Cr evaporation at the cathode side [22,36], but

on the other hand Ni or Fe-based alloys are prone to metal dusting and the presence of Cr in these alloys decreases the metal dusting rate [35]. Metal dusting is a corrosion phenomenon leading to structural disintegration of metals and alloys into dust composed of fine particles of the metal/alloy and carbon.

1.2 Fuels and fuel processing

1.2.1 Fuels

Most fuel cells require fairly pure hydrogen as fuel, and fuel cells which can use other fuels typically work best with hydrogen [37]. Recently there has been a considerable interest in running SOFCs on direct hydrocarbons [38, 39, 40]. Natural gas, due to its widespread availability and distribution infrastructure is an ideal choice for stationary SOFC applications. [41, 37]. Due to the high energy density liquid hydrocarbons (propane and butane) are preferred for portable applications [42]. Furthermore, they are readily available, inexpensive, and are the lowest molecular weight hydrocarbons that can be easily handled as liquids [37]. Additionally, alcohols (methanol and ethanol) have also been considered for portable fuel-cell applications. Though there are reports on the operation of SOFCs on fuels such as ethane, propane [43, 44], butane [42, 17] and octane [40], these are limited to a laboratory environment and furthermore, while running these fuels on SOFC, they no longer remain as higher hydrocarbons, but rather break down to smaller molecules, and the electrochemical charge transfer proceeds through hydrogen and CO oxidation. A list of fuels that can be used in SOFC is given in [45].

Though these fuels can be practically used in SOFC, the choice of proper fuel predominantly depends on the operating temperature of the cell. Natural gas and higher hydrocarbons can be effectively reformed in SOFCs operating above 600°C. For operating temperatures as low as 500°C oxygenates such as methanol or ethanol are considered as the most likely fuel due to the low temperature required for the effective reforming of these fuels [46].

1.2.2 Fuel processing

The main reason that SOFCs can run on hydrocarbons is the high temperature of operation. This high temperature is ideal for reforming reactions to produce electrochemically active synthesis gas (H_2 and CO). The electrochemical activity of various chemical species is still a topic of open debate. However, there is no doubt on the electrochemical activity of H_2 and CO [47, 48, 49]. Therefore, any fuel used in SOFC must be finally converted into H_2 and/or CO to enable charge transfer reactions. The fuel processing can be achieved either internal or external to a fuel cell stack [50]. Using external reformer, however, results in extra cost added to the overall system and hence internal reforming is a very attractive option. Internal reforming can be carried out either in a fuel reformer integrated within the stack (indirect

internal reforming), or directly on the fuel cell anode (direct internal reforming) [45]. Indirect internal reforming design increases the system efficiency by effectively recuperating the high quality waste heat from the stack into the fuel supply.

The direct internal reforming of HCs can eliminate the need of a fuel reformer and the extra cooling air which would otherwise be required in an SOFC running on hydrogen. Thus the direct internal reforming basically results in an increased overall efficiency of the system and lower additional costs [18]. However, direct internal reforming of hydrocarbons without upstream reforming is challenging due to the possibility of anode fouling [51]. Therefore, issues related to coking have been widely studied [16, 13, 52]. So far existing installations of SOFC plants do not resort to the direct use of hydrocarbon fuels, mainly due to electrode stability issues. Instead, hydrocarbons are pre-reformed before entering the fuel cell stack. Moreover, SOFC anodes are not tolerant to sulfur content in natural gas. Therefore, the existing installations do require some amount of fuel processing in front of the stack [37,53].

The wider range of fuel choice for SOFC also calls in for advanced electrode materials for achieving the maximum performance. There is a considerable effort going on aimed at improving the thermo-catalytic, structural, and electrical properties of SOFC electrodes [54,17]. In a noted review, it is said that, *"Although cost is clearly the most important barrier to the widespread SOFC implementation, perhaps the most important technical barriers currently being addressed relate to the electrodes, particularly the fuel electrode or anode"* [37].

1.3 Aim of current study

For the further development of SOFC technology, the combination of modeling and experimental evaluation of the models is important. Accurate numerical models taking into account physico-chemical processes are cost effective and can substitute many expensive experimental runs. Due to the inter-disciplinary nature of the subject, literature data on SOFC analysis is quite diverse in nature. A large body of literature data is focused on material issues. Electrochemical performance characteristics are well studied by button cell experiments for H_2 and CH_4 fuel. However, for CH_4 fuel electrochemical data at different steam dilution and operating temperatures are really scarce. In SOFC literature there is a plethora of numerical models. Simple zero dimensional models to stack level models are reported. However, models with thorough validation of electrochemistry and catalytic chemistry are few. One reason may be the lack of detailed experimental data on the catalytic chemistry in SOFCs under short circuit conditions. Excerpting the potential of elementary heterogeneous chemistry for steam reforming of CH_4 on Ni, this dissertation explores the performance of SOFCs under internal reforming conditions. The elementary mechanism is thoroughly validated for SOFC operating conditions by specially designed experiments carried out at Colorado School of Mines. Validity of electrochemical model parameters is ensured by comparison with experimental data. The work also explores various porous media transport models and

their validity for application in fuel cell anodes. Modeling is carried out at unit cell level, including interconnects.

Chapter 2

Heterogeneous chemistry

2.1 Introduction

Heterogeneous chemical reactions proceeding at the interface between the solid catalyst surface and the adjacent gas-phase are central to many chemical engineering applications. The catalyst basically provides an alternate reaction pathway by lowering the activation energy for the reaction as shown in Fig.2.1. The surface intermediates can react among themselves

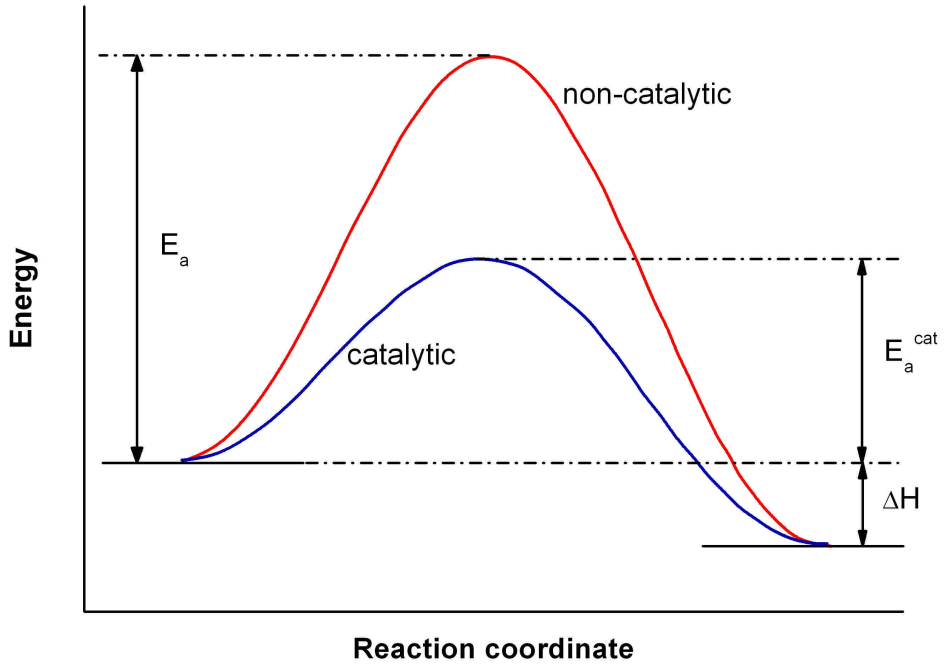

Figure 2.1: Activation energy for catalytic and non-catalytic pathway for a chemical reaction

or can directly react with the gaseous species. However, an important feature of heterogeneous catalysis is that the products of reaction must be removed rapidly from the catalyst

surface in order to generate free active sites. In general heterogeneous catalysis comprises various physico-chemical processes such as: [55]

- Chemisorption
- Dissociation/activation
- Diffusion
- Recombination
- Desorption

The rates of surface reaction depend on the fractional coverage of the surface adsorbed species and the temperature. However, the rates are particularly specific to the catalyst formulation, catalyst support, and catalyst structure. And therefore, the description of heterogeneous reaction rates is more complex compared to gas-phase kinetics.

In most cases heterogeneous reaction rates are described in terms of adsorption isotherms, sticking coefficients, or elementary step rate constants. These include Langmuir adsorption isotherm, competitive adsorption, Langmuir-Hinshelwood kinetics, the BET isotherm and so forth. However, by using mean field approximation, heterogeneous reactions on the solid surfaces can be principally treated by drawing analogy with gas-phase reactions. A general introduction to these topics is discussed in the following section [56]. The mean field approximation and the kinetic models used in the present work will be discussed briefly.

2.2 Mean-field approximation

In mean-field approximation, the surface adsorbates are assumed to be uniformly distributed over the catalyst surface. The state of the catalyst surface is described by the surface temperature T and the fractional coverages of the adsorbates θ_{k}. Fractional coverage θ_{k} is the fraction of the surface covered by the surface adsorbed species k. Furthermore, it is assumed that the adsorption is limited to a mono atomic layer, and an uncovered surface is treated as the K_{s}'th surface species. This means, there are only $K_s - 1$ surface adsorbed species. Assuming the surface temperature and coverages can be averaged over microscopic fluctuations, a chemical reaction can be defined in a way similar to gas-phase reactions,

$$\sum_{k=1}^{K_g+K_s+K_b} \nu'_{ki}\chi_k \Rightarrow \sum_{k=1}^{K_g+K_s+K_b} \nu''_{ki}\chi_k \tag{2.1}$$

χ_k is the species involved in the reaction and ν'_{ki} and ν''_{ki} are the stoichiometric coefficients of the k'th species for the i'th reaction. The total surface concentration, when all the adsorption

sites are covered or, in other words the saturation sorbent capacity is given by the maximum surface site density Γ in mol/m^2 [56]. And the number of sites required for the species to adsorb on the surface is given by the coordination number σ_k. In the following analysis it is assumed that the total number of surface sites is conserved for each reaction, i.e,

$$\sum_{k=1}^{K_s} \nu_{ki}\sigma_k = 0, \tag{2.2}$$

The above equation means that if the reactants occupy two surface cites then the products should also occupy two surface cites. Here $\nu_k = \nu''_k - \nu'_k$. However, the scenario could be different in case of Chemical Vapor Deposition processes (CVD), where the surface sites are not conserved. The net molar production rate $\dot{s}_k$ of a gaseous species or a surface adsorbed species due to heterogeneous reaction can be written as

$$\dot{s}_k = \sum_{i=1}^{N_s} \nu_{ki} k_{f_i} \prod_{k=1}^{K_g+K_s+K_b} [X_k]^{\nu'_{ki}}. \tag{2.3}$$

Based on mean field approximation the rate constant can be expressed in an Arrhenius form:

$$k_{f_i} = A_i \left[\frac{T}{T^0}\right]^{\beta_i} \exp\left(-\frac{E_{ai}}{RT}\right) \prod_{k=K_g+1}^{K_g+K_s} \theta_k^{\mu_{ki}} \exp\left(-\frac{\epsilon_{ki}\theta_k}{RT}\right), \tag{2.4}$$

where k_{f_i} is the rate constant for the i'th reaction, μ_{ki} and ϵ_{ki} are the parameters modeling the coverage dependency of rate constant for the i'th reaction, and θ_k is the surface coverage of the kth species. The rate constant for the reverse reaction can be calculated from the thermodynamic data as

$$K_{c_i} = \frac{k_{f_i}}{k_{r_i}} = K_{p_i} \left(\frac{p^0}{RT}\right)^{\sum_{k=1}^{K_g} \nu_{ki}} \prod_{k=K_g+1}^{K_g+K_s} \frac{\sigma_k^{\nu'_k}}{\sigma_k^{\nu''_k}}, \tag{2.5}$$

where p^0 is the standard state pressure and K_{p_i} is the equilibrium constant calculated by

$$K_{p_i} = \exp\left(\frac{\Delta S_i^0}{R} - \frac{\Delta H_i^0}{RT}\right). \tag{2.6}$$

Equation 2.5 follows from the definition of K_{c_i} and K_{p_i} as

$$K_{c_i} = \frac{\prod_{k=1}^{K_g+K_s} [X_k]^{\nu''_{ki}}}{\prod_{k=1}^{K_g+K_s} [X_k]^{\nu'_{ki}}}, \quad K_{p_i} = \frac{\prod_{k=1}^{K_g} (p_k/p^0)^{\nu''_{ki}}}{\prod_{k=1}^{K_g} (p_k/p^0)^{\nu'_{ki}}} \frac{\prod_{k=k_g+1}^{K_g+K_s} \theta_k^{\nu''_{ki}}}{\prod_{k=k_g+1}^{K_g+K_s} \theta_k^{\nu'_{ki}}}. \tag{2.7}$$

The relationship between surface coverages and the surface concentrations are given by

$$\theta_k = \frac{[X_k]\sigma_k}{\Gamma}, \tag{2.8}$$

and the temporal variations of surface coverages are given by

$$\frac{d\theta_k}{dt} = \frac{\dot{s}_k \sigma_k}{\Gamma}, \quad k = K_\mathrm{g} + 1, \ldots, K_\mathrm{g} + K_\mathrm{s}. \tag{2.9}$$

Since the surface coverages are referred to a single mono-layer, the sum of coverages obeys the condition

$$\sum_{k=1}^{K_s} \theta_k = 1. \tag{2.10}$$

The change of entropy ΔS^0 and enthalpy ΔH^0 are given by

$$\frac{\Delta S_i^0}{R} = \sum_{k=1}^{k=K_g+K_s} \nu_{ki} \frac{S_k^0}{R}, \tag{2.11}$$

and

$$\frac{\Delta H_i^0}{RT} = \sum_{k=1}^{k=K_g+K_s} \nu_{ki} \frac{H_k^0}{RT}. \tag{2.12}$$

2.2.1 Adsorption and sticking coefficients

One of the major mechanistic steps during heterogeneous chemical reactions is the collision between the gaseous species and the catalytically active solid adsorbent. According to kinetic theory the rate at which these collisions occur is given by

$$Z = \sqrt{\frac{k_B T}{2\pi M}} \left(\frac{N}{V}\right), \tag{2.13}$$

where k_B is Boltzmann's constant, T is the absolute temperature, W the molar mass, and N/V is the number density of gas molecules. However, these surface collisions are only one of the several processes that occur during surface reactions. For example the surface adsorbate can be mobile, there can be interactions between the surface adsorbates, dissociative adsorption, and desorption from the surface and so forth. However, for a simple sticking reaction, the reaction rate is just the rate of collision multiplied with the probability that the collision results in the formation of a surface adsorbate. The probability of such a process, or in other words the ratio of the rate of adsorption to the rate at which the adsorptive strikes the total surface can be expressed in terms of sticking coefficient S_i^0. Furthermore, the sticking coefficient in general depends on temperature and the temperature dependency is expressed as

$$S_k^0 = S_i^0 = a_k \left[\frac{T}{T^0}\right]^{b_k} \tag{2.14}$$

Since sticking coefficient is a probability factor its value should lie between 0 and 1. a_k and b_k are dimensionless and c_k has units compatible with gas constant R. The expression for

reaction rate while using sticking coefficient can be written as

$$\dot{s}_k = S_k^0 \sqrt{\frac{RT}{2\pi W}} [X_k] \theta_{\text{free}}^{\tau}. \tag{2.15}$$

Here θ_{free} is the available free surface coverage for collision $\tau = \sum_k^{K_s} \nu'_{ki}$. Equation 2.8 can be used to rearrange Eq.2.15 to give

$$\dot{s}_k = k_{f_i} [X_k] [X_{\text{free}}]^{\tau}, \tag{2.16}$$

where

$$k_{f_i} = \frac{S_i^0}{\Gamma^{\tau}} \sqrt{\frac{RT}{2\pi W}}. \tag{2.17}$$

2.3 Fuel cell catalysis

The anode of a SOFC is a place where substantial heterogeneous chemistry can proceed while running them on hydrocarbons, hydrocarbon derived fuels or bio-mass derived fuels [19,46,57]. However, the proceeding reaction pathway depends on the inlet fuel composition and the stoichiometric composition of the resulting fuel within the anode compartment due to electrochemistry. In case of a fuel feed consisting of CO_2 and little H_2O, dry reforming is the main pathway, though during the later stages steam reforming can dominate depending on the electrochemical rate at the three-phase boundary. Steam reforming is a matured technology or commercial production of H_2 widely practiced in industry [58]. Though steam reforming can be used to produce H_2 from any hydrocarbon feed stock, the scope of this dissertation is limited to CH_4.

Nickel is the most widely used electro-catalyst in SOFC anodes and therefore, steam reforming of CH_4 on Ni supported catalysts have been widely studied [59, 58]. The major reactions that CH_4 can undergo during reforming or partial oxidation can be summarized as [58]

$$CH_4 + H_2O \rightleftharpoons CO + 3H_2 \quad (\Delta H^0 = 206.2 \text{ kJ/mol}), \tag{2.18}$$

$$CH_4 + CO_2 \rightleftharpoons 2CO + 2H_2 \quad (\Delta H^0 = 274.2 \text{ kJ/mol}), \tag{2.19}$$

$$CO + H_2O \rightleftharpoons CO_2 + H_2 \quad (\Delta H^0 = -41.1 \text{ kJ/mol}), \tag{2.20}$$

$$CH_4 + O_2 \rightleftharpoons CO_2 + 2H_2 \quad (\Delta H^0 = -320 \text{ kJ/mol}). \tag{2.21}$$

CH_4 can also undergo cracking on Ni surface leading to C formation

$$CH_4 \rightleftharpoons C + 2H_2 \quad (\Delta H^0 = 75\ \text{kJ/mol}). \tag{2.22}$$

It is well known that Ni catalyzes carbon formation, if insufficient amount of steam is present along with hydrocarbons or CO [60]. Therefore, a number of research groups have studied carbon deposition and the related cell performance which is discussed in section 2.3.1. A schematic representation of the global reactions that occur in an SOFC anode is shown in Fig. 2.2.

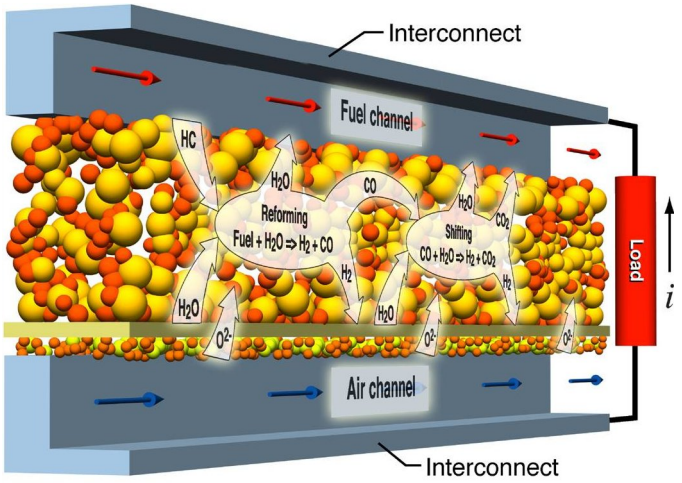

Figure 2.2: A schematic representation of the major reaction processes in an SOFC anode (Courtesy of R. J. Kee, Colorado School of Mines)

Though Eqs. 2.18 to 2.22 look simple from a global perspective, in reality these reactions proceed in a much more complex fashion: such as adsorption of the gas-phase species on the surface followed by reaction among various surface adsorbed species and desorption from the surface into the gas-phase. Chemisorption of CH_4 (or any hydrocarbon) on metals involve the cleavage of C-H bond [58]. CH_4 undergoes stepwise dehydrogenation on Ni leading to surface intermediates as proposed by Alstrup et al. [61]:

$$CH_4 \Rightarrow CH_3(\text{Ni}) \Rightarrow CH_2(\text{Ni}) \Rightarrow CH(\text{Ni}). \tag{2.23}$$

Xu et al. have studied the kinetics of CH_4 reforming on Ni supported magnesium spinal [62,63]. However, their experiments are carried out at low temperatures ranging from 500°C to 575°C, which is quite low compared to the nominal operating temperatures of SOFC. Ceria has been proven as a good material to be used in SOFC anodes, particularly while operating on direct hydrocarbons [19, 17, 16].

There are numerous reports on the reforming kinetics of CH_4 on Ni catalysts, however, only few deals with the reforming over the anode of a real SOFC. Timmerman et al. studied internal reforming of methane at Ni/YSZ and Ni/CGO SOFC cermet anodes [59]. Nagakawa et.al studied steam reforming kinetics on a real operating fuel cell [19]. When the partial

pressure of H_2 was below 5 kPa, under open circuit conditions they observed decreasing rate for steam reforming, however, the rate was restorable by exposing the anode to H_2 for a while. Based on these observations they concluded that an oxidized state of the Ni surface can result in decreased catalytic activity, while exposing the anode to reducing environment can result in increased activity.

Hecht et al. have studied the reforming kinetics based on an elementary reaction mechanism, using experiments tailored to mimic a typical fuel cell operation [64]. In their separated anode experiments, two flow channels were separated by the anode of an SOFC. One of the two channels was fed with fuel and the other was fed with H_2O or CO_2 diluted in Argon. The experiment was designed in a way that permitted the transport of species between the two channels through the reactive porous media. In all cases the mechanism used by Hecht et al. reasonably well reproduces the experimental observations.

2.3.1 Carbon deposition

Though it is theoretically possible to operate an SOFC on hydrocarbon fuels, running them on Ni based anodes is a challenge due the coking propensity. This is much more severe for higher hydrocarbons. Although carbon deposition can be suppressed by operating at high steam to carbon (S/C) ratio, this results in decreased cell performance due to fuel dilution. Koh et al. studied the effect of carbon deposition on cell performance [13]. Based on thermodynamic calculations they also report a ternary diagram for the C-H-O system, which identifies the carbon deposition boundary. In general C deposition depends strongly on S/C ratio and operating temperature. Finnerty et al. studied the C deposition effects on Ni/YSZ anodes at various YSZ dopant levels. They observed dissociative adsorption of methane (Eq. 2.23) and subsequent C deposition (Eq. 2.22) at temperatures above 780°C. [52]. Though open circuit conditions can result in detrimental C deposition at low S/C ratio, in certain cases the cell can be recovered by applying load [13]. It is worth mentioning that activity of YSZ as a reforming catalyst has also been reported in the literature [65].

Based on the study of bimetallics Lee et. al concluded that, stable operation of n-butane is possible on anodes based on Cu-Ni and Cu-Co [17]. Their study shows that cermet based Cu-Co (20 wt-%) resulted in minimum C deposition while 4 wt-% Ni resulted in maximum C deposition. Furthermore, they also found the reduction temperature to be very important for the formation of C on Cu-Ni bimetallics. In another interesting report McIntosh et al. claimed that the C deposits can increase the electronic conductivity in Cu based anodes, where they achieved catalytic activity by introducing ceria [16].

2.3.2 Elementary kinetics

Elementary reactions are the reaction steps at the most fundamental level. These reactions can not be further decomposed. Furthermore, in case of elementary reactions the rate expression corresponds to the stoichiometric equation. When there is no correspondence between the rate expression and stoichiometry these reactions are called non-elementary reactions. Though not strictly elementary our group proposed an elementary like mechanism for steam reforming of methane on Ni based catalysts. In the study reported by Hecht et al. [64] the multi-step mechanism was evaluated only for 800°C. In work presented in this thesis, the mechanism have been extended to wider temperature ranges (500°C-1800°C) and is listed in the appendix. Though the mechanism is elementary like in nature it covers the global aspects of steam reforming, dry reforming, water-gas shift, reverse water-gas shift and C deposition. The reaction mechanism consists of 42 irreversible reactions among 6 gas-phase species and 12 surface adsorbed species. Most of the reactions are given in the Arrhenius form, or are given in terms of sticking coefficient (section 2.2.1), and some of the activation energies are coverage dependent. The mechanism is constructed in such a way that it ensures thermodynamic consistency of enthalpy and entropy, which means that only the forward reaction rate constant k_f and E_f^{act} can be specified independently, while the reverse reaction rate coefficients and enthalpy are subjected to the following constraints

$$E_{\text{f}}^{\text{act}} - E_{\text{r}}^{\text{act}} = \Delta\text{H}, \tag{2.24}$$

and

$$\frac{A_f}{A_r} = \exp\left(\frac{\Delta S}{R}\right). \tag{2.25}$$

However, the mechanism has not been specifically validated for conditions where coking and bulk-phase Ni oxidation occur. Accurate prediction of surface carbon is essential for precise calculation of open circuit potentials for SOFCs operating on hydrocarbon fuels. Furthermore, the redox stability of Ni under SOFC operating conditions is also a major concern for long term stable operation of SOFCs. Therefore, work remains to be done in validating the mechanism for C deposition and incorporating steps that account for the redox state of the catalyst surface.

Chapter 3

Electrochemistry

3.1 Introduction

Electrochemistry deals with the chemical changes caused by the passage of electric current and the conversion of chemical energy into electrical energy. All electrochemical systems consist of two electrodes separated by the electrolyte. When connected to an external load the potential difference across the electrodes drives the electrons through the external circuit. However, the overall processes in the electrochemical system are quite complex in nature. The elementary processes and factors that affect the processes of charge transfer at the interfaces formed by the electrodes and electrolyte are the predominant concern of research. Nevertheless, charge transfer still remains as one of the least understood aspects of electrochemistry. This chapter briefly introduces the electrochemical principles within the scope of SOFC modeling.

3.2 Charge transfer chemistry

Fundamentally the charge transfer chemistry proceeds by electrochemically active species such as H_2 and CO at the three-phase boundary. Nevertheless, when H_2 and CO are present together in the system, the H_2 oxidation kinetics dominates over CO oxidation [66]. However, as mentioned earlier understanding the kinetics, reaction pathways, and the rate limiting step remains as a complex and challenging task for electrochemists. For the simplest case of hydrogen oxidation a large number of reaction steps are assumed to take place at the Ni/YSZ interface. Many possible reaction pathways are proposed [67, 68, 49, 69]. A discussion of the different proposed pathways is given in [11]. In general the postulated reaction pathways can be grouped into two major categories namely oxygen spillover and hydrogen spill over mechanisms. However, recently there has been some consensus regarding the reaction pathway for hydrogen oxidation reaction on Ni/YSZ anodes [70, 71]. Bessler et. al. [70, 71] convincingly demonstrated draw backs of oxygen spill over mechanism and concluded that the hydrogen spill over is the likely reaction pathway. They also asserted the rate limiting charge transfer

step as the hydrogen spillover from Ni surface to hydroxyl group on YSZ surface. The discussions on the modeling presented in this dissertation are based on the assumption that H_2 is the only electrochemically active species taking part in the charge transfer chemistry by neglecting the contribution by CO.

3.2.1 Hydrogen oxidation

Hydrogen oxidation is the most studied charge transfer reaction in solid oxide electrochemical systems [48, 66, 49, 67, 68, 69, 72, 11]. The global hydrogen oxidation reaction

$$H_2 + O^{2-} \rightleftharpoons H_2O + 2e^-, \tag{3.1}$$

proceeds via multi-step adsorption, desorption and reaction steps. The sequence of possible reaction that constitutes reaction 3.1 is listed below [73]. However, this is only a generic sequence of steps and by no means one that is proved or demonstrated with any degree of certainty.

1) Adsorption/desorption of H_2 on Ni surface

$$H_2 + (Ni) + (Ni) \rightleftharpoons H(Ni) + H(Ni) \tag{3.2}$$

2) Charge transfer at TPB

$$H(Ni) + O^{2-}(YSZ) \rightleftharpoons (Ni) + OH^-(YSZ) + e^-(Ni) \tag{3.3}$$

$$H(Ni) + OH^-(YSZ) \rightleftharpoons (Ni) + H_2O(YSZ) + e^-(Ni) \tag{3.4}$$

3) Adsorption/desorption of H_2O on YSZ surface

$$H_2O(YSZ) \rightleftharpoons H_2O + (YSZ) \tag{3.5}$$

4) Oxygen ion transfer between the bulk and surface YSZ

$$V_o^{\bullet\bullet}(YSZ) + O^{2-}(YSZ) \rightleftharpoons (YSZ) + O_o^{\times}(YSZ) \tag{3.6}$$

The symbols in the bracket stand for the corresponding surface to which the particular species is attached. For example H(Ni) stands for a hydrogen atom attached to Ni surface, and (Ni) represents a free Ni surface. $O^{\times}(YSZ)$ is a lattice oxygen and $V^{\bullet\bullet}(YSZ)$ is an oxygen vacancy. The hydrogen adsorption desorption reaction also appears in the heterogeneous chemistry mechanism listed in Appendix. Although, in principle any of these reactions can be rate limiting, the work presented here follows the report of Zhu et al. [73]; assuming

reaction 3.4 to be rate limiting and others to be in equilibrium. Bessler et. al [70, 71] proved this to be a reasonable assumption [71]. Based on these assumptions the phenomenological Butler-Volmer equation takes the form

$$i = i_0\left[\exp\left(\frac{(1+\beta_a)F\eta_a}{RT}\right) - \exp\left(-\frac{\beta_c F\eta_a}{RT}\right)\right], \tag{3.7}$$

where η_a=E_a-E_a^{eq} is the anodic activation overpotential, and β is the charge transfer coefficient or the asymmetry factor. For single step electron transfer reactions the charge transfer coefficients always obey the condition β_a+β_c=1. The exchange current density i_0 is a quantity dependent on the temperature, reactant and product composition and is given by [74, 73],

$$i_0 = k_{H_2}\exp\left(-\frac{E_{H_2}}{RT}\right)\frac{(p_{H_2}/p^*_{H_2})^{1/4}(p_{H_2O})^{3/4}}{1+(p_{H_2}/p^*_{H_2})^{1/2}}. \tag{3.8}$$

The complex reaction order dependence of exchange current density in H_2 and H_2O are quite different from the ones used for global charge transfer chemistry [75]. The parameter $p^*_{H_2}$ is given by [73]

$$p^*_{H_2} = \frac{A_{H_2}\Gamma^2\sqrt{2\pi RTW_{H_2}}}{S^0_{H_2}}\exp\left(-\frac{E^{des}_{H_2}}{RT}\right), \tag{3.9}$$

where site density $\Gamma = 2.6\times10^{-9}$ mol/cm^2, the pre-exponential factor A_{H_2}=5.59×10^{19} cm^2/s mol, $S^0_{H_2} = 0.01$ is the sticking coefficient for H_2 adsorption, and the activation energy $E^{des}_{H_2}$ = 88.12 kJ/mol. The parameters k_{H_2} and E_{H_2} can be determined by fitting the model to experimental data [74].

3.2.2 Oxygen reduction

As in the case of H_2 oxidation, the oxygen reduction reactions (ORR) on the cathode are also assumed to take place in a multi-step manner. The adsorption of O_2 on the cathode surface is followed by the dissociation into two O atoms, and the surface diffusion to the three-phase boundary region. The O atoms take part in a number of electron transfer steps, reducing O to O^{2-}. The rate limiting process, however, has not yet been identified conclusively. The overall oxygen reduction reaction and the incorporation of the ions into the electrolyte can be written in Kröger-Vink notation as

$$\frac{1}{2}O_2 + V_o^{\bullet\bullet}(el) + 2e^-(c) \rightleftharpoons O_o^{\times}(el). \tag{3.10}$$

The above global reaction can be split into a number of steps. One of the possible sequence of mechanistic steps is described below.

1) Adsorption/desorption of oxygen

$$O_2 + (c) + (c) \rightleftharpoons O(c) + O(c) \tag{3.11}$$

2) Surface diffusion to three-phase boundary regions

$$\mathrm{O(c)} \rightleftharpoons \mathrm{O(TPB)} \tag{3.12}$$

3) Formation of O^{2-} ions and the subsequent incorporation into the electrolyte

$$\mathrm{O(TPB)} + \mathrm{V_o^{\bullet\bullet}(el)} + 2\mathrm{e^-} \rightleftharpoons \mathrm{O_o^{\times}(el)} + \mathrm{(TPB)} \tag{3.13}$$

Assuming the charge transfer step 3.13 to be rate limiting Zhu et al. derived the expressions for Butler-Volmer equation [73]

$$i = i_0\left[\exp\left(\frac{\beta_a F\eta_c}{RT}\right) - \exp\left(-\frac{\beta_c F\eta_c}{RT}\right)\right] \tag{3.14}$$

and the exchange current density as [74, 73]

$$i_0 = k_{O_2}\exp\left(-\frac{E_{O_2}}{RT}\right)\frac{(p_{O_2}/p^*_{O_2})^{1/4}}{1+(p_{O_2}/p^*_{O_2})^{1/2}}, \tag{3.15}$$

where $p^*_{O_2}$ is given by [73]

$$p^*_{O_2} = A_{O_2}\exp\left(-\frac{E^{\mathrm{des}}_{O_2}}{RT}\right), \tag{3.16}$$

where A_{O_2}=4.9 $\times$ 10^{10} kPa, and E_{O_2} = 200 kJ/mol. Other parameters such as k_{O_2} and E_{O_2} are basically fit parameters, which can be deduced by calibrating the model to experimental data [74]. The activation energy for ORR on LSM-YSZ cathodes are reported to be between 100 and 200 kJ/mol [20].

A thorough discussion on the modified Butler-Volmer formalism followed here is described in [73].

3.2.3 Global charge transfer

The discussions in sections 3.2.1 and 3.2.2 and the form of Butler-Volmer equation presented above are based on the assumption of single step electron transfer reaction as the rate limiting process. However, in SOFC modeling literature it is quite common to consider the charge transfer reactions in a global picture. Generally the Butler-Volmer equation is written as

$$i = i_0\left[\exp\left(\alpha_a\frac{n_e F\eta_{act}}{RT}\right) - \exp\left(-\alpha_c\frac{n_e F\eta_{act}}{RT}\right)\right]. \tag{3.17}$$

This equation represents the net current density i in the anodic direction. The first term is the rate of charge transfer in the anodic direction and the second term is the rate of charge transfer in the cathodic direction. α_a and α_c are the asymmetry factors or charge transfer coefficients in the anodic and cathodic directions, respectively. The transfer coefficient is a fraction of

change in polarization that leads to a change in reaction rate constant [76]. And for the case of global charge transfer reactions, the asymmetry factors need not be constrained by $\alpha_a + \alpha_c = 1$ as in the case of single step electron transfer reactions [77]. It is quite common to assume the number of charges transferred $n_e = 1$ [78], however, other values are also reported [79]. A positive value of i would mean the flow of electrons from electrolyte phase to the electrode (anode) and current flow from electrode to the electrolyte.

3.3 Fuel cell irreversibilities

The operation of the cell is associated with various irreversibilities and leads to various potential losses. In the case of electrodes the total resistance comprises of the internal resistance, contact resistance, activation polarization resistance, and concentration polarization resistance. Internal resistance refers to the resistance for electron transport, which is usually determined by the electronic conductivity and the thickness of the electrode structure. Contact resistance refers to the poor contact between the electrode and the electrolyte structure. All resistive losses are functions of local current density. However, one can minimize the overpotential losses by appropriate choice of electrode material and controlling the microstructural properties during manufacturing process.

3.3.1 Activation overpotential

Activation overpotential is associated with the charge transfer process. It can be interpreted as a resistance to the electrochemical charge transfer reaction taking place at the three-phase boundary. The maximum voltage that can be harnessed from the cell under reversible conditions is the open circuit potential (OCV). However, during operation the cell has to overcome the irreversibilities associated with the processes. Therefore, a fraction of the total potential is utilized to drive the charge transfer reaction taking place at the three-phase boundaries. This is known as the activation overpotential. The higher the resistance for charge transfer reaction, the higher will be the activation overpotential. The Butler-Volmer equation conveniently relates the activation overpotential with the current density implicitly. However, the definitions of activation overpotential and the asymmetry factors are potentially confusing.

In general, during anodic charge transfer the electrons are released at the anode-electrolyte interface, and they move towards the cathode through the external circuit whereas the electric current by convention flows in the opposite direction. The electrons (negatively charged) always flow towards the positive terminal, which is the cathode. In order to drive the electrons to the region of lower potential, energy needs to be supplied. Therefore, to drive the electrons from the electrolyte to the anode (in the case of anode charge transfer) energy has

to be spent. The amount of energy requires to drive the electrons depend on the relative potential difference between the anode and the electrolyte. The electric potential of the anode is always lower than that of the electrolyte. Therefore, the forward reaction can be facilitated by increasing the anode potential (i.e. making it less negative). At equilibrium anode electrical potential difference $E_{\mathrm{a}}^{\mathrm{eq}} = \phi_{\mathrm{a}}^{\mathrm{eq}} - \phi_{\mathrm{e,a}}^{\mathrm{eq}}$ the reaction proceeds in the anodic and cathodic direction at equal and opposite rates. The activation overpotential η_{a} is the potential difference exceeding the equilibrium potential difference between the anode and the electrolyte. The electric potential difference between the anode and electrolyte is $E_{\mathrm{a}} = \phi_{\mathrm{a}} - \phi_{\mathrm{e}}$, and the activation overpotential is $\eta_{\mathrm{a}} = E_{\mathrm{a}} - E_{\mathrm{a}}^{\mathrm{eq}}$.

Limiting cases

Two limiting cases exist for Eq. 3.17. At very high activation overpotential the first exponent in Eq. 3.17 turns out to be much greater than the second exponent and hence can be neglected, leading to

$$\eta_{\mathrm{act}} = \left(\frac{RT}{\beta n_{\mathrm{e}} F}\right) \ln i - \left(\frac{RT}{\beta n_{\mathrm{e}} F}\right) \ln i_0, \tag{3.18}$$

this is the well known Tafel equation.

For very low activation overpotentials ($\eta \ll 1$), the argument $\beta n_{\mathrm{e}} F/RT$ becomes much less than unity and the exponent can be expanded in terms of Taylor series. Neglecting the higher order terms leads to the linear current-potential relation

$$\eta_{\mathrm{act}} = i \frac{RT}{n_{\mathrm{e}} F i_0}. \tag{3.19}$$

Though the limiting cases of Butler-Volmer equations are easy to use, one should be careful about the range of activation overpotential for which these equations are valid. Chan et al. [76] reported the lower limit of activation overpotential for which the Tafel equation can be used as $\eta_{\mathrm{act}} > 0.28$ V, and the upper limit for linear current-potential relation ship as $\eta_{\mathrm{act}} < 0.1$ V.

3.3.2 Ohmic overpotential

The major contribution to ohmic overpotential is the ionic resistance of the electrolyte material. In the state of the art anode supported cell the ohmic losses are minimized by the use of thin film electrolytes which are usually 5-10 μm thick and high temperature operation. However, the high temperature operation is not preferred because of the detrimental effects on the cell life time and the cost of ceramic materials required for high temperature operation [80].

The electrodes also contribute to ohmic overpotential due to internal resistance. In the case of mixed electronic and ionic conducting electrodes as such as perovskites both ionic and electronic conduction determines the total internal resistance. However, the electronic

properties strongly depend on composition and micro-structure. For Ni/YSZ cermet the electronic conductivity changes with Ni content. The percolation theory predicts an 'S' shaped curve for the cermet conductivity as a function of Ni content. The percolation threshold, the Ni content at which the conductivity starts to increase, is found to be 30% and depends on porosity, pore size, and particle size distribution. Furthermore, the electrical conductivity of the cermet changes by several orders of magnitude as the fraction of YSZ changes from 0 to 100% [10].

The ohmic overpotential can be expressed as a function of local current density i as

$$\eta_{\text{ohm}} = iR_{\text{tot}}, \tag{3.20}$$

where R_{tot} is the total cell resistance and can be further decomposed into the contribution of individual cell components

$$R_{\text{tot}} = \rho_{\text{e}} l_{\text{e}} + \rho_{\text{a}} l_{\text{a}} + \rho_{\text{c}} l_{\text{c}} + R_{\text{contact}}. \tag{3.21}$$

In the above equation ρ_{e}, ρ_{a}, and ρ_{c} are the respective resistances of electrolyte, anode, and cathode, and l_{e}, l_{a}, and l_{c} are the respective thickness of electrolyte, anode, and cathode, and R_{contact} is any contact resistance present in the system. The most dominant contribution to ohmic resistance is by the electrolyte, which can be expressed as

$$\rho_{\text{e}} = \frac{1}{\sigma_{\text{e}}}. \tag{3.22}$$

Here σ_{e} is the ionic conductivity of the electrolyte and is a strong function of temperature generally expressed as

$$\sigma_{\text{e}} = \frac{\sigma_0}{(T/T^0)} \exp\left(-\frac{E_{\text{e}}}{RT}\right), \tag{3.23}$$

where E_{e} is the activation energy for ion transport.

The total resistance on the anode/cathode side comprises of internal resistance towards the transport of electrons (also ions in the case of mixed ionic electronic conductors) and contact resistance, i.e., the resistance caused by the poor adherence between the anode and the electrolyte. The magnitude of all these resistances depends on the particular material of construction and the micro-structure of the porous electrode.

3.3.3 Concentration overpotential

Concentration overpotential arises from the transport limitations within the porous electrode structure. The maximum potential that can be derived during the fuel cell operation depends on the partial pressure of electrochemically active reactant species, and the product of electrochemical charge transfer reaction at the reaction site (TPB) as described by Nernst equation

3.29. However, due to the transport limitation the concentration of the chemical species at the TPB is different from that in the fuel and oxidizer channels. The concentration overpotential strongly depends on electrode micro-structure. A high tortuosity and low porosity can lead to high concentration overpotentials.

Based on the assumption of equi-molar counter diffusion, analytical expression for concentration overpotential is possible when H_2 is used as fuel [76]. However, the situation is more complex when CH_4 or other hydrocarbons are used as fuel. When any fuel other than pure H_2 or CO is used as the anode stream, numerous chemical reactions proceed in the porous anode and one has to resort to numerical methods to evaluate the concentration overpotential. The most appropriate approach is to solve the porous media problem as a reaction-diffusion equation. But to reduce the numerical intensity of the problem many researchers do adhere to the simple analytical expression derived for H_2 even for the case of hydrocarbons [81].

3.4 Nernst equation and cell potential

The cell potential is the operating potential of the cell, which is a manifestation of the collected differences in the electric potential between the various phases in the cell [82]. Assuming H_2 oxidation as the only charge transfer reaction, the potential difference across the anode-electrolyte interface and cathode-electrolyte interface without taking into account the losses is given by

$$\Phi_c - \Phi_a = \frac{1}{2F}\left(\bar{\mu}_{H_2} + \frac{1}{2}\bar{\mu}_{O_2} - \bar{\mu}_{H_2O}\right), \tag{3.24}$$

where $\bar{\mu}$ is the chemical potential of each species. Considering the overpotential losses the potential across the cell can be written as a function of local current density i

$$E_{cell} = \Phi_c - \Phi_a - \eta_a(i) - |\eta_c(i)| - \eta_{ohm}(i) - \eta_{conc}(i). \tag{3.25}$$

Where η_a and η_c are the activation losses at the anode and cathode side respectively, η_{ohm} is the ohmic overpotential, and η_{conc} is the concentration overpotential. Since porous media transport is modeled in detail in this work the concentration overpotential is not treated explicitly. For perfect gases the chemical potential takes the form

$$\bar{\mu}(T, p) = \bar{\mu}^o(T) + RT\ln\left(\frac{p}{p^0}\right), \tag{3.26}$$

and the chemical potential of each species is independent of all other species. The pressure dependency is governed by the partial pressures. Hence, the term on the right hand side of

Eq. 3.24 can be written as

$$E_{\text{rev}} = \Phi_{\text{c}} - \Phi_{\text{a}} = \frac{1}{2F}\left(\bar{\mu}^{\text{o}}{}_{\text{H}_2} + \frac{1}{2}\bar{\mu}^{\text{o}}{}_{\text{O}_2} - \bar{\mu}^{\text{o}}{}_{\text{H}_2\text{O}}\right) + \frac{RT}{2F}\ln\left(\frac{p_{\text{H}_2,\text{a}} p_{\text{O}_2,\text{c}}^{1/2}}{p_{\text{H}_2\text{O,a}}}\right), \tag{3.27}$$

where

$$\frac{1}{2F}\left(\bar{\mu}^{\text{o}}{}_{\text{H}_2} + \frac{1}{2}\bar{\mu}^{\text{o}}{}_{\text{O}_2} - \bar{\mu}^{\text{o}}{}_{\text{H}_2\text{O}}\right) = \frac{-\Delta G^{\text{o}}}{2F} = E^{\text{o}}. \tag{3.28}$$

This leads to well known *Nernst* equation

$$E_{\text{rev}} = E^{\text{o}} + \frac{RT}{2F}\ln\left(\frac{p_{\text{H}_2,\text{a}} p_{\text{O}_2,\text{c}}^{1/2}}{p_{\text{H}_2\text{O,a}}}\right). \tag{3.29}$$

In the above equation E^{o} is the electromotive force (EMF) at standard pressure. Eq. 3.29 can be substituted back in Eq. 3.25 leading to,

$$E_{\text{cell}} = E_{\text{rev}} - \eta_{\text{a}}(i) - |\eta_{\text{c}}(i)| - \eta_{\text{ohm}}(i) - \eta_{\text{conc}}(i). \tag{3.30}$$

The ohmic loses in Eq. 3.25 is given by Eq. 3.20. The Nernst potential or open circuit voltage (OCV) is the maximum possible potential that can be derived from a cell operating reversibly. Therefore, the Nernst potential is also known as the reversible potential. However, during the operation of the cell the maximum possible potential is always lower than the Nernst potential due to the irreversibilities associated with the fuel cell operation. Further, the Nernst equation can be applied only under equilibrium condition.

Chapter 4

Modeling mass and heat transport

4.1 Introduction

Mathematical models predicting the performance of a fuel cell can assist system development. Seeking for the optimal operating conditions, these mathematical models can effectively substitute expensive experimental runs. Many questions of practical importance such as the excess air requirement and fuel flow rates can be answered using state of the art numerical models. Moreover, simple mathematical models such as a zero dimensional polarization models help to understand the influence of various electrochemical parameters on fuel cell performance [76, 78, 83].

Modeling solid oxide fuel cell is an inherently complex task. Any physically realistic model should account for the coupled interactions of thermo-catalytic and electrochemical effects together with heat and mass transport phenomena. However, the detailed resolution of the resulting interactions of all these phenomena depend on the accuracy of the chemical and physical models employed. A general trend in fuel cell modeling is to represent the catalytic chemistry on a global level (global reactions) and the porous media transport using modified Fick diffusion approach. Irrespective of the model employed, extreme care should be exercised to validate the model using experimental results both from electrochemical performance and thermo-catalytic perspective. Unfortunately, the amount of literature data available to validate the model with regards to thermo-catalytic chemistry is really scarce. Therefore, most fuel cell modeling efforts are focused on validating the model with respect to electrochemical performance paying little attention to catalytic chemistry or neglecting it completely. There is a large body of literature data available on modeling and simulation of SOFC processes, which are briefly reviewed here.

The simplest models analyzing the electrochemical performance are the polarization models [76]. These models are distinctively different in terms of complexity and applicability to fuel cell systems. In most cases these polarization models are developed for chemical systems consisting only of H_2, H_2O, and O_2. The concentration losses in these models are calculated based on mixed diffusion model assuming equi-molar counter diffusion. However,

the models reported by Zhu et al. [78] and Williford et al. [84] require special attention. In their work, Zhu et al. derived a general mathematical model applicable to any multi component system, and the concentration losses are modeled using dusty gas model. However, the model requires more complex numerical calculations. Williford et al. have claimed in their study that the root of concentration loss stems from surface diffusional limitations at the three-base boundary, and therefore, they have included surface diffusional effects into their model. However, the model has the limitation of its applicability only to system consisting of H_2, H_2O, and O_2, and fails to account for all possible surface intermediates.

The quest to predict the effect of other cell components on cell performance and the need to interpret the influence of micro structural properties lead to the development of other simple educative models. An electrolyte model to investigate the migration of O^{2-} ions and diffusion of free electrons is developed by Chan et al. [85]. Interconnects; one of the most important cell component is probably the least numerically investigated cell component. Tanner et al. reported interconnect model to investigate symmetry effects [86]. Model incorporating micro-structure of electrodes has been reported by Xia et al. [87].

Cell level models with varying dimensionality have been reported. To mention a few, 2D models are reported by Li et al. [88], Billigham et al. [89], and Keegan et al. [90]. Burt et al. extended a 1D model to simulate a cell stack using domain decomposition and parallel execution of the code [91]. Aguiar et al. have also reported 1D model for direct internal reforming conditions [81, 92].

Computational Fluid Dynamic (CFD) models are generally useful for stack level modeling [93, 94]. These models can serve very effective in the analysis of thermal stress that can develop within the stack. Selimovic et al. analyzed the thermal stress development within a stack for co, counter and cross flow configuration for H_2 as well as for CH_4 fuel [95]. They concluded that the thermal stresses are minimal for co flow configuration compared to other flow configurations, for both metallic and ceramic interconnects. Imposing cyclic boundary conditions on top and bottom of the model domains, Recknagle et al. also carried out 3D modeling of planar SOFC stacks [96]. They also arrived at the conclusion that co flow configuration results in uniform temperature distribution and lower thermal stress compared to other flow configurations.

Transport through porous media is important in determining the concentration losses due to diffusion limitations within the porous inter networks. The following section briefly walks through some of the diffusion mechanisms and porous media transport models.

4.2 Diffusion mechanisms

The diffusion process in porous media is strongly influenced by the pore size distribution. Based on the size the pores are classified as micro pores ($d_p < 2$nm), macro pores ($d_p > 50$

nm), and meso pores (2nm > d_{p} < 50 nm) [97]. Within a pore, in general three fundamentally different diffusion phenomena can be distinguished.

- Bulk diffusion or free molecular diffusion. This diffusion phenomena is driven by kinetic energy of the gas molecules and is limited by the intermolecular collisions. Therefore, bulk diffusion is dominant in pores having large diameters in which collision with the wall do not play a significant role, i.e. the pore diameter significantly exceeds the mean free path.

- Knudsen diffusion becomes dominant if the mean free path exceeds the pore diameter so that the number of molecule-wall collisions exceed the number of intermolecular collisions.

- Surface diffusion, where adsorbed species hop along the pore walls; this transport mechanism is dominant only in the case of micro-pores.

The relative importance of intermolecular collisions and molecular-wall collisions can be characterized by Knudsen number $Kn = \lambda/d_{\mathrm{pore}}$, where λ is the mean free path and d_{pore} is the average pore diameter. When $Kn \ll 1$ bulk diffusion is dominant and when $Kn \gg 1$ Knudsen diffusion is dominant. When $Kn \simeq 1$, both bulk diffusion and Knudsen diffusion have to be taken into account, which typically is the situation for SOFCs.

The mean free path of a molecule in a gas mixture is given by [98, 99]

$$\lambda_{k\mathrm{m}}^{-1} = \sum_{l} X_l \lambda_{kl,m}^{-1}, \tag{4.1}$$

where $\lambda_{kl,m}$ is the mean free path of species k in l

$$\lambda_{\mathrm{kl,m}} = \frac{RT}{\pi p N_{\mathrm{a}} \sigma_{\mathrm{kl}}^2} \sqrt{\frac{W_{kl}^*}{W_k}}, \tag{4.2}$$

where N_{a} is the Avogadro's number and W_{kl}^* is the reduced molar weight

$$\frac{1}{W_{kl}^*} = \frac{1}{W_k} + \frac{1}{W_l}. \tag{4.3}$$

The collision diameter σ_{kl} of binary pair k-l can be estimated as an arithmetic average of collision diameters of molecules as

$$\sigma_{kl} = (\sigma_k + \sigma_l)/2. \tag{4.4}$$

Besides the diffusive transport, the viscous transport due to pressure gradient also contributes to the total flux, and can be conveniently represented by Darcy's formula. Therefore, choosing the right model for transport and reaction in porous medium is highly important in

the numerical modeling of anode supported SOFCs. A number of approaches can be used to describe the diffusional transport; some of them are discussed below.

4.3 Porous diffusion models

4.3.1 Modified Fick Model (MFM)

Modified Fick model, also known as mixed diffusion approach is the simplest of all approaches. It is easy to program and is less computationally expensive. In this method an equivalent Fickian diffusion coefficient is derived by considering the mixture diffusion coefficient $\mathcal{D}_{km}$ acting in series with Knudsen diffusion coefficient $\mathcal{D}_{kn}$ as follows

$$\frac{1}{\mathcal{D}_{\text{eff}}} = \frac{1}{\mathcal{D}^{\text{e}}_{km}} + \frac{1}{\mathcal{D}^{\text{e}}_{\text{kn}}} \tag{4.5}$$

where the effective mixture diffusion coefficient $\mathcal{D}^{\text{e}}_{km}$ is defined in terms of the mixture diffusion coefficient $\mathcal{D}_{km}$ as

$$\mathcal{D}^{\text{e}}_{km} = \frac{\epsilon}{\tau}\mathcal{D}_{km}. \tag{4.6}$$

Where ϵ is the porosity and τ is the tortuosity of the porous media. The mixture diffusion coefficient for the species k can further be computed as [100]

$$\mathcal{D}_{km} = \frac{1 - Y_k}{\sum_{j\neq k}^{K_{\text{g}}} X_j/\mathscr{D}_{jk}}, \tag{4.7}$$

where $\mathscr{D}_{jk}$ is the binary diffusion coefficient of species j in k and $\mathscr{D}_{jk}$=$\mathscr{D}_{kj}$. However, Eq. 4.7 is mathematically not well defined in the limit of pure species conditions. This problem can be circumvented by evaluating the diffusion coefficient in the following equivalent way [101]:

$$\mathcal{D}_{km} = \frac{\sum_{j\neq k}^{K_{\text{g}}} X_j W_j}{\bar{M}\sum_{j\neq k}^{K_{\text{g}}} X_j/\mathscr{D}_{jk}}. \tag{4.8}$$

The equation is still undefined for pure species condition, however, the round-off error accumulates to the same degree in the numerator and denominator. The Knudsen diffusion coefficient for the species k in Eq. 4.5 is defined as

$$\mathcal{D}^{\text{e}}_{k,\text{kn}} = \frac{2}{3}\frac{\epsilon}{\tau} r_{\text{p}} \sqrt{\frac{8RT}{\pi W_k}}, \tag{4.9}$$

where r_{p} is the average pore diameter. Based on the equivalent Fickian diffusion coefficient the diffusive flux of species k can be expressed as

$$J^d_k = -\mathcal{D}_{\text{eff}}\nabla[X_k]. \tag{4.10}$$

The viscous flow can be formulated in terms of Darcy's formula,

$$J_k^p = -\frac{B_g[X_k]}{\mu}\nabla p. \tag{4.11}$$

Therefore, the total flux of the species k can be written as,

$$J_k = J_k^d + J_k^p = -\mathcal{D}_{\text{eff}}\nabla[X_k] - \frac{B_g[X_k]}{\mu}\nabla p. \tag{4.12}$$

The permeability in Eq. 4.11 is given in terms of Kozeny-Carman equation (Eq. 4.25)

4.3.2 Generalized Maxwell-Stefan Model (GMS)

In its most general form the Maxwell-Stefan equation can be written as

$$\nabla X_k = \sum_{l=1}^{K_g} \frac{X_k X_l (v_l - v_k)}{\mathscr{D}_{kl}}, \tag{4.13}$$

where v is the diffusion velocity of the species. Since the molar diffusivity of species k is defined as

$$J_k = [X_k](v_k - v^*), \quad \text{where} \quad v^* = \sum_k X_k v_k, \tag{4.14}$$

Eq. 4.13 can be written in terms of the molar species fluxes J_k as

$$\nabla X_k = \sum_{l=1}^{K_g} \frac{(X_k J_l - X_l J_k)}{[X_T]\mathscr{D}_{kl}}. \tag{4.15}$$

This is an implicit relationship between molar fluxes and concentration gradients. However, it is possible to invert the Eq. 4.15 to develop a direct representation of molar fluxes J_k as

$$J_k^d = -[X_T][\mathscr{B}]^{-1}\nabla X_k. \tag{4.16}$$

The components of the matrix $\mathscr{B}$ are given by

$$b_{kl} = \left[\frac{X_k}{\mathscr{D}_{kK_g}} + \sum_{j\neq k}^{K_g} \frac{X_k}{\mathscr{D}_{kj}}\right]\delta_{kl} + (\delta_{kl} - 1)\left(\frac{X_k}{\mathscr{D}_{kl}} - \frac{X_k}{\mathscr{D}_{kK_g}}\right). \tag{4.17}$$

One of the main draw backs of GMS formulation from SOFC modeling perspective is its inability to account for Knudsen diffusion. And furthermore, GMS formulation guarantees that the sum of diffusive fluxes vanishes, which is not the case for fuel cell operating conditions due to the viscous transport. The viscous transport can be introduced as in the case of Fick

model to give the total flux as

$$J_k = J_k^d + J_k^p = -[X_T][\mathscr{B}]^{-1}\nabla X_k - \frac{B_g[X_k]}{\mu}\nabla p. \tag{4.18}$$

4.3.3 Modified Maxwell-Stefan Model (MMS)

A more complete description of multi-component transport in pore structure without accounting for the pressure gradient can be obtained using a modified Maxwell-Stefan formulation. The MMS formulation treats molecular diffusion in series with Knudsen diffusion leading to,

$$\sum_{k\neq l}\frac{[X_l]J_k - [X_k]J_l}{[X_T]\mathcal{D}_{kl}^e} + \frac{J_k}{\mathcal{D}_{k,kn}^e} = -\nabla[X_k]. \tag{4.19}$$

The Dusty Gas Model and the Mean Transport Pore Model described in the following sections are basically extensions of MMS model with pressure gradients.

4.3.4 Dusty Gas Model (DGM)

The DGM, originally developed for astrophysical applications, has been widely accepted to describe the transport of multi component ideal gas mixtures in porous media. In its application to porous media problems, the porous medium is visualized as a collection of spherical dust particles constrained to remain stationary in space by undefined forces. In other words the pore walls are considered as giant molecules distributed uniformly in space. These molecules are further considered to be a dummy or pseudo n+1'th species in the n component gaseous mixture [102].

The model accounts for three different transport mechanisms, molecular diffusion, Knudsen diffusion, and viscous transport. The total diffusive flux in DGM results from molecular diffusion acting in series with Knudsen diffusion. The viscous porous media flow (Darcy flow) acts in parallel with diffusive flux. The DGM can be written as an implicit relationship among molar concentrations, fluxes, concentration gradients and pressure gradient as

$$\sum_{l\neq k}\frac{[X_l]J_k - [X_k]J_l}{[X_T]\mathcal{D}_{kl}^e} + \frac{J_k}{\mathcal{D}_{k,kn}^e} = -\nabla[X_k] - \frac{B_g[X_k]}{\mu\mathcal{D}_{k,kn}^e}\nabla p. \tag{4.20}$$

Eq. 4.20 can be inverted to develop a direct formulation of the diffusive molar flux vector J_k as [73]

$$J_k = -\left[\sum_{l=1}^{K_g}\mathcal{D}_{kl}^{\mathrm{DGM}}\nabla[X_l] + \left(\sum_{l=1}^{K_g}\frac{\mathcal{D}_{kl}^{\mathrm{DGM}}[X_l]}{\mathcal{D}_{l,kn}^e}\right)\frac{B_g}{\mu}\nabla p\right]. \tag{4.21}$$

The first term on the right hand side of Eq. 4.21 represents the diffusive flux and the second term represents the viscous flux. $\mathcal{D}_{kl}^{\mathrm{DGM}}$ are defined as DGM diffusion coefficients given as [73]

$$\mathcal{D}_{kl}^{\mathrm{DGM}} = \mathscr{H}^{-1}, \tag{4.22}$$

where the elements of the $\mathscr{H}$ matrix are

$$h_{kl} = \left[\frac{1}{\mathcal{D}^{\mathrm{e}}_{k,kn}} + \sum_{j\neq k}\frac{X_j}{\mathcal{D}^{\mathrm{e}}_{kj}}\right]\delta_{kl} + (\delta_{kl}-1)\frac{X_k}{\mathcal{D}^{\mathrm{e}}_{kl}}. \tag{4.23}$$

The effective binary diffusivity $\mathcal{D}^{\mathrm{e}}_{kl}$ is given by

$$\mathcal{D}^{\mathrm{e}}_{kl} = \frac{\epsilon}{\tau}\mathscr{D}_{kl}. \tag{4.24}$$

The permeability B_g in Eq. 4.21 is given by Kozeny-Carman relationship [103]

$$B_g = \frac{\epsilon^3 d_p^2}{72\tau(1-\epsilon)^2}. \tag{4.25}$$

The effective Knudsen diffusion coefficient appearing in Eq. 4.21 is given by Eq. 4.9. More detailed descriptions of DGM are given elsewhere [104, 105, 106, 107].

4.3.5 Mean Transport Pore Model (MTPM)

The MTPM visualizes the porous medium as networks of cylindrical capillaries with radii distributed around the mean value $\bar{r}$. The width of this distribution is characterized by the mean value of the squared transport-pore radii $\bar{r^2}$ [108]. When the mean free path of the molecule is comparable with the transport pore diameter an implicit relationship between the concentration gradients and fluxes can be written as

$$\frac{J_k}{\mathcal{D}^{\mathrm{e}}_{k,kn}} + \sum_{k\neq l}\frac{[X_l]J_k - [X_k]J_l}{[X_{\mathrm{T}}]\mathcal{D}^{\mathrm{e}}_{kl}} = -\nabla[X_k], \tag{4.26}$$

this is nothing but the modified Maxwell-Stefan model (MMS). However, it should be noticed that the above equation does not include the flux due to viscous transport, which can be included in Eq. 4.26 to obtain the total flux. Unlike DGM the permeation transport in MTPM is treated differently. In DGM as well as in MTPM the permeation fluxes are given by the Darcy equation as

$$J^p_k = -\frac{B_{g,k}[X_k]}{\mu}\nabla p. \tag{4.27}$$

However, the permeation coefficients are treated differently in DGM and MTPM. The viscous flux term in DGM does not account for the permeation coefficient of individual mixture components, while MTPM accounts for the permeation coefficient of individual species as

$$B_k = \mathcal{D}^{\mathrm{e}}_{k,\mathrm{kn}}\frac{\omega\nu_{\mathrm{k}} + Kn_{\mathrm{k}}}{1+Kn_{\mathrm{k}}} + \frac{\bar{r}^2\epsilon p}{8\tau\mu}. \tag{4.28}$$

The parameter ω describes the details of wall slip condition (ω = 0.9, $\pi/4$, $3\pi/16$ etc. [98]) and ν_{k} is the square root of the relative molecular weight of the gas mixture component k

$$\nu_{\mathrm{k}} = \sqrt{\frac{W_k}{\sum_{j=1}^{K_g} X_j W_j}}. \tag{4.29}$$

The effective permeability given by Eq.4.28 is valid for bulk, Knudsen, and transition regimes. The net permeation flux can be expressed as the sum of permeation flux of individual mixture components

$$J^p = -\sum_{k=1}^{K_{\mathrm{g}}} B_{\mathrm{k}} \nabla [X_k]. \tag{4.30}$$

Combining the permeation flux and diffusive fluxes the implicit relationship among concentration gradients, pressure gradients and fluxes can be written as

$$\sum_{l \neq k} \frac{[X_l]J_k - [X_k]J_l}{[X_T]\mathcal{D}^{\mathrm{e}}_{kl}} + \frac{J_k}{\mathcal{D}^{\mathrm{e}}_{k,kn}} = -\nabla [X_k] - \left[\frac{B_k}{\mathcal{D}^{\mathrm{e}}_{k,kn}} + \sum_l \frac{[X_l]}{[X_T]} \frac{B_k - B_l}{\mathcal{D}^{\mathrm{e}}_{kl}} \right] \frac{1}{RT} \frac{[X_k]}{[X_T]} \nabla p. \tag{4.31}$$

4.4 General transport equations

In general a 2D or 3D flow field can be resolved for steady state conditions by solving the equation of continuity

$$\nabla \cdot (\rho \vec{u}) = 0 \tag{4.32}$$

and momentum

$$\nabla \cdot (\rho \vec{u}\vec{u}) = -\nabla p - \frac{2}{3} \nabla \cdot (\mu \nabla \vec{u}) + \nabla \cdot [\mu (\nabla \vec{u} + \nabla \vec{u}^{\mathrm{T}})] + \vec{F}. \tag{4.33}$$

In Eq. 4.33 $\vec{F}$ is zero for the plain media and in the porous media it is defined by Darcy's law as

$$\vec{F} = -\frac{\mu}{B_g} \vec{u}, \tag{4.34}$$

where μ is the viscosity and B_g is the permeability defined by Eq. 4.25. The species concentrations are solved by the species transport equation defined in the following form

$$\nabla \cdot (\rho \vec{u} Y_k) = -\nabla \cdot (W_k \vec{J_k}) + \dot{s_k} W_k A_{\mathrm{s}} \tag{4.35}$$

where Y_k is the mass fraction of k'th species in the mixture, $\dot{s_k}$ is the molar production rate of the species due to surface reactions defined by Eq. 2.3, W_k is the molecular mass and A_{s} is the specific area available for surface reactions. The flux $\vec{J_k}$ in Eq. 4.35 can be defined by Eq. 4.10, 4.21, 4.31, or 4.16.

The temperature field can be resolved by the energy balance equation

$$\nabla \cdot (\rho \vec{u} C_p T) = \nabla \cdot (k \nabla T) - \nabla \cdot \sum_{k}^{K_g} h_k \vec{J}_k W_k \tag{4.36}$$

The equations described in this sections are used to simulate the button cell presented in Chapter 6

4.5 Model reduction

The elliptic model equations described in section 4.4 with detailed heterogeneous chemistry and electrochemistry can turn out to be computationally expensive depending on the complexity of the geometry. However, by carefully formulating the governing equations it is quite possible to consider and simulate the cell geometry in terms of two independent variables. These one dimensional numerical models can serve as valuable design tools for SOFC applications. These models are reasonably fast taking few minutes on a personal computer. The equations described in this sections are used for the planar cell models presented in Chapter 7. In general in this model, the flow through the channels is modeled by plug flow equations and porous media transport is modeled by DGM explained in section 4.3.4

4.5.1 Heat and mass transport

Channel Flow

Flow through fuel and air channels is assumed to be one dimensional and laminar in nature. The plug flow equation for species continuity in the channel are given by

$$\frac{\partial(\rho_f Y_k)}{\partial t} = -\frac{\partial(\rho_f u Y_k)}{\partial z} + \frac{P_\mathrm{e}}{A_\mathrm{c}} J_k W_k, \quad k = 1, \ldots, K_g. \tag{4.37}$$

The velocity is calculated from the momentum equation

$$\frac{\partial(\rho_f u)}{\partial t} = -\frac{\partial(\rho_f u u)}{\partial z} + u \sum_{k=1}^{K_g} \frac{P_\mathrm{e}}{A_c} J_k W_k, \tag{4.38}$$

by neglecting the pressure drop in the flow channels. Here P_e is the perimeter associated with the membrane electrode assembly, and A_c is the cross sectional area of the channel. Axial diffusion can also be introduced into the channel flow Eq. 4.37 as

$$\frac{\partial(\rho_f Y_k)}{\partial t} = -\frac{\partial(\rho_f u Y_k)}{\partial z} - \frac{\partial(\rho_f V_k Y_k)}{\partial z} + \frac{P_\mathrm{e}}{A_\mathrm{c}} J_k W_k, \quad k = 1, \ldots, K_g. \tag{4.39}$$

The axial diffusion velocity v_k can be evaluated using multi-component formulation [56],

$$v_k = \frac{1}{X_k}\mathcal{D}_{km}\nabla X_k, \tag{4.40}$$

where $\mathcal{D}_{km}$ is the mixture average diffusion coefficient. Assuming constant pressure in the channels density is calculated from the ideal gas equation

$$\rho_f = \frac{p\bar{M}}{RT}. \tag{4.41}$$

In Eq. 4.37 and 4.38 J_k is the flux at the electrode channel interface and is calculated using dusty gas model (Eq. 4.21). Temperature in the flow channels is determined from the energy equation

$$\frac{\partial(\rho_f C_{pf} T_f)}{\partial t} = -\frac{\partial(u\rho_f C_{pf} T_f)}{\partial z} - \frac{h}{H_c}(T_f - T_e) + \frac{h}{H_c}(T_I - T_f). \tag{4.42}$$

The first term on the right hand side of Eq. 4.42 represents the transport of energy due to the bulk fluid flow, second and third terms represents the heat transfer from the channel to the electrode structure and heat transferred from the interconnect into the flow channels respectively. The heat transfer coefficient h is evaluated from Nusselt number

$$Nu = \frac{hD_h}{k}, \tag{4.43}$$

which is expressed empirically as [109]

$$Nu = 3.095 + 8.933\left(\frac{1000}{Gz}\right)^{-0.5386}\exp\left(-\frac{6.7275}{Gz}\right) \tag{4.44}$$

where Graetz number Gz is given by

$$Gz = \frac{D_h}{z}RePr. \tag{4.45}$$

Various dimensions used in the above equations are schematically represented in Fig. 4.1

Porous media transport

Species transport through the porous media is assumed to be one dimensional along the thickness of the porous structure and is given by

$$\frac{\partial(\epsilon\rho_f Y_k)}{\partial t} = -\frac{\partial(J_k W_k)}{\partial y} + \dot{s}_k W_k A_s. \tag{4.46}$$

Where $\dot{s}_k$ is the heterogeneous production rate of the chemical species k and A_s is the specific catalyst area available for surface reactions. The total density of the gas-phase within the

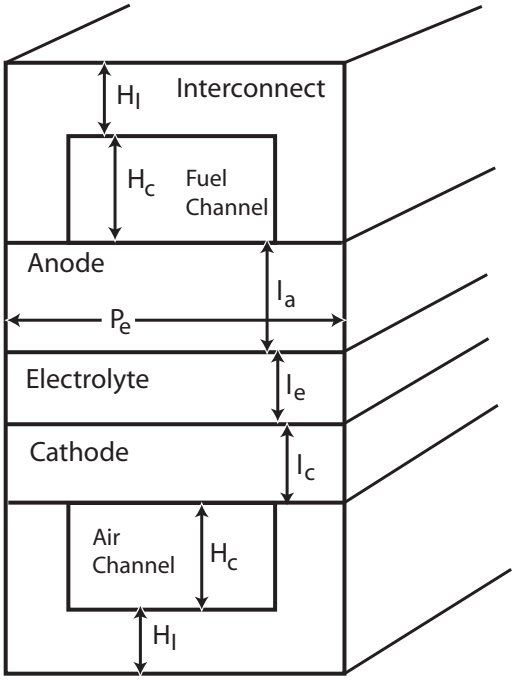

Figure 4.1: Schematic representation of various dimensions used in the model equations.

porous structure can be calculated from

$$\frac{\partial(\epsilon\rho_f)}{\partial t} = -\sum_{k=1}^{K_g} \frac{\partial(J_k W_k)}{\partial y} + \sum_{k=1}^{K_g} \dot{s}_k W_k A_s. \tag{4.47}$$

In the above equations the fluxes J_k are evaluated using DGM. Assuming the reaction heat is released on the solid surface the heat balance equation within the porous structure can be written as

$$\frac{\partial(\rho C_p T)}{\partial t} = \nabla \cdot (k_{\text{eff}} \nabla T) - \sum_{k=1}^{K_g} \dot{s}_k W_k A_{\text{s}} h_k \tag{4.48}$$

The first term on the right hand side represents heat transfer due to conduction and second term represents the heat released due to heterogeneous reactions within the electrodes which vanishes in the case of cathode. Two source terms, the radiative heat source term Q_{r}, and the convective heat source term Q_{h} enters Eq. 4.48 as boundary condition at the interface between electrode and the flow channel, and the electrochemical heat source term Q_{e} enters as boundary condition at the interface between the anode and the electrolyte. The radiative heat transfer between the interconnect and the outer most discretised cell in the porous electrode is given by

$$Q_{\text{r}} = \frac{1}{\delta y}\left[\frac{\sigma\left(T_I^4 - T^4\right)}{1/e_I + 1/e - 1}\right]. \tag{4.49}$$

The convective heat transfer between the fluid in the channel and the outer most discretised cell in the porous electrode is given by

$$Q_{\mathrm{h}} = \frac{h}{\delta y}(T_f - T). \tag{4.50}$$

δy appearing in Eq. 4.49 and Eq. 4.50 results from the finite volume integration over the discretised cells and must have a finite value. The global charge transfer reaction at the three-phase interface can be written as

$$\mathrm{H_2} + \mathrm{O^{2-}} \rightarrow \mathrm{H_2O} + 2\mathrm{e^-}, \tag{4.51}$$

however, only a part of the energy change during the reaction is released as heat, which amounts to

$$Q_{\mathrm{e}} = -\frac{T\Delta S}{\delta y}\frac{i}{2F}. \tag{4.52}$$

Assuming one dimensional transport in the electrolyte, the heat balance can be written as

$$\frac{\partial\left(\rho C_p T\right)}{\partial t} = \frac{\partial}{\partial z}\left(k\frac{\partial T}{\partial z}\right) + \frac{i^2}{\sigma_{\mathrm{e}}} \tag{4.53}$$

The last term in the above equation represents the ohmic heating due to ion transport in the electrolyte.

Interconnect

Assuming one dimensional transport the heat balance equation for the interconnect can be summarized as

$$\frac{\partial(\rho C_p T_I)}{\partial t} = \frac{\partial}{\partial z}\left(k\frac{\partial T_I}{\partial z}\right) + \frac{h}{H_I}(T_f - T_I) - \frac{1}{H_I}\left[\frac{\sigma\left(T_I^4 - T^4\right)}{1/e_I + 1/e - 1}\right] \tag{4.54}$$

The first term on the right hand side represents the conduction within the interconnect, second and third term represents the heat transferred to/from the channel to the interconnect and the radiation transfer to/from the interconnect to the electrode structure. Eqs. 4.48, 4.53, and 4.54 requires boundary conditions at $z = 0$ and $z = L$ which are given by

$$\left.\frac{\partial T}{\partial z}\right|_{z=0} = 0, \qquad \left.\frac{\partial T}{\partial z}\right|_{z=L} = 0. \tag{4.55}$$

The inlet conditions also serve as the initial condition. A schematic representation of the cell assembly with the application of various heat source terms and boundary conditions is shown in Fig.4.2.

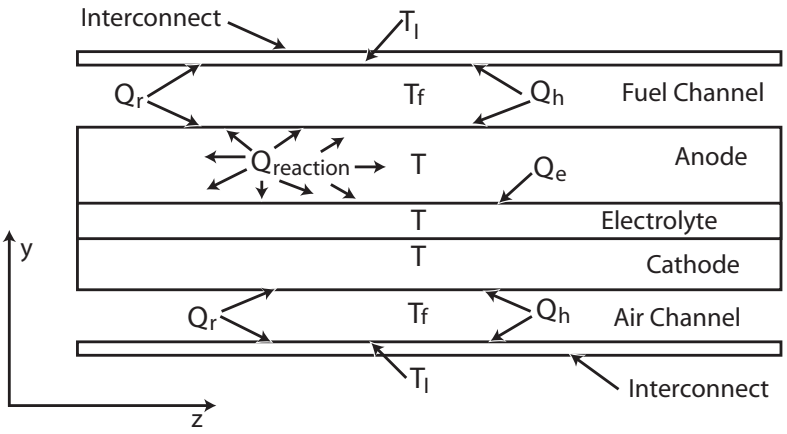

Figure 4.2: Demonstration of the application of various heat source terms, temperatures, and boundary conditions.

The reaction heat Q_{reaction} is released everywhere on the anode and is given by

$$Q_{\text{reaction}} = \sum_{k=1}^{K_g} \dot{s}_k W_k A_s h_k, \tag{4.56}$$

which is the last term on the right hand side of Eq. 4.48.

Modeling radiative heat transfer in SOFC is a complex process and the radiative transport within the semitransparent electrodes and electrolyte and surface to surface heat transfer must be accounted for an accurate calculation. However, an exact knowledge of phenomenological properties like absorption coefficient, refractive index, scattering coefficient, emissivity, reflectivity, etc. are severe obstacle to model radiative heat transport in SOFC electrodes and electrolyte. A detailed discussion of radiation heat transfer in SOFC is given elsewhere [110,111,112,113]. In an analysis of spectral radiation in SOFC electrodes Damm et al. [111] have proved that the radiation effects in SOFC electrodes are minimal and can safely be neglected. Therefore, in the present work only surface to surface radiation is considered. Since the planar geometry considered here is of high aspect ratio (L/d≈50) the surfaces can be treated as black bodies with emissivity e=1 [110] .

Chapter 5

Coupling of transport and reaction in porous media

Porous media finds extensive application in chemical engineering. In certain cases they are simply used to increase the mass transfer rate between two distinct phases, while in certain other cases they are used to disperse the catalyst effectively. Catalytic packed beds are an integral part of any chemical production industry. Solid Oxide Fuel Cells are class of electrochemical devices where porous media finds important application. Over the years many models have been developed to study the transport processes in porous media, starting from simple Fickian approach to complex Dusty Gas Model (DGM). However, very little is done to validate the accuracy of these models under reaction conditions, especially with multi-component species mixtures.

In an attempt to critically evaluate the accuracy of various models, this chapter focuses on the usage of DGM, MTPM, MFM, MMS, and GMS models applied to reacting porous media. The work presented here is basically an extension of the work reported by Hecht et al. [64], who describes a reactor environment that is much more amenable for the investigation of thermo-catalytic chemistry than a fuel cell itself. The anode of a fuel cell provides ample opportunity for heterogeneous reforming reactions. The multi-component gas mixture is transported from the fuel channel towards the three-phase boundary by diffusional flow and viscous flow. On their way towards the three-phase interface the HCs react with CO_2 and H_2O formed at the interface as a result of electrochemical charge transfer chemistry. Therefore, a steep gradient in species profile exists across the anode thickness. An important difference between the work reported by Hecht et al. and the work presented here is in the applied elementary step mechanism. In the investigation carried out by Hecht et al. the mechanism was evaluated only at 800°C, however for the results presented in this chapter an extended version of the mechanism is employed. The mechanism is made to be consistent in both enthalpy and entropy over the temperature range of 500°C to 1800 °C.

5.1 Experimental setup

The experiment reported by Hecht et al. [64] treats the anode of a SOFC as the reacting porous medium. A 750 μm thick anode is sandwiched between two flow channels of 6.25 mm^2 cross sectional area. The flow channels are 5 cm long. One flow channel carries the species that typically are present in the fuel channel of a real fuel cell, while the other channel carries mainly reforming gas (CO_2 and H_2O) and fuel. A schematic representation of the flow configuration is shown in Fig. 5.1. Three cases are described in the report, (i) dry reforming, (ii) steam-reforming, and (iii) combination of both. In order to follow up the work of Hecht et al., the same naming conventions used by the authors are adopted here. One of the flow channels is referred as fuel channel, while the other is referred as electrolyte channel.

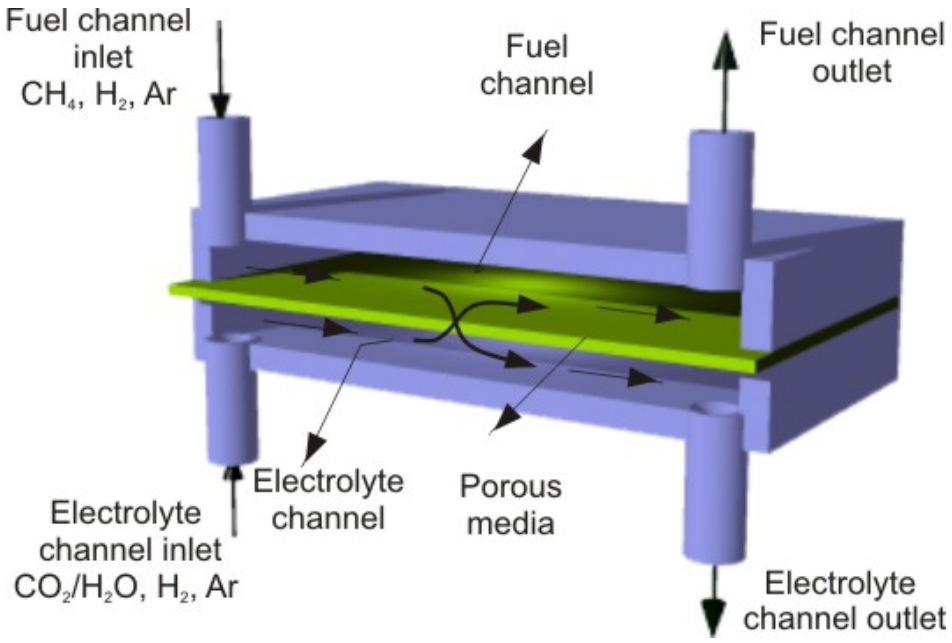

Figure 5.1: Schematic representation of the experimental setup. Green represents the porous anode which is sandwiched between two flow channels. One of the channels is fed with fuel gas and the other channel is fed with reforming gas such as H_2O or CO_2

The following sections present the comparison between the experiments and the various porous media transport models. For modeling purpose the code developed by Dr. H. Zhu (Colorado School of Mines, Golden, USA) has been used [64]. The code is very much similar to the SOFC code reported in Chapter 7 without the electrochemistry model and hence the governing equations and the computation method are not explained here. Flow through the channels is assumed to be plug flow in nature and the transport across the thickness of the porous medium is assumed to be one dimensional. Various porous media transport models employed in the calculations presented in this chapter is discussed in detail in Chapter 4. The porous medium is divided into 80 finite volume cells and the reactor is discretized in the axial direction into 100 cells. The structural properties of the porous media used in the study is given in Table 5.1. Only the cases of dry reforming and steam reforming is considered here.

In all cases the experiments were carried out at 800°C and the flow rates were so chosen to visit the kinetic regimes rather than equilibrium. For all the cases presented here no carbon deposition was observed due to the high dilution and high concentration of reforming agents present. This possibly increased the accuracy of the calculation since the heterogeneous reforming mechanism was not developed for carbon deposition conditions.

Table 5.1: Structural parameters for the porous media

Parameters	Value	Units
length	5.0	cm
Porosity	35	%
Tortuosity	3.5	
Pore diameter	0.7	μm
particle diameter	1.0	μm
Specific area	1080	cm^{-1}

5.2 Dry reforming: comparison between experiment and various models

In the case of dry reforming the inlet to the fuel channel is a mixture of 77.2% Ar, 2.8% H_2, and 20% CH_4, while, the electrolyte channel inlet is a mixture of 48.2% Ar, 1.8% H_2, and 50% CO_2. The inlet flow rates range from 50 to 150 sccm (standard cubic centimeter). Figure 5.2 depicts the profile of various species in the flow channels as well as across the thickness of the porous medium at selected axial positions as predicted by DGM. The bottom panel shows the mole fractions within the fuel channel and the top panel shows the mole fractions within the electrolyte channel. As expected, the CO_2 concentration decreases in the electrolyte channel and increases slightly in the fuel channel. Since the porous medium permits the transport of species between the two channels CO_2 diffuses from the electrolyte channel towards the fuel channel due to its high concentration in the electrolyte channel. While CH_4 flux is from the fuel channel towards the electrolyte channel due to its high concentration in the fuel channel. It is quite evident from the middle panels that CO_2 and CH_4 always have opposite fluxes. Dry reforming proceeds within the porous media and consequently the mole fraction of H_2 and CO increases in both the channels. However, dry reforming results in higher CO concentration compared to steam reforming. Concentration of CO increases almost at the same rate in both the channels. Hydrogen mole fraction remains slightly higher in the fuel channel possibly due to the higher inlet concentrations in the fuel channel relative to the electrolyte channel. Ar which is present in higher concentrations in the fuel channel diffuse across the porous media resulting in decreased concentration along the fuel channel length.

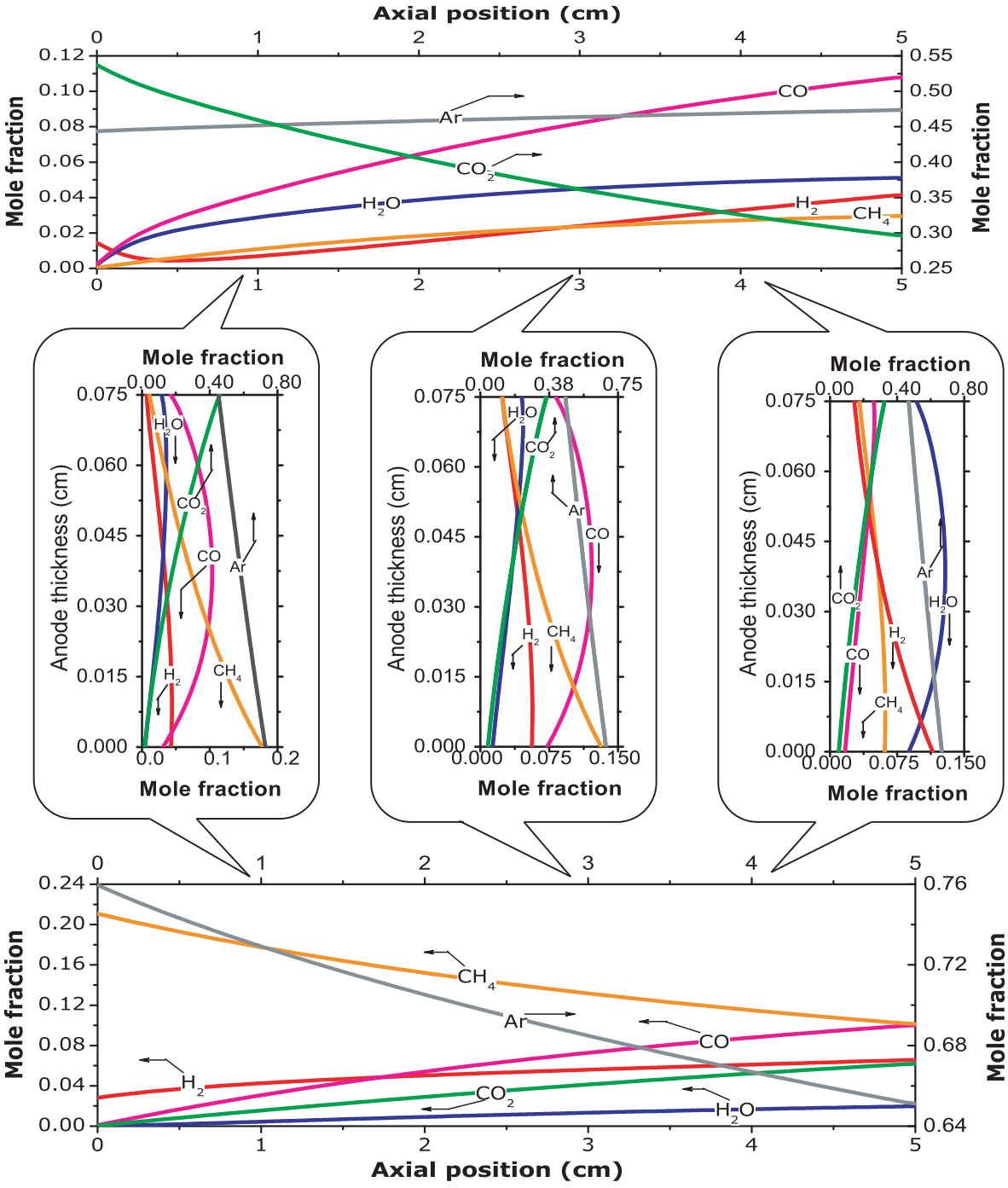

Figure 5.2: Profiles of various species in the fuel channel and the electrolyte channel for dry reforming case at 50 sccm and 800°C based on DGM. The bottom panel shows the profiles within the fuel channel and the top panel stands for the profiles within the electrolyte channel. The three middle panels show the mole fraction profiles across the thickness of the porous medium at three different locations.

Although the objective of this chapter is to compare the various model against experimental observation to identify the model leading to best predictions under reaction conditions, it turned out to be rather a difficult task, partly also due to the accuracy of the chemistry model. For certain species some model outperformed the others. However, in general DGM and MFM gave reasonably good results for all cases.

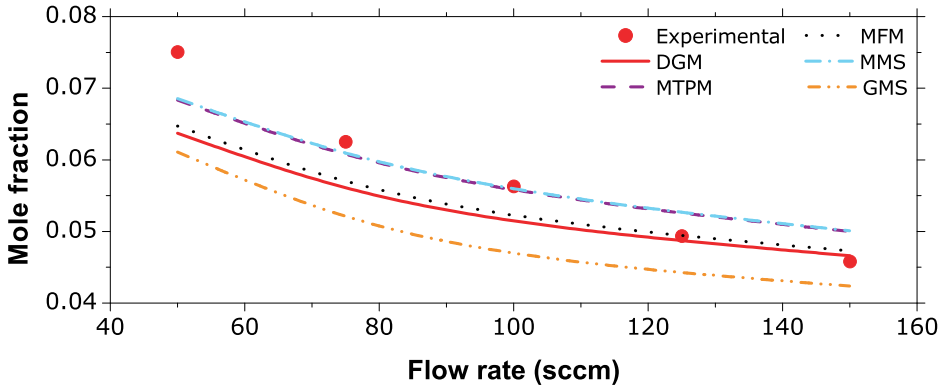

Figure 5.3: Comparison of experimental measurements and various model predictions for H_2 at the fuel channel exhaust. Nominal inlet mole fractions at the fuel channel are 20% CH_4, 2.8% H_2, and 77.2% Ar. Inlet mole fractions at the electrolyte channel are 50% CO_2, 1.75% H_2 and 48.25% Ar.

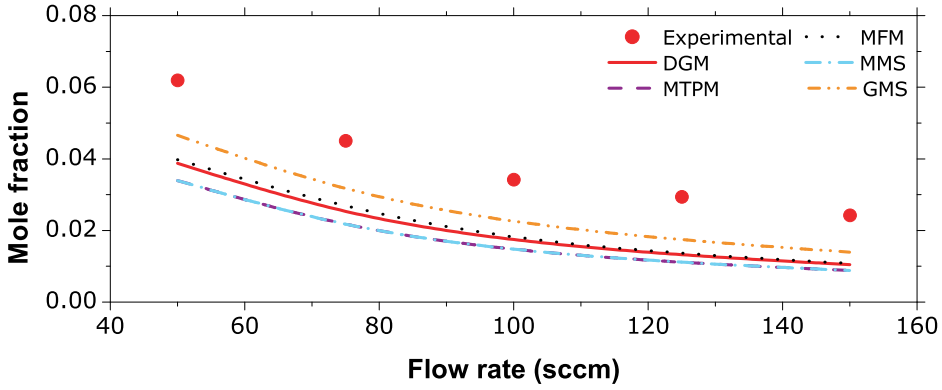

Figure 5.4: Comparison of experimental measurements and various model predictions for H_2 at the electrolyte channel exhaust. Nominal inlet mole fractions at the fuel channel are 20% CH_4, 2.8% H_2, and 77.2% Ar. Inlet mole fractions at the electrolyte channel are 50% CO_2, 1.75% H_2 and 48.25% Ar.

Figures 5.3 and 5.4 present the comparison of various model predictions and experimental measurements for H_2. Figure 5.3 compares the fuel channel predictions and measurement, and Fig. 5.4 compares predictions and measurements for the electrolyte channel. The fuel channel outlet concentrations are rather well predicted by MTPM and MMS. While for the electrolyte channel all the models under predict H_2 mole fractions. Since H_2 is a reaction product its concentration decreases with increasing flow rate in both channels.

An analogous comparison of predicted and measured mole fractions of H_2O for fuel channel and electrolyte channel outlets are displayed in Figs. 5.5 and 5.6, respectively. All the models gave reasonably good results for the electrolyte channel exhaust. However, for the fuel channel the MTPM and MMS by far under predicted the mole fraction of H_2O. It should be noticed that all the H_2O observed in the experiments reported here is a reaction product resulting from the reverse water-gas shift reaction. As expected the product H_2O decreases with increasing flow rate. Figs. 5.7 and 5.8, respectively, show the comparison between

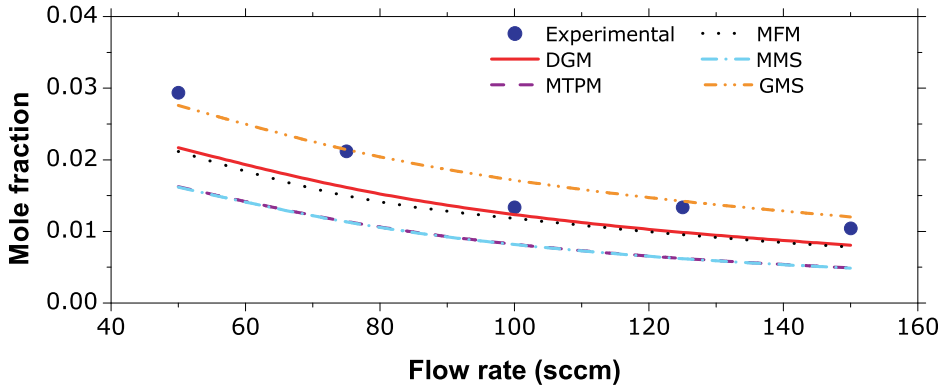

Figure 5.5: Comparison of experimental measurements and various model predictions for H_2O at the fuel channel exhaust. Nominal inlet mole fractions at the fuel channel are 20% CH_4, 2.8% H_2, and 77.2% Ar. Inlet mole fractions at the electrolyte channel are 50% CO_2, 1.75% H_2 and 48.25% Ar.

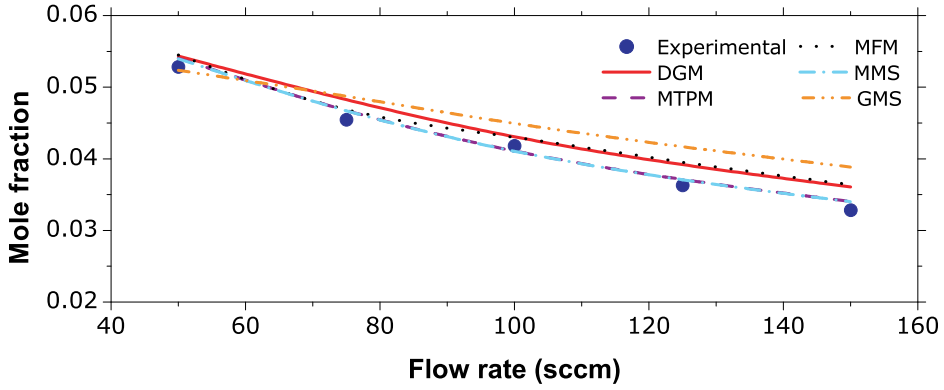

Figure 5.6: Comparison of experimental measurements and various model predictions for H_2O at the electrolyte channel exhaust. Nominal inlet mole fractions at the fuel channel are 20% CH_4, 2.8% H_2, and 77.2% Ar. Inlet mole fractions at the electrolyte channel are 50% CO_2, 1.75% H_2, and 48.25% Ar.

measurements and model predictions of the mole fraction of CO for fuel and electrolyte channel outlets. Since CO is a product of reforming reactions its concentration decreases with increasing flow rate. However, dry reforming resulted in much higher CO production than H_2. All the models work well in reproducing the experimental observations.

Predictions and measurements of the mole fraction of CO_2 for the exhausts of fuel and electrolyte channel are shown in Figs. 5.9 and 5.10 respectively. For both channels DGM and MFM predictions are in good agreement with experimental observations. GMS over predicts the mole fraction in the fuel channel exhaust and under predicts the mole fraction in the electrolyte channel exhaust. While MTPM and MMS under predicts the mole fraction in the fuel channel exhaust and over predicts the mole fraction in the electrolyte channel exhaust. The mole fraction of CO_2 increases with increasing flow rate within the electrolyte channel exhaust due to the lower extent of reforming at high flow rates. While in the fuel channel the

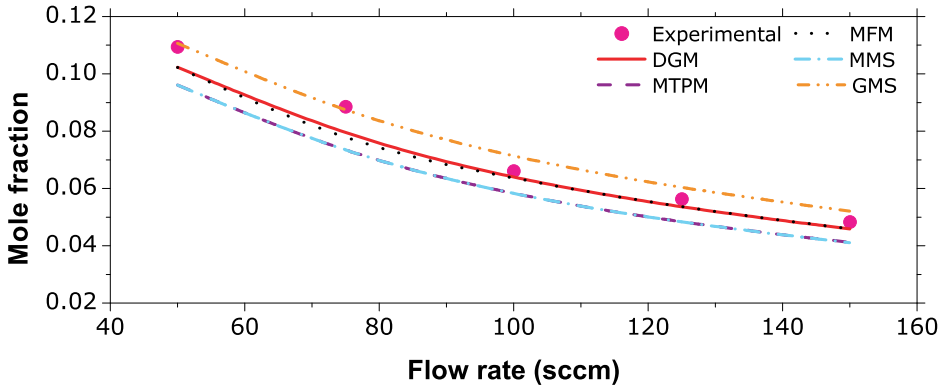

Figure 5.7: Comparison of experimental measurements and various model predictions for CO at the fuel channel exhaust. Nominal inlet mole fractions at the fuel channel are 20% CH_4, 2.8% H_2, and 77.2% Ar. Inlet mole fractions at the electrolyte channel are 50% CO_2, 1.75% H_2, and 48.25% Ar.

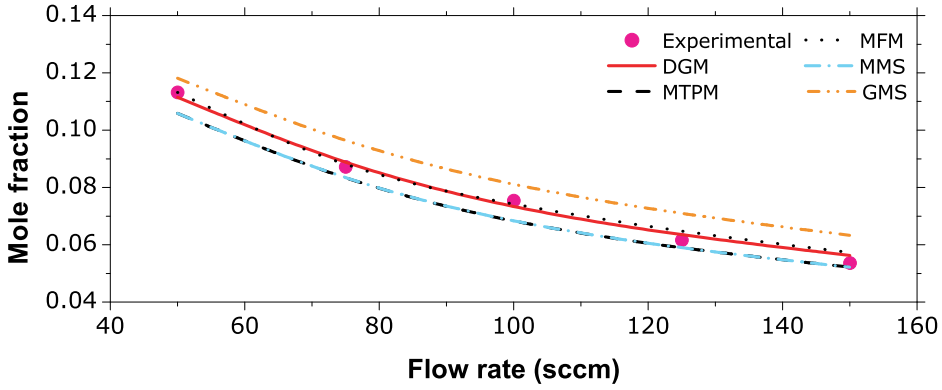

Figure 5.8: Comparison of experimental measurements and various model predictions for CO at the electrolyte channel exhaust. Nominal inlet mole fractions at the fuel channel are 20% CH_4, 2.8% H_2, and 77.2% Ar. Inlet mole fractions at the electrolyte channel are 50% CO_2, 1.75% H_2, and 48.25% Ar.

concentration of CO_2 decreases with increasing flow rate. The short residence time at higher flow rates results in much less CO_2 reaching the fuel channel.

The mole fractions of CH_4 in the fuel channel exhaust are presented in Fig. 5.11 and the mole fractions of CH_4 in the electrolyte channel exhaust are displayed in Fig. 5.12. For both cases DGM and MFM work well in predicting the experimental observations. However, for electrolyte exhaust the observations are best matched by MTPM and MMF predictions, and GMS predictions are in best agreement with experimental observations for fuel channel exhaust. Similar to the case of CO_2 the concentration of CH_4 in the fuel channel outlet increases with increasing flow rate, while the concentration decreases in the electrolyte channel outlet. All the CH_4 present in the electrolyte exhaust results from the diffusion of CH_4 across the porous medium from the fuel channel to the electrolyte channel. Due to the decreasing

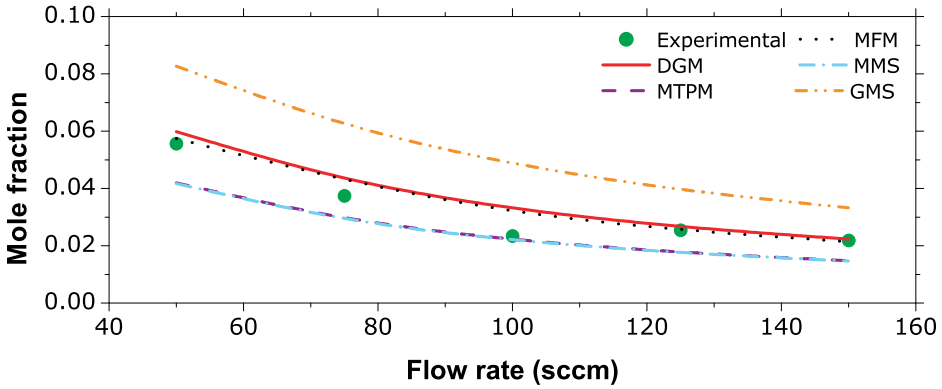

Figure 5.9: Comparison of experimental measurements and various model predictions for CO_2 at the fuel channel exhaust. Nominal inlet mole fractions at the fuel channel are 20% CH_4, 2.8% H_2, and 77.2% Ar. Inlet mole fractions at the electrolyte channel are 50% CO_2, 1.75% H_2, and 48.25% Ar.

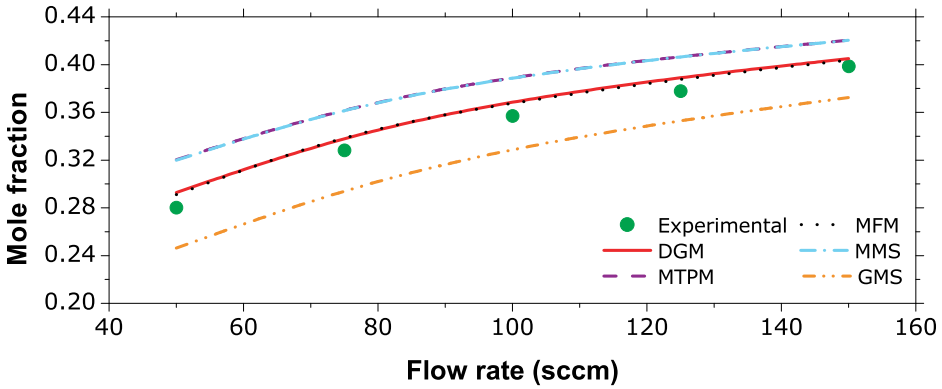

Figure 5.10: Comparison of experimental measurements and various model predictions for CO_2 at the electrolyte channel exhaust. Nominal inlet mole fractions at the fuel channel are 20% CH_4, 2.8% H_2, and 77.2% Ar. Inlet mole fractions at the electrolyte channel are 50% CO_2, 1.75% H_2, and 48.25% Ar.

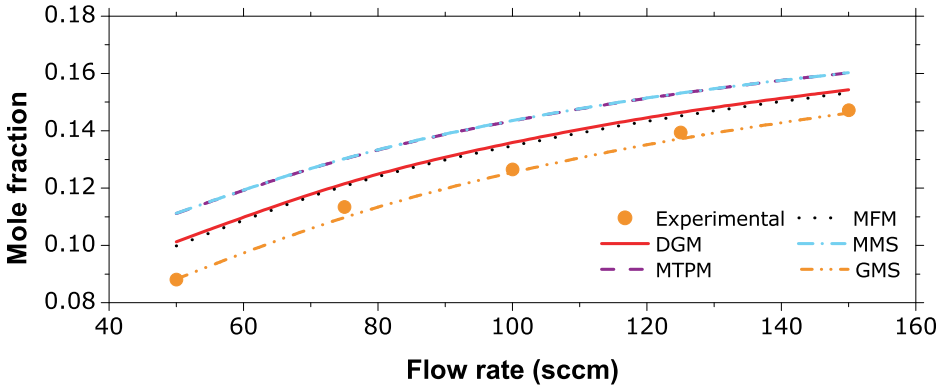

Figure 5.11: Comparison of experimental measurements and various model predictions for CH_4 at the fuel channel exhaust. Nominal inlet mole fractions at the fuel channel are 20% CH_4, 2.8% H_2, and 77.2% Ar. Inlet mole fractions at the electrolyte channel are 50% CO_2, 1.75% H_2, and 48.25% Ar.

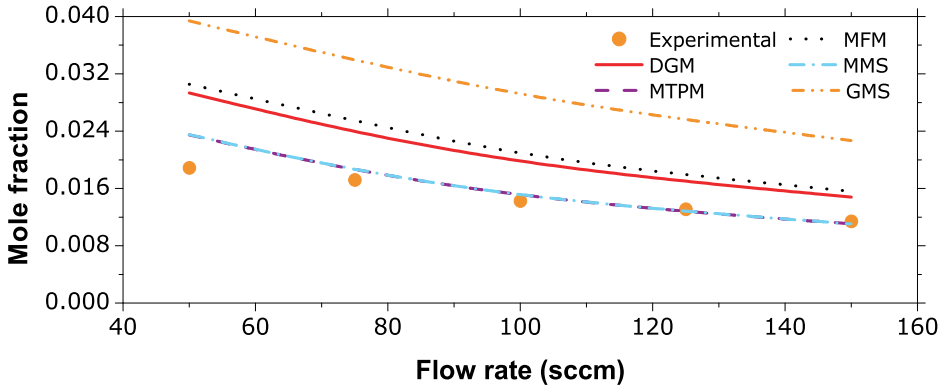

Figure 5.12: Comparison of experimental measurements and various model predictions for CH_4 at the electrolyte channel exhaust. Nominal inlet mole fractions at the fuel channel are 20% CH_4, 2.8% H_2, and 77.2% Ar. Inlet mole fractions at the electrolyte channel are 50% CO_2, 1.75% H_2, and 48.25% Ar.

conversion with increasing flow rate, the mole fraction of CH_4 in the fuel channel outlet increases with increasing flow rate. However, the shorter residence time leads to lower CH_4 fractions reaching the electrolyte channel, resulting in a decreasing mole fraction.

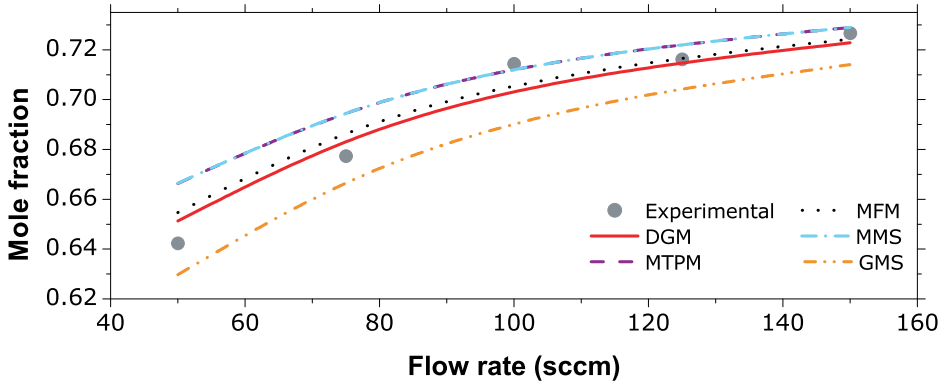

Figure 5.13: Comparison of experimental measurements and various model predictions for Ar at the fuel channel exhaust. Nominal inlet mole fractions at the fuel channel are 20% CH_4, 2.8% H_2, and 77.2% Ar. Inlet mole fractions at the electrolyte channel are 50% CO_2, 1.75% H_2, and 48.25% Ar.

Argon used as a diluent is present at the inlet of both the channels. Figs. 5.13 and 5.14 show the molar fraction of Ar in the fuel channel exhaust and the electrolyte channel exhaust respectively. For both cases DGM and MFM predictions are in good agreement with experimental measurements.

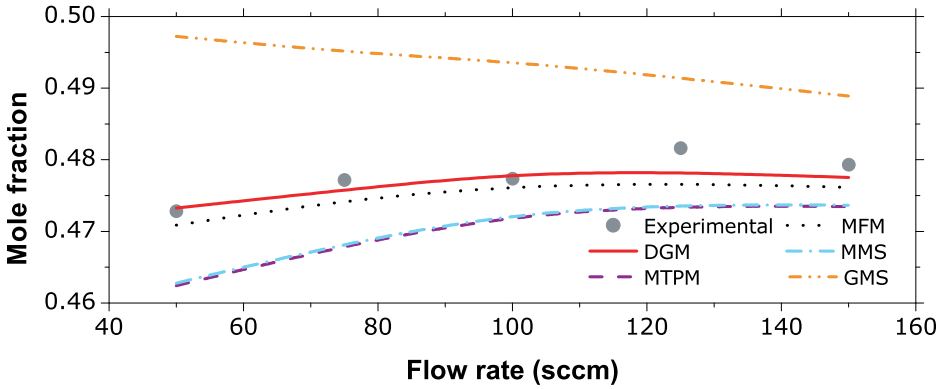

Figure 5.14: Comparison of experimental measurements and various model predictions for Ar at the electrolyte channel exhaust. Nominal inlet mole fractions at the fuel channel are 20% CH_4, 2.8% H_2, and 77.2% Ar. Inlet mole fractions at the electrolyte channel are 50% CO_2, 1.75% H_2, and 48.25% Ar.

5.3 Steam reforming: comparison between experiment and various models

For steam reforming, the composition of the feed to the fuel channel is the same as in the case of dry reforming. i.e. 77.2% Ar, 2.8% H_2, and 20% CH_4. While the composition of the feed to the electrolyte channel is changed to 48% H_2O, 1.8% H_2, and 50.2% Ar. Figure 5.15 demonstrates the species profile in the flow channels as well as across the thickness of porous medium at selected axial positions. Quite evidently, steam reforming results in higher H_2 concentrations than CO. While dry reforming results in higher CO concentration than H_2. Furthermore, steam reforming resulted in higher CH_4 conversion. Except these two changes the general trends for steam reforming are similar to those observed in the case of dry reforming. Here, CH_4 as H_2O have opposite fluxes. H_2O has a flux away from the electrolyte channel into the fuel channel, while CH_4 flux is from fuel channel into the electrolyte channel. Argon fed to the fuel channel with higher concentration has flux into the electrolyte channel. All these trends are observed in dry reforming as well. In both the flow channels the concentration of H_2 increases along the reactor length as a result of reforming reactions.

Figures 5.16 and 5.17 respectively show the experimentally measured as well as the predicted mole fractions of H_2 from the fuel and the electrolyte channel exhausts. The mole fractions of H_2 decrease with increasing flow rate due to decreasing extent of reforming reactions. All the models work well in predicting the experimental observations.

Comparison of H_2O exhaust mole fractions from both the channels is shown in Fig. 5.18 and Fig. 5.19. Former presents the exit mole fraction from the fuel channel and the latter presents exit mole fraction from the electrolyte channel. At the exit of the electrolyte channel, the mole fraction of H_2O increases with increasing flow rate due to the lesser extend of reforming reactions. While at at the fuel channel exit the mole fraction of water decreases

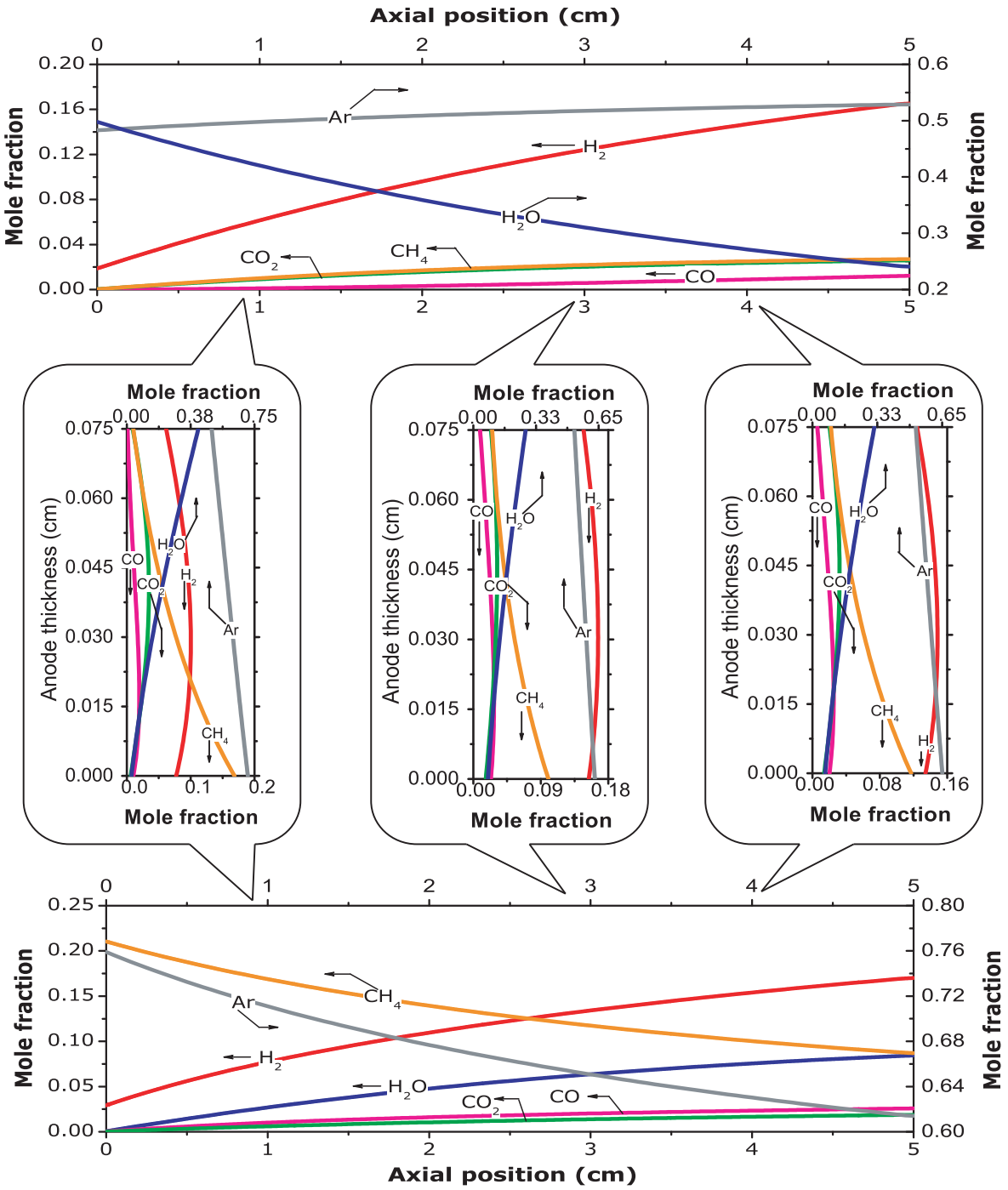

Figure 5.15: Profiles of various species in the fuel channel and the electrolyte channel for steam reforming case at 50 sccm and 800°C based on DGM. The bottom panel shows the profiles within the fuel channel and the top panel stands for the profiles within the electrolyte channel. The three middle panels show the mole fraction profiles across the thickness of the porous medium at three different locations.

with increasing flow rate due to the short residence time. It should be noticed that, H_2O in the fuel exit can result from the diffusive transport of H_2O from electrolyte channel or from reverse water-gas shift as observed in the case of dry reforming. For both channel exits DGM and MFM predictions are in good agreement with measurements. GMS model over

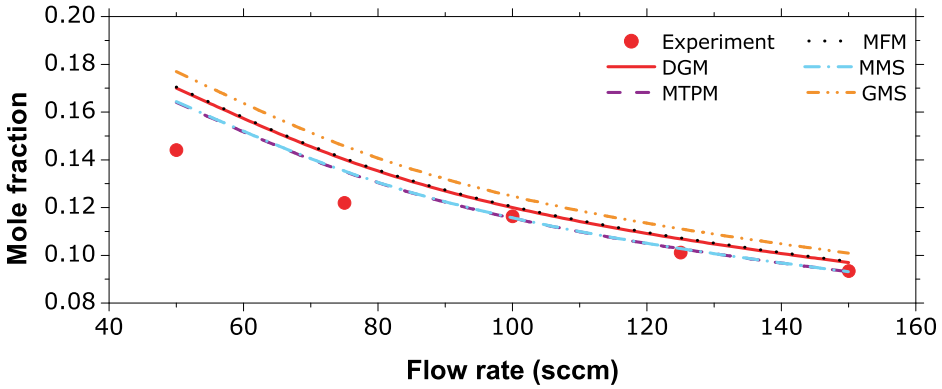

Figure 5.16: Comparison of experimental measurements and various model predictions for H_2 at the fuel channel exhaust. Nominal inlet mole fractions at the fuel channel are 20% CH_4, 2.8% H_2, and 77.2% Ar. Inlet mole fractions at the electrolyte channel are 48% H_2O, 1.8% H_2, and 50.2% Ar.

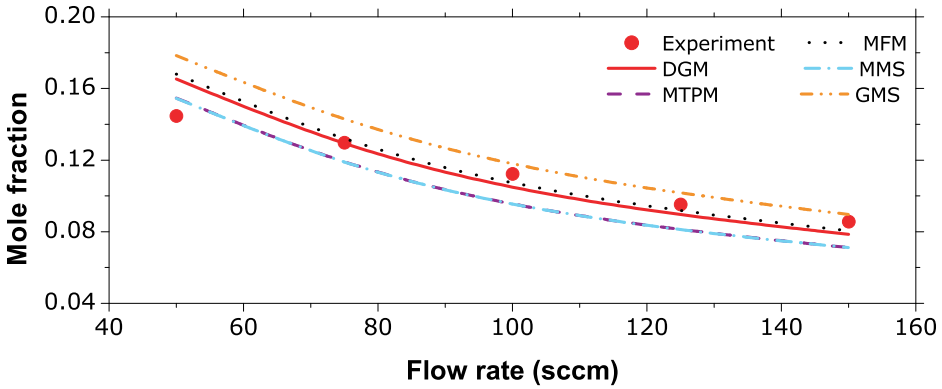

Figure 5.17: Comparison of experimental measurements and various model predictions for H_2 at the electrolyte channel exhaust. Nominal inlet mole fractions at the fuel channel are 20% CH_4, 2.8% H_2, and 77.2% Ar. Inlet mole fractions at the electrolyte channel are 48% H_2O, 1.8% H_2, and 50.2% Ar.

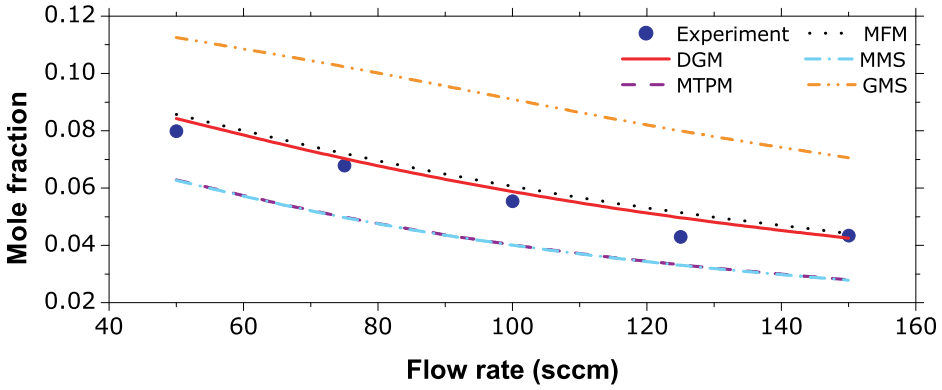

Figure 5.18: Comparison of experimental measurements and various model predictions for H_2O at the fuel channel exhaust. Nominal inlet mole fractions at the fuel channel are 20% CH_4, 2.8% H_2, and 77.2% Ar. Inlet mole fractions at the electrolyte channel are 48% H_2O, 1.8% H_2, and 50.2% Ar.

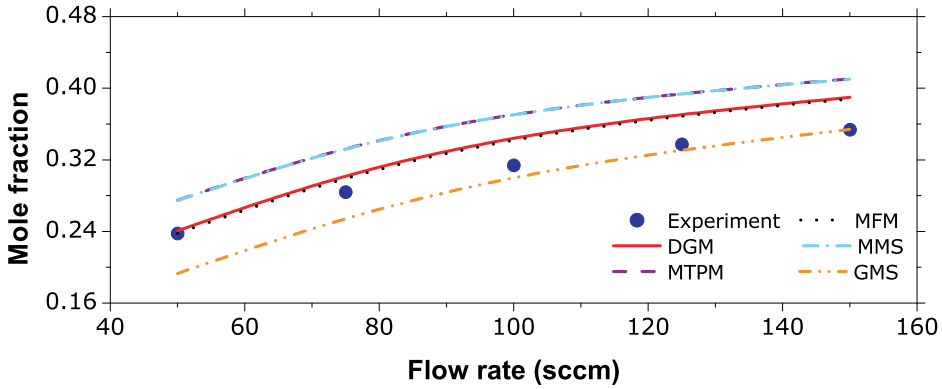

Figure 5.19: Comparison of experimental measurements and various model predictions for H_2O at the electrolyte channel exhaust. Nominal inlet mole fractions at the fuel channel are 20% CH_4, 2.8% H_2, and 77.2% Ar. Inlet mole fractions at the electrolyte channel are 48% H_2O, 1.8% H_2, and 50.2% Ar.

predicts the exit composition of H_2O in the fuel channel, however the predictions are in good agreement for electrolyte channel exhaust.

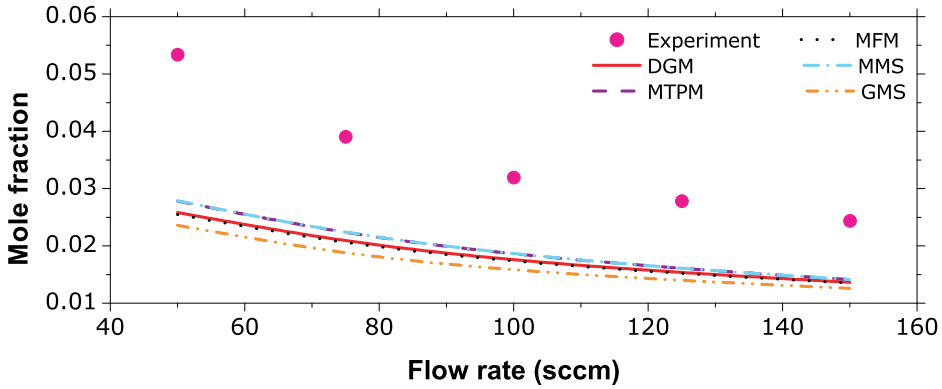

Figure 5.20: Comparison of experimental measurements and various model predictions for CO at the fuel channel exhaust. Nominal inlet mole fractions at the fuel channel are 20% CH_4, 2.8% H_2, and 77.2% Ar. Inlet mole fractions at the electrolyte channel are 48% H_2O, 1.8% H_2, and 50.2% Ar.

Figures 5.20 and 5.21 represent the measured and predicted mole fractions of CO from the fuel and electrolyte channel exhaust, respectively, as a function of flow rate. All the models fail to predict the measured values for CO, possibly also due to inaccuracy of the elementary mechanism used here. However, all the models predict decreasing CO content in the exhaust with increasing flow rate, which is consistent with the experiments.

The comparisons of model predictions and measurements of the mole fraction of CO_2 at the exhaust of the fuel and the electrolyte channels, for various flow rates are shown respectively in Fig. 5.22 and Fig. 5.23. For both cases MTPM and MMS predictions are in excellent agreement with measured values. DGM and MFM also work well in reproducing

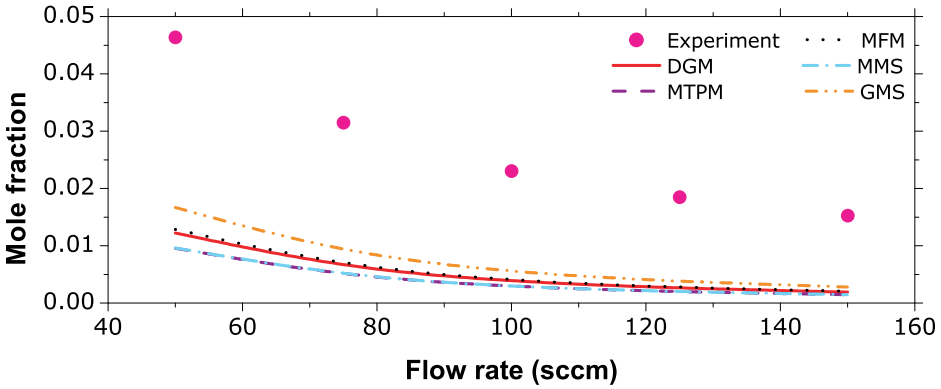

Figure 5.21: Comparison of experimental measurements and various model predictions for CO at the electrolyte channel exhaust. Nominal inlet mole fractions at the fuel channel are 20% CH_4, 2.8% H_2, and 77.2% Ar. Inlet mole fractions at the electrolyte channel are 48% H_2O, 1.8% H_2, and 50.2% Ar.

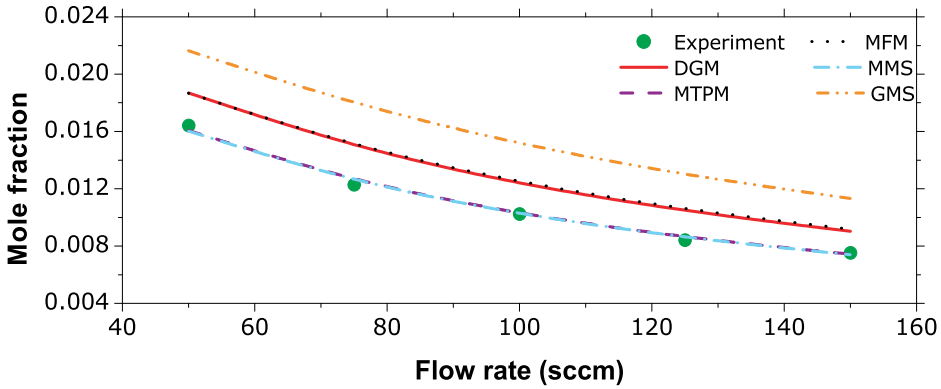

Figure 5.22: Comparison of experimental measurements and various model predictions for CO_2 at the fuel channel exhaust. Nominal inlet mole fractions at the fuel channel are 20% CH_4, 2.8% H_2, and 77.2% Ar. Inlet mole fractions at the electrolyte channel are 48% H_2O, 1.8% H_2, and 50.2% Ar.

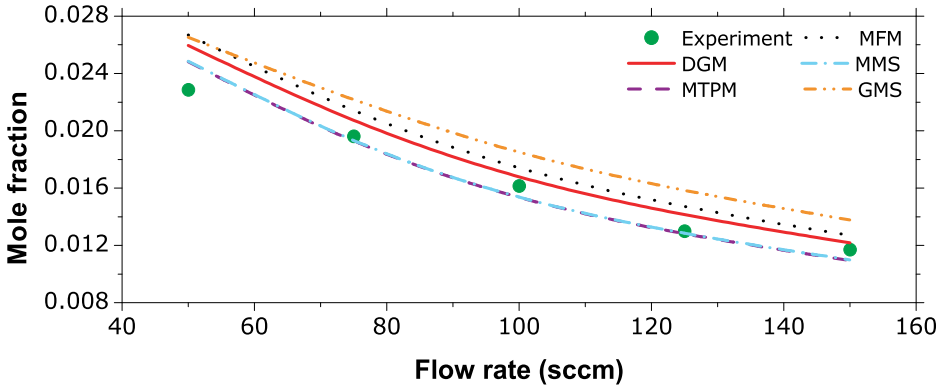

Figure 5.23: Comparison of experimental measurements and various model predictions for CO_2 at the electrolyte channel exhaust. Nominal inlet mole fractions at the fuel channel are 20% CH_4, 2.8% H_2, and 77.2% Ar. Inlet mole fractions at the electrolyte channel are 48% H_2O, 1.8% H_2, and 50.2% Ar.

the experimental observations. As expected the CO_2 mole fraction decreases with increasing flow rates. However, concentration of CO_2 in the exhaust of the electrolyte exceeds the concentration in the exhaust of the fuel channel.

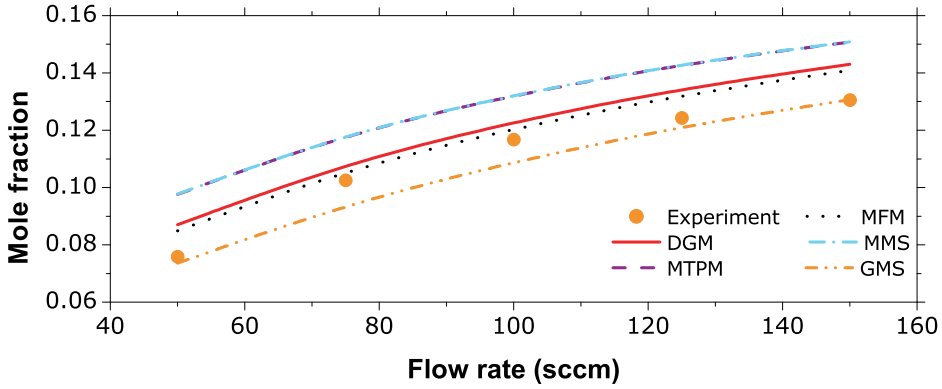

Figure 5.24: Comparison of experimental measurements and various model predictions for CH_4 at the fuel channel exhaust. Nominal inlet mole fractions at the fuel channel are 20% CH_4, 2.8% H_2, and 77.2% Ar. Inlet mole fractions at the electrolyte channel are 48% H_2O, 1.8% H_2 and 50.2% Ar.

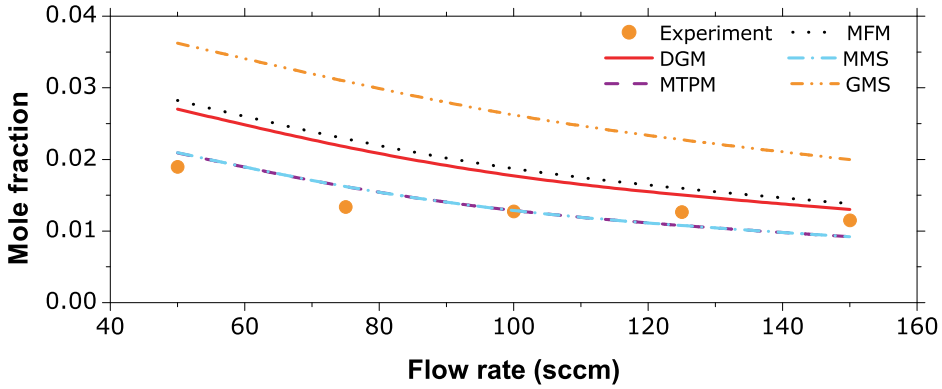

Figure 5.25: Comparison of experimental measurements and various model predictions for CH_4 at the electrolyte channel exhaust. Nominal inlet mole fractions at the fuel channel are 20% CH_4, 2.8% H_2, and 77.2% Ar. Inlet mole fractions at the electrolyte channel are 48% H_2O, 1.8% H_2 and 50.2% Ar.

Figures 5.24 and 5.25 depict the exit concentrations from the fuel channel and electrolyte channel for CH_4. Similar to the case of dry reforming CH_4 mole fractions in the fuel channel exit increases with increasing flow rates. While CH_4 mole fractions at the electrolyte channel exit decreases with increasing flow rate due to the short residence time.

Comparison between experiments and model predictions for Ar is shown in Figs. 5.26 and 5.27. The former represents the exit mole fraction from the fuel channel and the latter depicts the exit mole fraction from the electrolyte channel. As in the case of dry reforming higher flow rates resulted in higher Ar exit mole fractions from the fuel channel. DGM and MFM predictions are in good agreement with experimental observation for fuel channel exit.

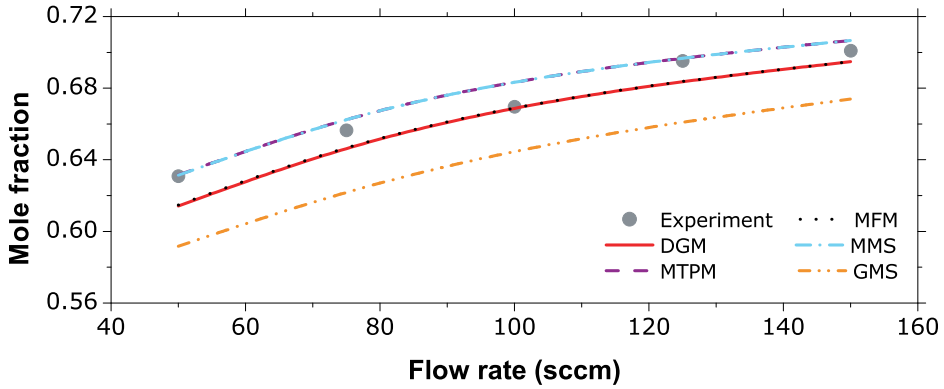

Figure 5.26: Comparison of experimental measurements and various model predictions for Ar at the fuel channel exhaust. Nominal inlet mole fractions at the fuel channel are 20% CH_4, 2.8% H_2, and 77.2% Ar. Inlet mole fractions at the electrolyte channel are 48% H_2O, 1.8% H_2, and 50.2% Ar.

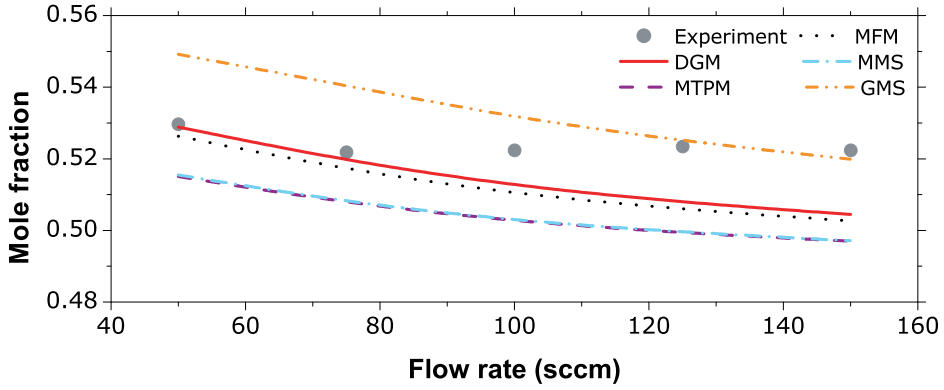

Figure 5.27: Comparison of experimental measurements and various model predictions for Ar at the electrolyte channel exhaust. Nominal inlet mole fractions at the fuel channel are 20% CH_4, 2.8% H_2, and 77.2% Ar. Inlet mole fractions at the electrolyte channel are 48% H_2O, 1.8% H_2, and 50.2% Ar.

At the electrolyte channel exit the mole fractions decrease with increasing flow rate. This is primarily due to the fact that at low flow rate (high residence time) more Ar diffuses across the porous media from fuel channel to the electrolyte channel.

5.4 Summary

This chapter presented the analysis of various porous media transport models and its validation under reaction conditions. The elementary heterogeneous reaction mechanism reported by Hecht et al. has been extended for wider temperature conditions [64]. All model predictions are compared with the experiment reported by Hecht et al. [64]. In general DGM and MFM give almost the same results in all cases. Similarly MTPM and MMS model gives the same results for all cases. For the cases as considered here it is quite obvious that DGM and MFM are able to reproduce the experimental observation to a great extend. MTPM as well

as MMF predictions are also acceptable, though to a lesser extent compared to DGM and MFM. In certain cases GMS predictions are in good agreement with experimental observation. However, in some cases when GMS predicted one of the channel exit mole fractions accurately, it failed to predict the other exit. It should be noticed here that the GMS model does not incorporate Knudsen diffusion. While all other diffusion models considered here incorporates Knudsen diffusion. DGM and MTPM are basically extension of MMS. MMS considered here does not incorporate viscous transport. While other models such as DGM, MTPM, and MFM incorporates viscous transport. The standard deviation σ is calculated

Table 5.2: Error analysis for various model predictions

	Standard deviation σ	
Model	Steam reforming	Dry reforming
MFM	1.3792×10^{-2}	8.0908×10^{-3}
DGM	1.3977×10^{-2}	8.2169×10^{-3}
GMS	1.9453×10^{-2}	1.3967×10^{-2}
MMS	2.0512×10^{-2}	1.4269×10^{-2}
MTPM	2.0556×10^{-2}	1.4311×10^{-2}

according to Eq. 5.1 for the fuel exhaust and the electrolyte exhaust channel separately, and the arithmetic average is presented in Table 5.2

$$\sigma = \sqrt{\frac{1}{\mathrm{N}} \sum_{i=1}^{\mathrm{N}} (X_k - \bar{X})^2}. \tag{5.1}$$

Here $\bar{X}$ are the experimentally measured mole fractions and X_k are the model predicted mole fractions for the fuel and electrolyte channels. From Table 5.2 it is quite evident that MFM deviates least from the measured values, closely followed by DGM. Though GMS model leads to lower values of standard deviation compared to MMS and MTPM, in many cases when it predicted one of the exhaust channel measurement, it failed to predict the other one. However, while doing a standard deviation analysis as done here, the error in predicting one channel is subsided by the accurate prediction of other, leading to better average value. Although MMS and MTPM results in higher standard deviation compared to GMS, for these models the error in predicting the exhaust measurements are even on both channels. And therefore, these models are better alternative compared to GMS model.

Chapter 6

Modeling Button Cells

6.1 Introduction

Button cells are the simplest SOFC set up, that one can use to study the anodic and cathodic processes under various operating temperatures and inlet fuel conditions. There is a large body of experimental data on these systems running on H_2 fuel [114, 115, 15]. These cells can be easily studied using simple polarization models such as the one described by Chan et al. [76], or Williford et al. [78]. However, there are also studies available on methane fuel [18, 17, 39, 38] and higher HCs [40]. Modeling such systems requires more sophisticated models which account for the reaction and diffusion within the porous media.

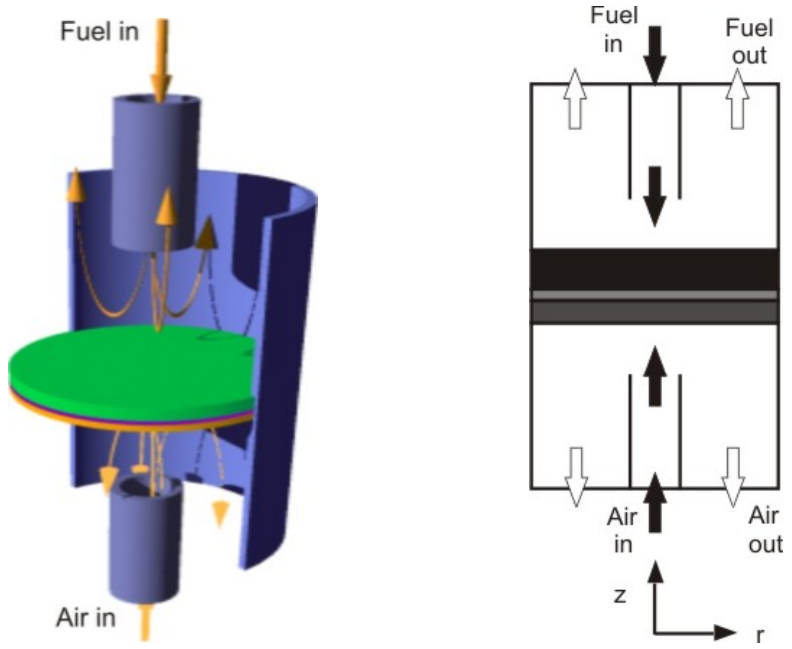

(a) (b)

Figure 6.1: (a) Three dimensional schematic representation of button cell configuration, (b) two dimensional plane of button cell configuration used in the simulation.

Any numerical investigation of cell performance and analysis should make sure the use of physically realistic model parameters. The electrochemical model parameters which quantify the electrochemical performance are significantly important in fuel cell modeling. Furthermore, in most cases the porous media properties such as porosity, pore diameter, particle diameter, and tortuosity are not directly known. However, they are accessible via experimental methods. It is quite well known that the use of very high tortuosity can lead to concentration overpotentials at high current densities, however, at low current densities SOFC models are not sensitive to tortuosity factor [84]. Most often a physically realistic range for tortuosity is 2-6. Though it is quite possible to reproduce the observed current voltage curve by varying many parameters to which the SOFC model is sensitive to, any reliable prediction should make sure that the model parameters are physically realistic.

This chapter presents the simulation of a button cell data reported by Liu et al. [38]. The model parameters derived here are further used in the performance analysis presented in the later chapters. A schematic representation of button cell is given in Fig. 6.1. The configuration is basically a concentric cylindrical assembly intercepted by the membrane electrode assembly (MEA). The fuel and air inlet are through the inner cylindrical pipe, which reaches above the anode and cathode. The product gas outlet is through the concentric space between the inner and outer cylinder.

For the simulations, the governing equations described in section 4.4 are solved using the commercial CFD code FLUENT. The computational procedure is described in the following section.

6.2 Computational procedure

The elliptic transport equations are solved using the commercial CFD code FLUENT [1]. However, the source terms and fluxes appearing in Eq. 4.35 and the electrochemistry model (Eqs. 3.7, 3.14, and 3.25) are implemented using User Defined Functions (UDF) [2]. The species fluxes are calculated using DGM. Though the DGM equation contains contribution due to diffusive flux as well as viscous flux (Darcy flow), the viscous term appearing in Eq. 4.21 is neglected here. In fact there is little error due to this omission since the solution of momentum equation in the porous media also takes into account of the Darcy flow (Eq. 4.34). During the iterations the thermodynamic state variables and the species concentrations are accessed from the solver, which are in turn used to evaluate the UDF returned values. Velocity (0.04 m/s) inlet boundary conditions and pressure outlet boundary conditions are used for the calculations. Eqs. 3.7, 3.14, and 3.25 form a system of algebraic equations with i, η_a and η_c as unknowns. At three-phase boundary for each computational cell the residual form for the above variables can be written as

$$F(\xi) = 0, \tag{6.1}$$

where the vector ξ is ordered as

$$\xi = [i, \eta_a, \eta_c]^T. \tag{6.2}$$

This equation system is solved using damped Newton iterations. The Newton solver normally converges within 3 to 4 iterations. However, calculation of residual requires the evaluation of Nernst potential and the exchange current densities which are dependent on the partial pressures of H_2, H_2O, and O_2 at the three-phase boundary.

6.3 Model predictions

Numerous calculations have been carried out to reproduce the experimental data reported by Liu et al. [38]. Since the experimental report does not give a detailed description of the flow configuration, the simulation study assumes the inlet fuel pipe to be 7 mm in diameter and ends 5 mm above the anode. The anode is a 20 mm in diameter and 0.5 mm thick porous membrane. The parameters used for the calculation are given in Tables 6.1 and 6.2.

6.3.1 Interpreting experimental results

A comparison of experimentally observed and simulated polarization curves is shown in Fig. 6.2, for the fuel composition of 97% vol. CH_4 and 3% vol. H_2O.

Table 6.1: SOFC parameters

Parameters	Values	Units
Anode		
Thickness (l_a)	0.50	mm
Average pore radius (r_p)	0.50	μm
Average particle diameter (d_p)	2.50	μm
Specific area (A_s)	1025	cm^{-1}
Porosity (ϵ)	0.35	
Tortuosity (τ)	3.80	
Charge transfer coefficient (β_a)	0.50	
Electrolyte		
Thickness (l_e)	25.0	μm
Cathode		
Thickness (l_c)	30.0	μm
Average pore radius (r_p)	0.50	μm
Average particle diameter (d_p)	2.50	μm
Porosity (ϵ)	0.35	
Tortuosity (τ)	3.80	
Charge transfer coefficient (β_a)	0.5	

In all cases the model reasonably well reproduces the experimental observations for high current density region. For all operating temperatures we observe a significant drop in cell potential at low current densities, indicating the dominance of activation losses, which is

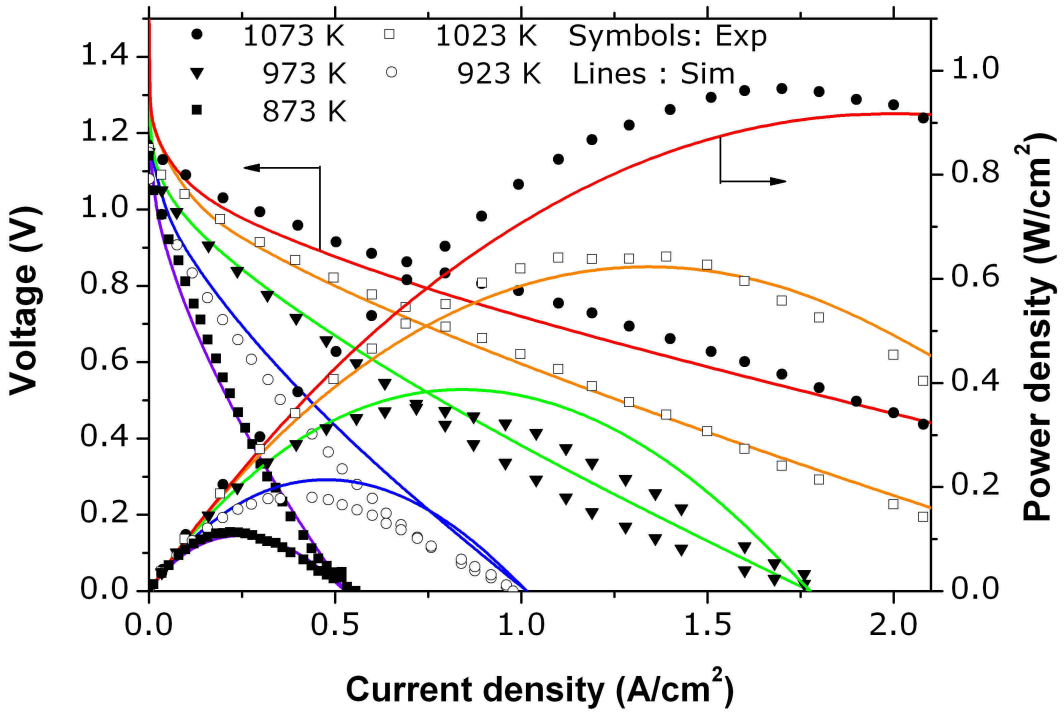

Figure 6.2: Voltage and power density against current density. Comparison with experimental data [38].

Table 6.2: Parameters for exchange current density

Parameters	Value	Units
H_2 oxidation ($i^*_{H_2}$)		
k_{H_2}	2.07×10^5	A cm^{-2}
E_{H_2}	87.8	kJ mol^{-1}
O_2 reduction ($i^*_{O_2}$)		
k_{O_2}	5.19×10^4	A cm^{-2}
E_{O_2}	88.6	kJ mol^{-1}

not really observed in the experimental data. However, the major discrepancy between the model predicted results and the experimentally observed data lies in the open circuit voltages (OCV). The experiment reports maximum OCV of 1.17 at 800°C. However, the model predicts a much higher OCV (1.55 V) at 800°C. To cross-check the model predictions, OCVs are calculated based on equilibrium calculations (with and without surface carbon). In performing these calculations, equilibrium composition resulting from 97% CH_4 and 3% H_2O is first calculated and then the OCVs are calculated using Nernst equation assuming H_2 oxidation mechanism. Experimentally observed OCVs are compared with those predicted by the model and equilibrium calculations (Fig. 6.3).

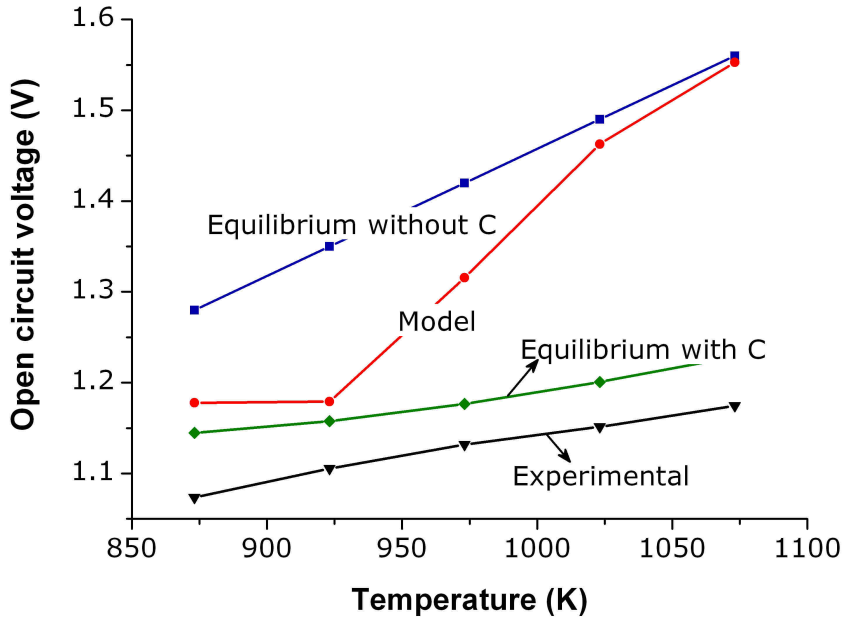

Figure 6.3: A comparison of experimentally observed OCVs and those predicted by the model and equilibrium calculations with and with out surface carbon formation.

In general, though slightly higher, equilibrium composition with surface carbon yields OCVs which are in reasonable agreement with experimental observation. The experimental observation of OCV is lower presumably due to slight gas leakage. However, equilibrium composition without accounting surface carbon resulted in much higher OCV's. At higher temperatures model predictions are close to those of equilibrium predictions without surface carbon, while at low temperatures model predictions are close to equilibrium calculations with surface carbon. This leads to the conclusion that, though the surface chemistry model is capable of predicting surface carbon formation, refinement of the model for carbon formation is required for accurate predictions especially at higher temperatures. Nevertheless, it should be noticed that under short-circuit conditions the model is in good agreement with experiments. It should be remembered that the Nernst equation is strictly valid only under equilibrium conditions, and for the calculation carried out here, we assumed that the H_2 electrochemical oxidation is fast enough to be in equilibrium. Furthermore, it is also worth remembering that the Nernst equation is not valid for the conditions of pure species, such as a cell running on 100% H_2. In such a case the Nernst equation can not be used for the calculation of OCV. For the calculations carried out here, since the partial pressure of H_2O is very low under open circuit conditions due the reforming reactions, the use of Nernst equation for the calculation of OCV leads to a very high voltage. Liu et al. [38] have analyzed a number of possible electrochemical oxidation reactions and concluded that the OCVs for the partial oxidation of C are in good agreement with experimental observation. However, when enough H_2O is present in the feed, the internal reforming can lead to H_2 production

within the anode, and under such conditions H_2 oxidation will be the dominant mechanism of electrochemical charge transfer compared to other pathways.

6.3.2 Overpotentials

Figures. 6.4 and 6.5 show the cathodic (η_c) and anodic (η_a) activation losses versus current density. The cathodic activation losses show expected behavior. The losses increase with de-

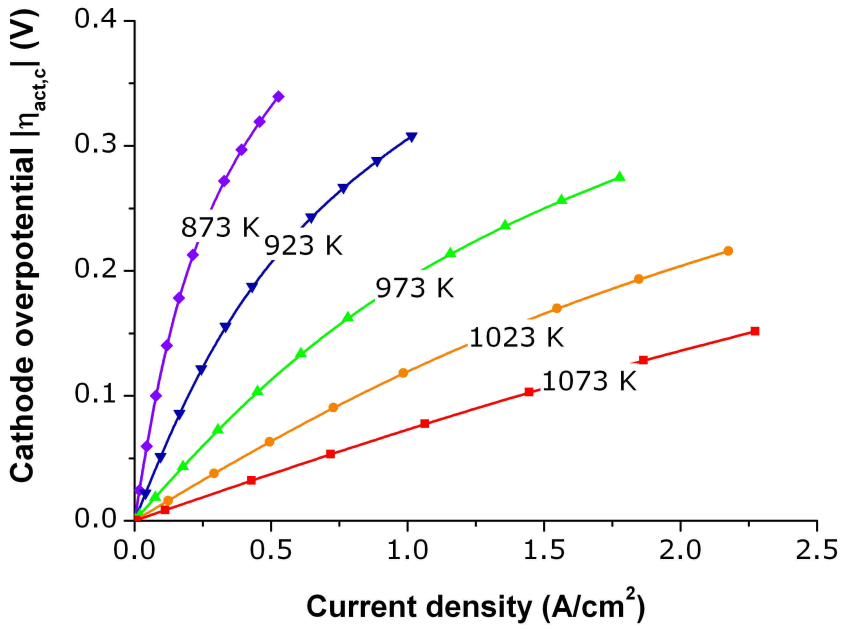

Figure 6.4: Cathode overpotentials as a function of current density for different operating temperatures.

creasing temperature and increasing current density. However, anodic activation loss shows a marked difference from the expected behavior. The anodic losses are distinctly different for high and low temperatures. At high temperatures the losses are high at low current densities. At this point it is worth to analyze the functional dependency of exchange current density i_0. The exchange current density is the current density of charge transfer reaction at equilibrium electric potential difference between the electrode and the electrolyte phases, and is usually a strong function of species concentration and temperature. A high exchange current density causes the electrochemical charge transfer reaction to proceed rapidly upon varying the potential difference from its equilibrium value. A careful analysis of Eq. 3.8 reveals that a zero H_2O partial pressure leads to zero exchange current density. At low current densities, nearly all H_2O produced at the three-phase boundary (TPB) by electrochemical charge transfer reaction is consumed by the reforming chemistry, leading to very low exchange current density for H_2 oxidation. This basically requires high aviation overpotential to drive the electrochemical charge transfer reactions. It should be noticed that the activation overpotential

η_a is the potential difference above the equilibrium electric potential difference between the electrode and electrolyte phases ($\eta_a = E_a - E_a^{eq}$).

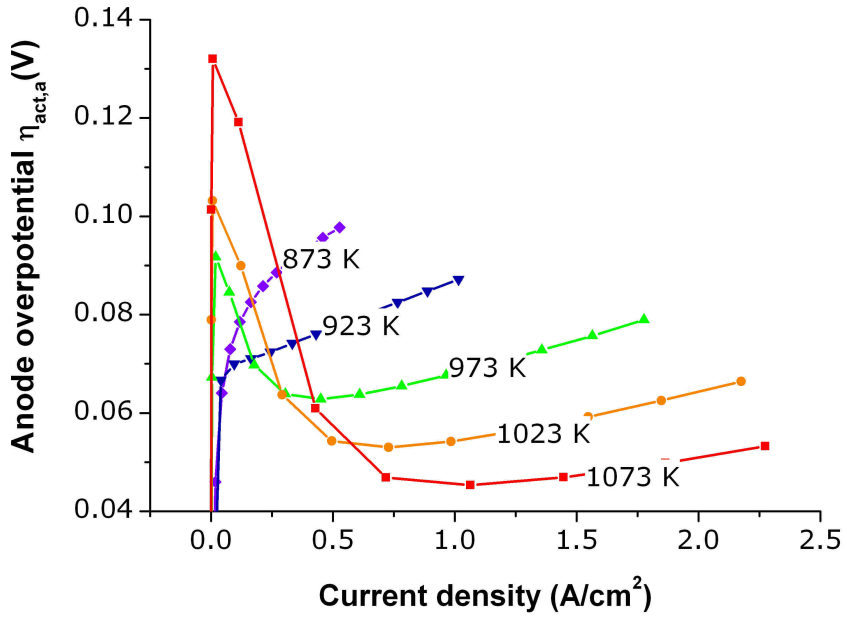

Figure 6.5: Anode overpotentials as a function of current density for different operating temperatures.

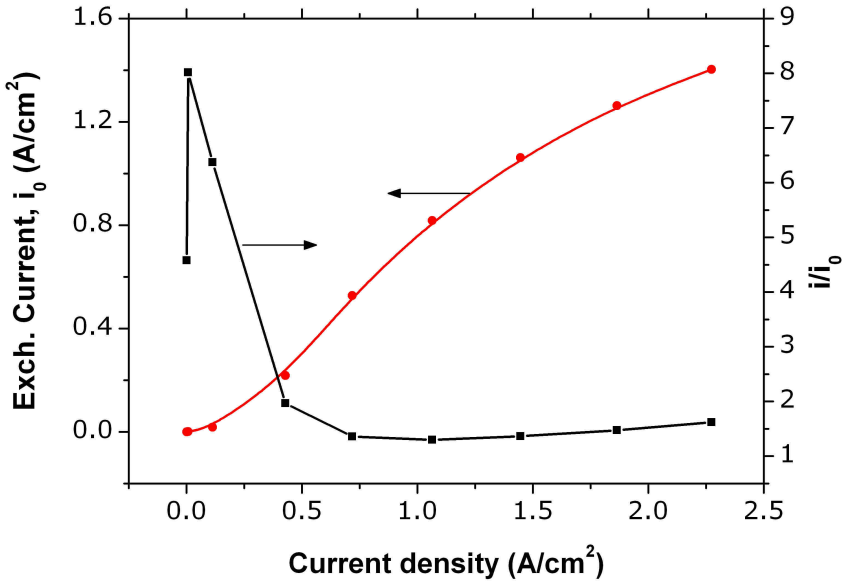

Figure 6.6: Exchange current density i_0 and i/i_0 for the anodic branch as a function of current density for the operating temperature of 1073 K.

However, the trend is different at low temperatures, where there is still enough H_2O at the TPB due to the low rate of reforming and hence leading to the expected behavior in loss potential. At high temperatures and high current densities there is plenty of H_2O available at the TPB and hence the anodic losses show the expected behavior at high current densities. Though one can argue this behavior is a limiting case of the exchange current density function (Eq. 3.8), it is worth remembering that any physically realistic functional formulation of exchange current density should be dependent on the concentration of the reactants and products participating in the charge transfer chemistry [75]. Since H_2 is undoubtedly an electrochemically active species any formulation of exchange current density will be dependent on H_2O partial pressure and will lead to same behavior at low current densities for any fuel with very low H_2O content. A plot of exchange current density i_0 and i/i_0 for the

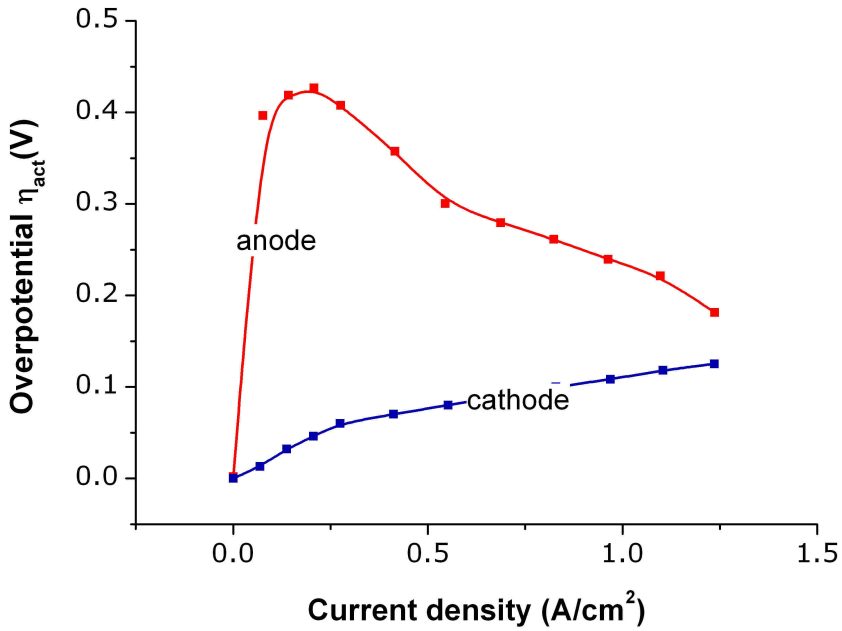

Figure 6.7: Anodic and cathodic overpotentials as a function of current density; experimental observation. Conditions:1000°C 9.2%CH_4 in Ar [116].

anodic branch is shown in Fig. 6.6. It is quite clear that the anodic overpotential follows the trend of i/i_0. Though not for the same cell configuration and fuel composition, Ihara et al. [116] experimentally investigated the anodic overpotential for 9.2% Vol. CH_4 in Ar at 1000°C. The observed anodic and cathodic overpotentials are shown in Fig. 6.7. Although the fuel contains only 9.2% Vol. CH_4 it should be noticed that, CH_4 enters the cell under dry conditions. The experimentally observed anodic overpotential shows striking similarity to the trend reported here.

6.3.3 Surface coverages

Figure 6.8 shows the carbon deposition at OCVs for various operating temperatures. Carbon deposition is maximum for the highest operating temperature of 800°C. Figure 6.9 shows carbon formation as a function of current density.

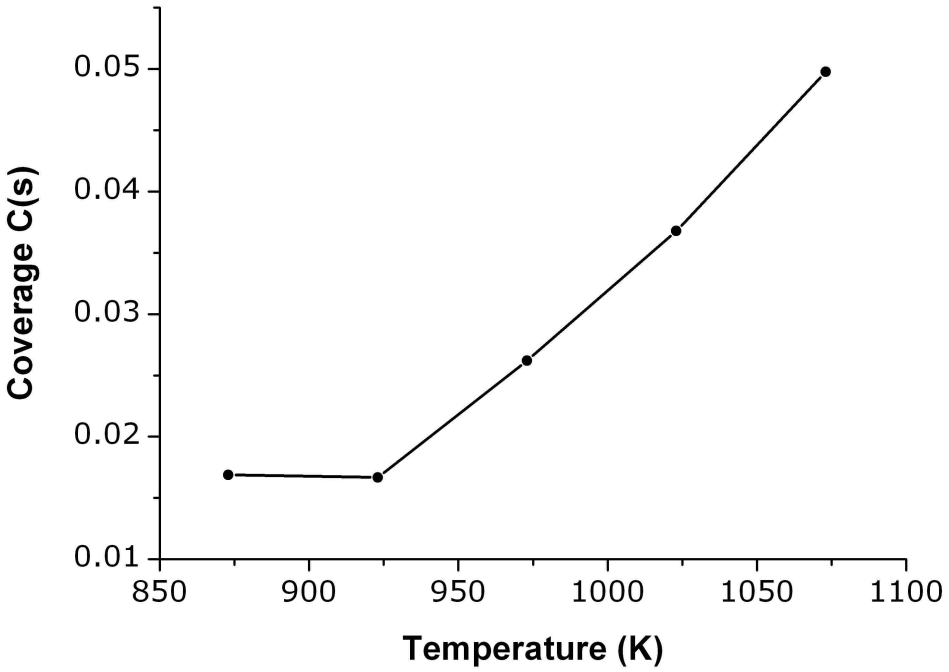

Figure 6.8: Surface coverage of carbon at OCVs fore different operating temperatures.

It is evident from the figure that the flow of current mitigates coking. It is mainly because of the fact that, as current starts flowing, more and more H_2O is formed at the three-phase boundary and hence reducing the possibility of CH_4 cracking on Ni surfaces. This observation of high C deposition at OCV is in good agreement with the experimental report [38]. Surface coverages of other species at the three-phase boundary are shown in Figs. 6.10, 6.11 and 6.12. Figure 6.10 shows the surface coverage of CO and free Ni sites. It can be seen that at open circuit the Ni surface is relatively open.

As current starts to flow, the free Ni surfaces are mostly covered by CO and hydrogen (Fig. 6.11). However, the coverage of hydrogen is relatively less compared to CO. The surface coverage of hydrogen results from the dissociative adsorption of H_2O and CH_4. For all temperature regimes major species on the surface are found to be hydrogen and CO. However, hydrogen coverage is ~45% of CO coverage for all cases. Figure 6.12 shows surface coverages of oxygen. It should be noticed that oxygen on the surface results from the dissociative adsorption of water.

All the species coverages decrease with increasing temperature. It is obvious because desorption rates are higher at higher temperature thereby leaving the Ni surfaces open at

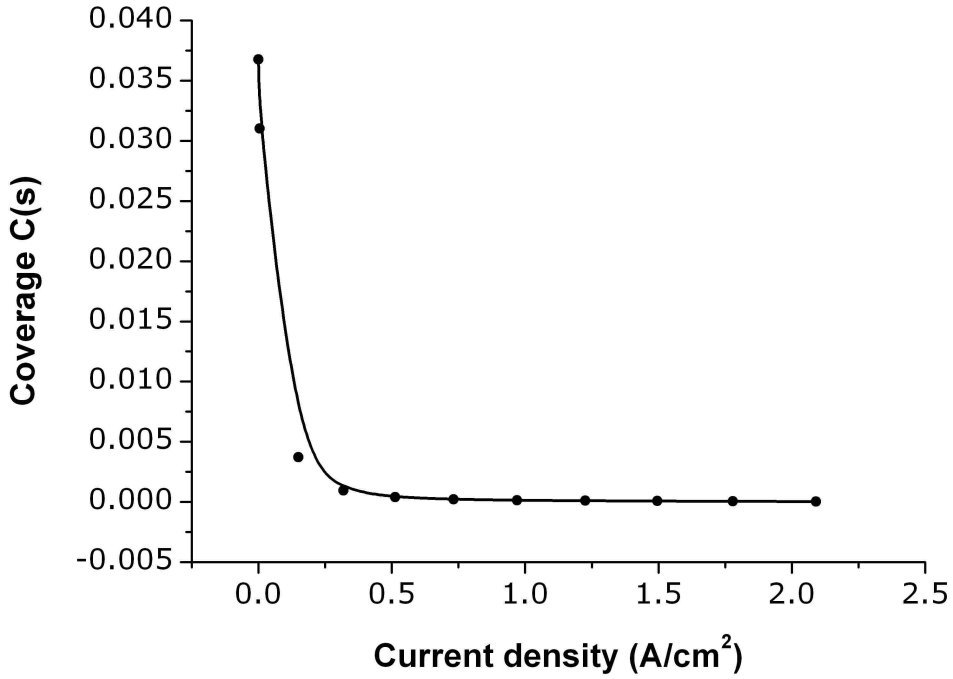

Figure 6.9: Carbon formation as a function of current density for the operating temperature of 1023 K.

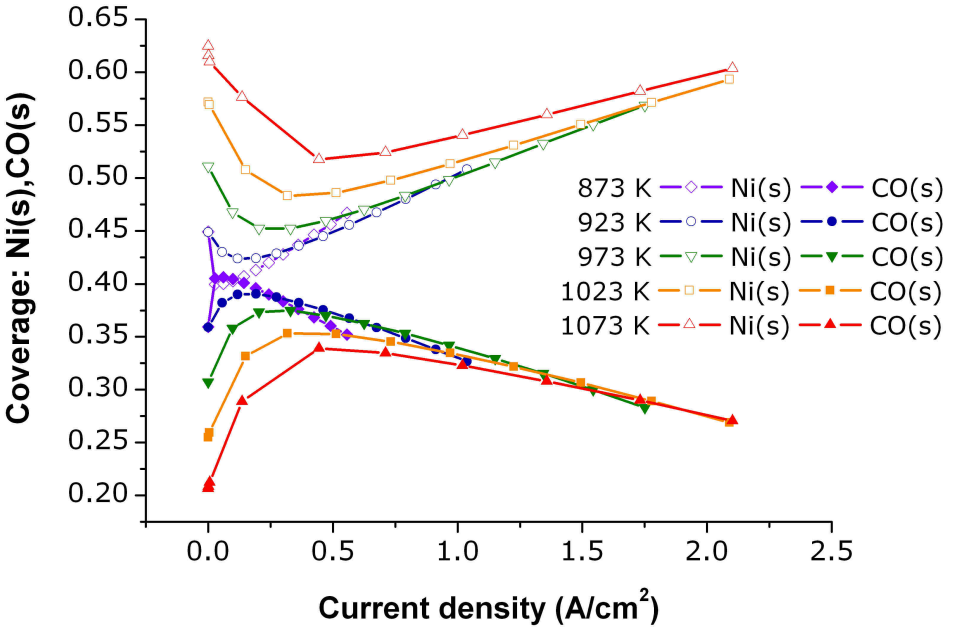

Figure 6.10: Fraction of Ni vacancies and surface coverage CO at the three-phase boundary as a function of current density for different operating temperatures.

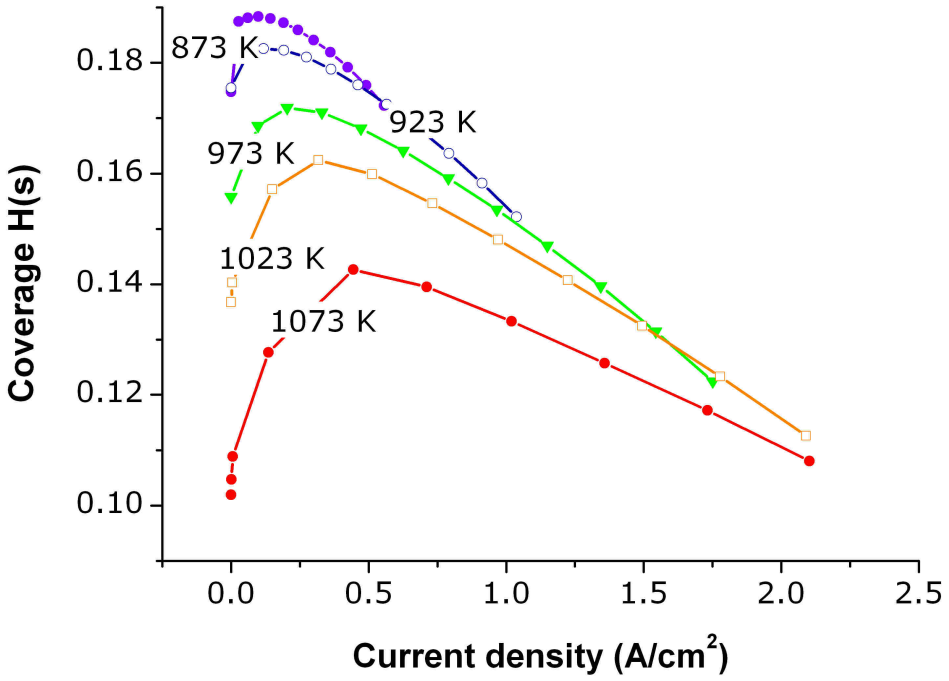

Figure 6.11: Surface coverage of hydrogen at the three-phase boundary as a function of current density for different operating temperatures.

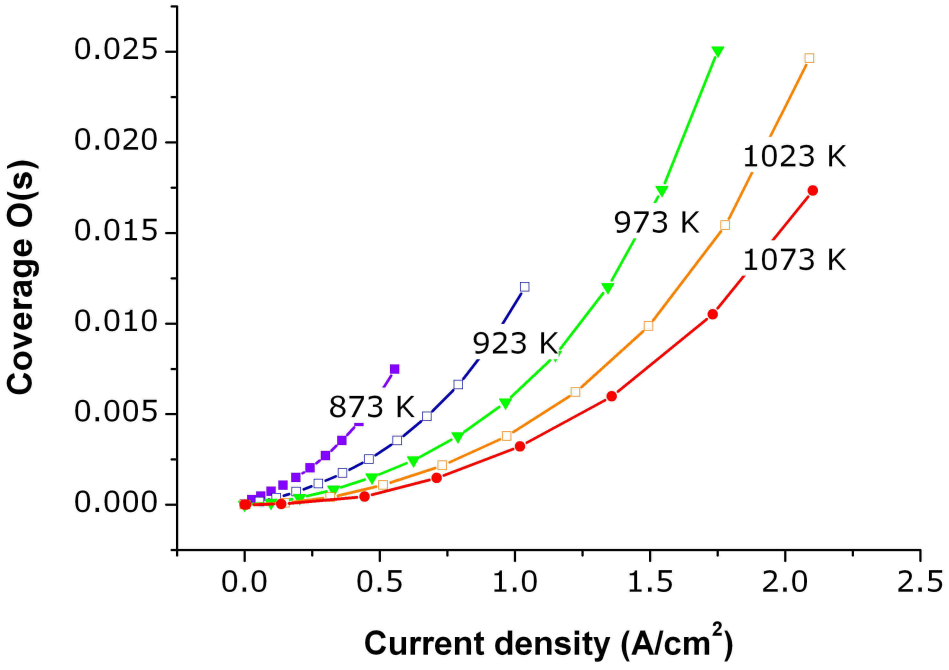

Figure 6.12: Surface coverage of oxygen at the three-phase boundary as a function of current density for different operating temperatures.

high temperature. We believe that carbon formation and its subsequent reaction with H_2O (globally stated as $C+H_2O \Leftrightarrow CO + H_2$) plays a key role at low current densities, where CO and H surface coverages keep increasing. For instance in the case of 750°C a comparison of surface coverages of H (Fig. 6.11), CO (Fig. 6.10), and C reveals that coking is suppressed at current density of approximately 0.3A/cm^2 (Fig. 6.9), and we see a transition in the trend of H_2 and CO coverages at the same current density.

6.3.4 Dependence of water

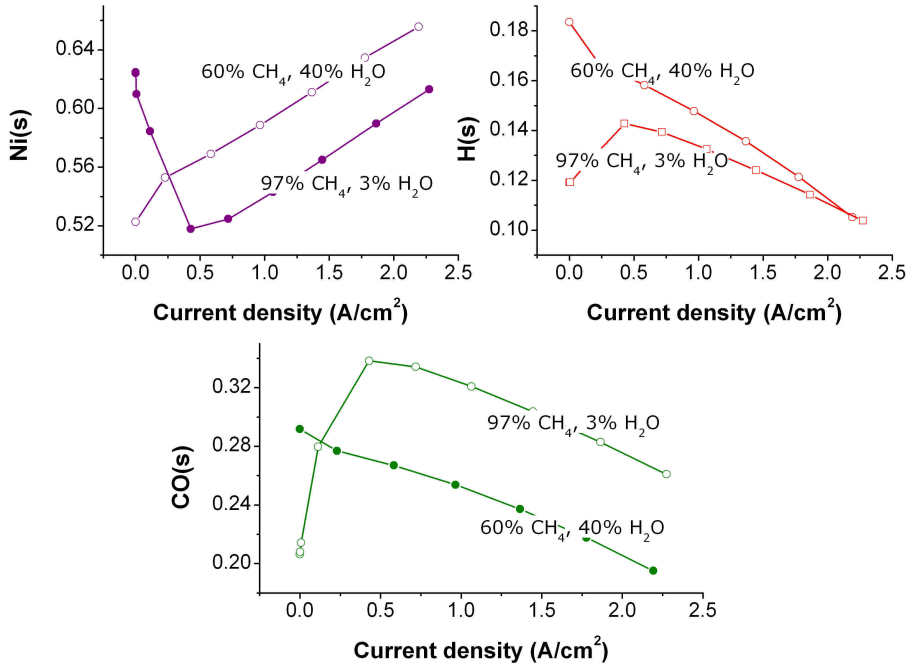

Figure 6.13: Comparison of surface coverages of various surface adsorbed species for two different fuel compositions with varying H_2O content.

Simulation are carried out with highly humidified CH_4 (40% vol H_2O) to understand the role of H_2O. A comparison of surface coverages of H and CO, and free Ni surface is shown in Fig. 6.13. Fuel gas with 40% H_2O resulted in higher H coverage and lower CO coverage compared to fuel gas with 3 vol. %H_2O. Fig. 6.14 shows a comparison of activation losses for anode and cathode for the two different feed gas compositions. For the case of fuel gas with 40% vol. H_2O activation overpotentials show a linear behavior with increasing current density and result in a much low activation losses compared to fuel gas with 3% vol. H_2O.

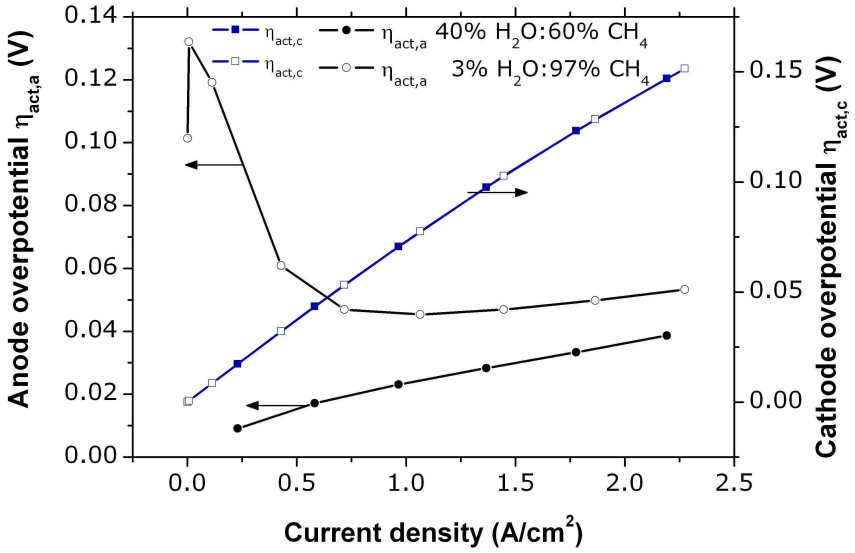

Figure 6.14: Comparison of overpotentials for two different inlet fuel compositions with varying H_2O content.

6.3.5 Species profiles

In their recent work Lin et al. [39] reported the exit fuel compositions from a button cell working under the same fuel compositions as in [38]. They found all the products to be increasing with increasing current density, though the equilibrium calculation predicts different trend. However, data are reported only for lower current densities (up to 0.8 A/cm^2). The

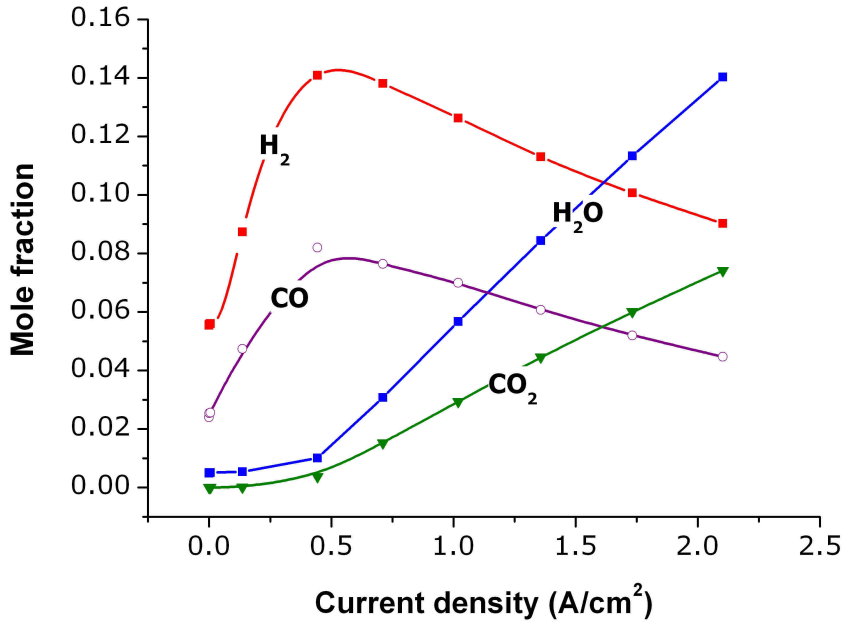

Figure 6.15: Exit gas composition as a function of current density at 800°C for the case of 97%CH_4 and 3%H_2O.

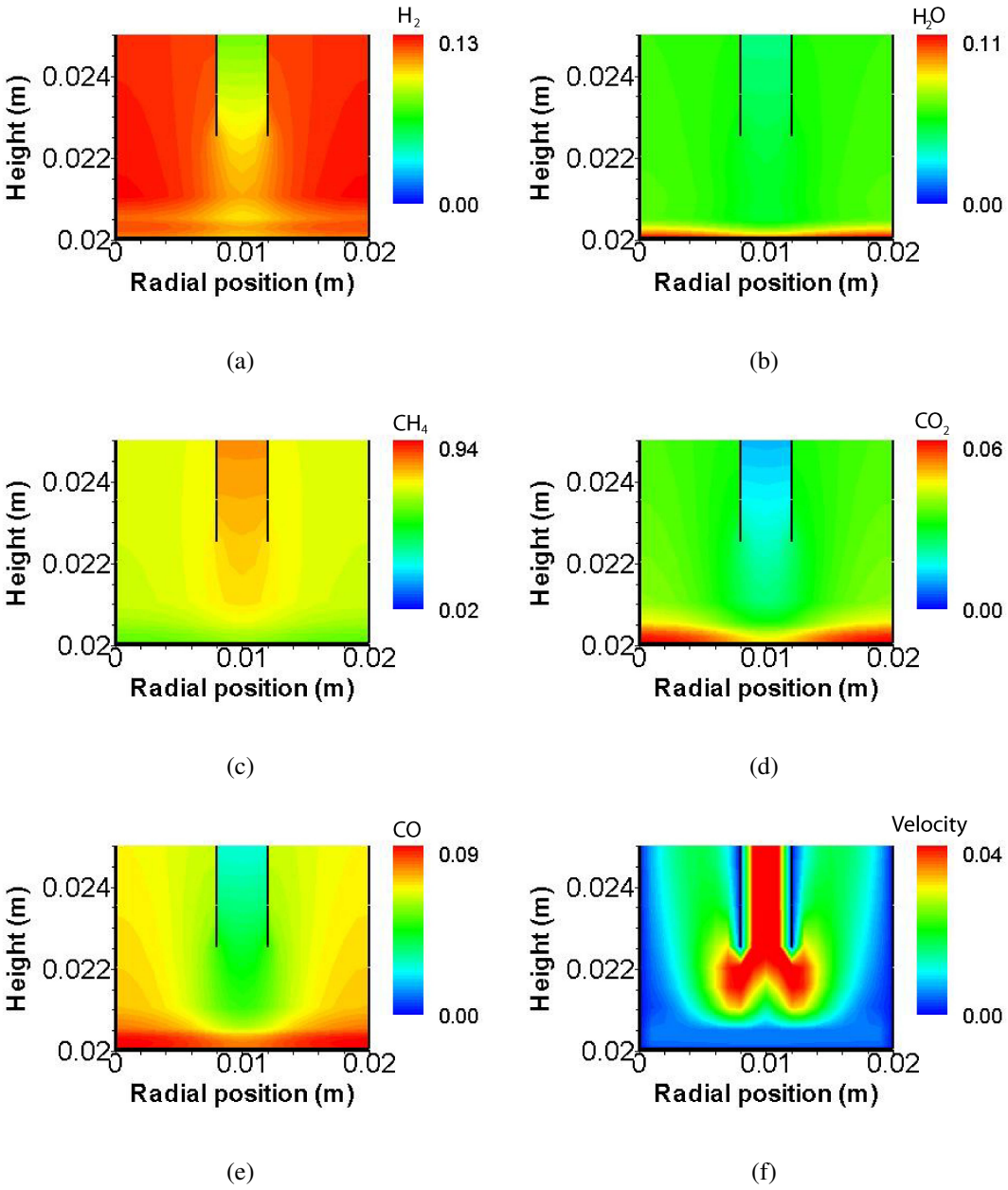

Figure 6.16: (a) H_2 mole fractions within the anode compartment. (b) H_2O mole fractions within the anode compartment. (c) CH_4 mole fractions within the anode compartment. (d) CO_2 mole fractions within the anode compartment. (e) CO mole fractions within the anode compartment. (f) Velocity (m/s) profiles with in the anode compartment.

findings presented in this work also predict an increasing product composition at low current densities (up to 0.5 A/cm^2) and then a decreasing H_2 and CO concentrations for further increase in current densities (Fig. 6.15). However, the results presented here shows more H_2O than CO_2, while the experiment predicts higher CO_2 than H_2O. The prediction of higher H_2O than CO_2 is consistent with the equilibrium predictions.

Contour plots of all reactants and products are shown in Fig. 6.16. It is quite clear that H_2 is produced within the anode and H_2O is produced by the electrochemical charge transfer reaction at the three-phase boundary. It can also be seen that the very low flow rate causes the

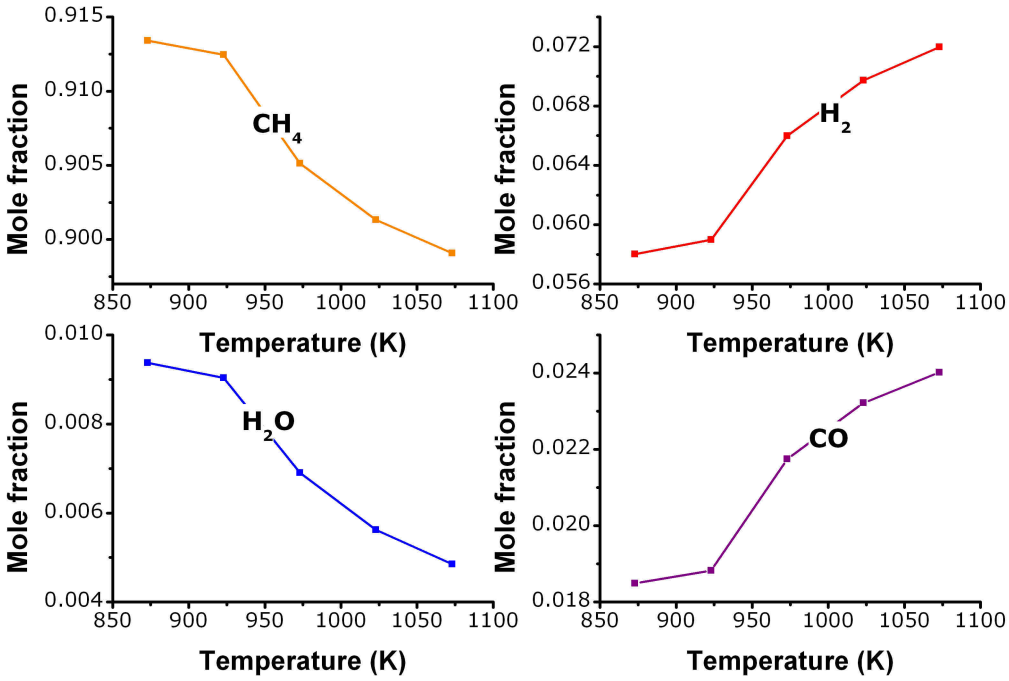

Figure 6.17: Composition of anode stream at OCVs as a function of temperature.

back diffusion of H_2 produced within the anode into the fuel inlet channel. Back diffusion can also be observed in the case of CO. It should be noticed that in a configuration like this, under low flow rates, the profiles will depend strongly on the distance between the anode surface and the fuel inlet. For the case of 800°C, velocity profile within the anode compartment is shown in Fig. 6.16(f).

The composition of anode exhaust stream at OCV for various operating temperatures is shown in Fig. 6.17. Increasing temperature increases the concentration of all reaction products. CO_2 is omitted from the figure due to its very low concentration at OCVs.

6.4 Summary

In this chapter a detailed CFD study of the chemical and electrochemical processes in an internally reforming anode supported SOFC button cell was carried out. Detailed models for chemistry, electrochemistry and porous media transport have been implemented into the commercial CFD code FLUENT with the help of used defined functions (UDF). Simulation results were compared with experimentally reported data. The comparisons lead to the conclusion that precise calculation of surface carbon formation is critical for the accurate prediction of OCVs for hydrocarbon fuels with very low H_2O content, and that Nernst equation may not be valid for the calculation of OCV for a fuel composition such as the one considered here. Anodic overpotentials showed remarkable difference from expected behavior.

Ihara et al. [116] have carried out experiments to evaluate the anodic and cathodic overpotential for dry CH_4 fuel (9.2% CH_4 in Ar), which is quite different from the CH_4 rich fuel (97%CH_4) used by Liu et al. [38]. Nevertheless, the predicted activation overpotential agrees qualitatively with the findings of Ihara et al. The model presented here is well applicable for any fuel cell configuration and can be applied to understand the underlying chemical and physical processes and hence to choose the best operating conditions for SOFCs.

Chapter 7

Planar cell modeling

7.1 Introduction

Resolving the details of processes such as heat transfer, mass transfer, thermo-catalytic chemistry and electrochemistry in each unit cell of a fuel cell stack is an inherently complex task and extremely computational intensive. In most cases the temperature distribution significantly influences the performance of the cell. A reasonable approach towards exploration of detailed processes within the cell stack is considering a single channel with appropriate boundary conditions. However, the temperature boundary condition that one can impose strongly depends on the unit cell's position within the stack and the surrounding cells' temperature. It is quite rational to assume isothermal conditions for a cell located in the center of the stack. However, this assumption may not be a reasonable one for outermost cells in the stack. Therefore, to adequately understand the macroscopic processes it is necessary to visit both isothermal and adiabatic operational regimes.

In this chapter the equations described in section 4.5 are solved to analyze the local distribution of variables such as temperature, species concentration, current density, reversible potential etc. Furthermore, the performance of the cell for various operational and geometrical conditions is explored. A schematic representation of the cell geometry considered in this chapter is depicted in Fig. 7.1.

7.2 Computational procedure

In order to solve the equation systems described in section 4.5, they are first cast into a finite volume form. The channels, interconnects and electrolyte are treated as one dimensional. In the axial direction the reactor geometry is discretised into 200 cells. The anode is discretised into 25 cells along the thickness and the cathode into 10 cells. Eqs. 4.37, 4.38, 4.41, 4.42, 4.46, 4.47, 4.48, 4.53, 4.54 and 2.9, form a system of coupled non-linear equations, which

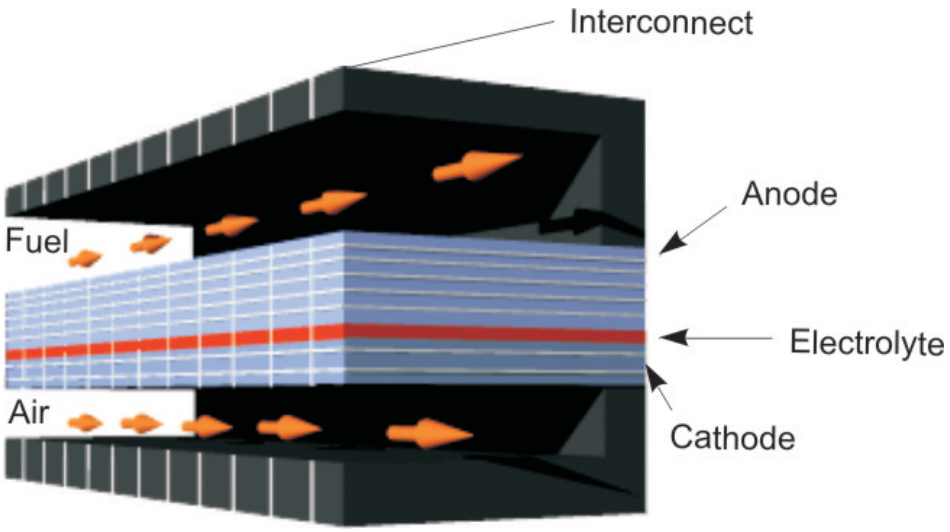

Figure 7.1: Schematic representation of planar cell.

can be written in the residual form as

$$F(\psi) = 0, \tag{7.1}$$

where the vector ψ is given by

$$\begin{aligned}\psi = [&(T)_{\mathrm{ic}}, (Y,u,T)_{\mathrm{a}}, (Y,\rho,T,\theta)_{\mathrm{a,1}} \ldots (Y,\rho,T,\theta)_{\mathrm{a,n}},\\ &(T)_{\mathrm{e}}, (Y,\rho,T)_{\mathrm{c,1}}, \ldots (Y,\rho,T)_{\mathrm{c,m}}, (Y,u,T)_{\mathrm{c}}, (T)_{\mathrm{ic}}]^{\mathrm{T}}.\end{aligned} \tag{7.2}$$

In Eq. 7.2 the indices ic, a, a,1, a,n, e, c,1, c,m, c, respectively, represents the interconnect, anode channel, first discretized cell in the anode, n'th discretized cell in the anode, electrolyte, first discretized cell in the cathode, m'th discretized cell in the cathode, and cathode channel. The entire solution procedure follows a space marching algorithm: at each axial position the transient system of equations are solved until a steady state solution is obtained. The initial condition at each axial position assumes the converged solution from the previous finite volume cell. Due to the elliptic nature of the heat balance equation in porous electrodes and the conductive terms in the solid regions an outer iteration loop is formed around the marching algorithm. The equation system is solved using the differential algebraic equation (DAE) solver LIMEX [117]. The entire solution converges in few passes.

The solution of the porous media problem also requires the current density at the three-phase boundary. The current density is calculated from the system of algebraic electrochemical model equations 3.7, 3.14, and 3.25. The unknowns can be written in the vector form as

$$\xi = [i, \eta_{\mathrm{a}}, \eta_{\mathrm{c}}]^{\mathrm{T}} \tag{7.3}$$

This equation system is solved using a damped Newton iteration, which converges in three to four iterations. The software is written in FORTRAN 77 and integrated into the Detailed Chemistry software package DETCHEM [2].

Table 7.1: Parameters for simulations

Parameters	Values	Units
Anode		
Thickness (l_a)	0.75	mm
Average pore radius (r_p)	0.50	µm
Average particle diameter (d_p)	2.50	µm
Specific area (A_s)	1025.00	cm^{-1}
Porosity (ϵ)	0.35	
Tortuosity (τ)	3.80	
Charge transfer coefficient (β_a)	0.50	
Specific heat (C_{pa})	450.00	J Kg^{-1} K^{-1}
Density (ρ)	3310.0	Kg m^{-3}
Thermal conductivity (k)	1.86	J m^{-1} s^{-1} K^{-1}
Electrolyte		
Thickness (l_e)	25.00	µm
Specific heat (C_{pe})	470.00	J Kg^{-1} K^{-1}
Density (ρ)	5160.00	Kg m^{-3}
Thermal conductivity (k)	2.16	J m^{-1} s^{-1} K^{-1}
Cathode		
Thickness (l_c)	30.00	µm
Average pore radius (r_p)	0.50	µm
Average particle diameter (d_p)	2.50	µm
Porosity (ϵ)	0.35	
Tortuosity (τ)	3.80	
Charge transfer coefficient (β_a)	0.50	
Specific heat (C_p)	430.00	J Kg^{-1} K^{-1}
Density (ρ)	3030.00	Kg m^{-3}
Thermal conductivity (k)	5.84	J m^{-1} s^{-1} K^{-1}
Interconnect		
Thickness l_i	300.00	µm
Specific heat (C_{pI})	550.00	J Kg^{-1} K^{-1}
Density (ρ)	3030.00	Kg m^{-3}
Thermal conductivity (k)	20.00	J m^{-1} s^{-1} K^{-1}

The reliability of the planar cell predictions relays on the accuracy of the model parameters. For example, the exchange current density parameters depend on the micro-structural properties such as porosity, pore and particle diameter etc. These parameters strongly influence the three-phase boundary length. For that reason the exchange current density parameters deduced by simulating one set of experimental data may not be valid for a cell with different micro-structural properties. Here, all the electrochemical model parameters and the micro-structural properties required for the planar cell modeling are the same as the ones presented in Chapter 6 for button cell modeling. The planar cell model predictions are reliable

as long as the cell is made up of the same constituents that make up the button cell. However, solving the heat transfer problem requires knowledge about the heat transfer properties of various structural components. The complete data set used for the simulation purpose are given in Table 7.1.

7.3 Local properties

7.3.1 Electrochemical properties

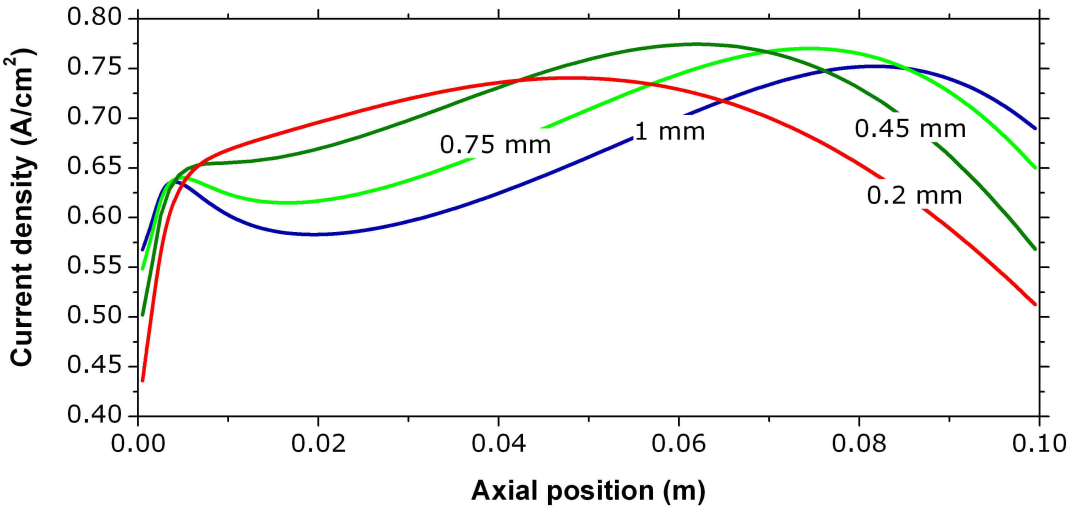

Figure 7.2: Current density for different anode thicknesses for cell operating at 0.7 V. The inlet fuel consists of 40%CH_4 and 60%H_2O at 800°C. Air enters the cathode side at 650°C and the air number λ=1 (Eq.7.11)

For the results presented here, a 10 cm long cell is considered and the inlet fuel is assumed to consist of 40% vol. CH_4 and 60% H_2O. The fuel enters the cell at 800°C with a velocity of 0.3 m/s. Air is assumed to enter the cell at 650°C with a velocity of 3 m/s. Figure 7.2 shows the influence of anode thickness on current density. It is quite evident from the graphs that the shape of the curve changes as the thickness changes. In general two regions with decreasing current density are observed; near the inlet and the exit of the channel. The decrease in current density near the inlet is due to the decreasing temperature because of endothermic reforming within the cell and decrease near the exit is due to the fuel dilution and oxidant depletion effect. However, decrease in current density near the fuel inlet is not observed for thin anodes; mainly due to low extend of reforming. For comparing isothermal and non-isothermal cases, the current density and reversible potential for both cases are shown in Fig. 7.3. In both cases inlet fuel comprises of 40% CH_4 and 60% H_2O. The reversible potential follows the same trend in both cases. For isothermal operating conditions the current density

linearly decreases after the initial peak, merely due to fuel dilution. Under non-isothermal operating conditions however, the current density is dominantly affected by the temperature, leading to an increases towards the channel exit. It should be noticed that if one increases the channel length further, the fuel dilution effect will eventually bring down the current density as is observed in Fig. 7.2 for thicker anode.

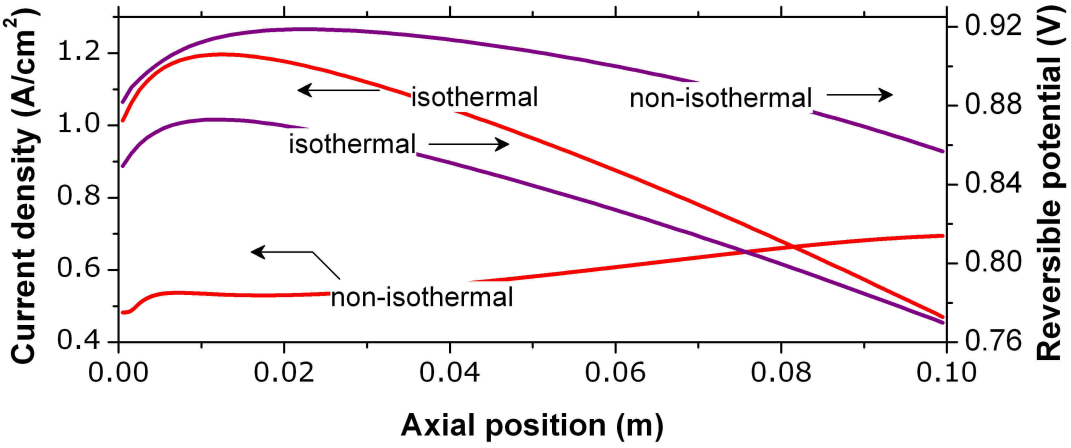

Figure 7.3: Current density and reversible potential for cell operating at 0.7 V. The inlet fuel consists of 40%CH_4 and 60%H_2O at 800°C. Air enters at 650°C and λ=3.5

7.3.2 Temperature profiles

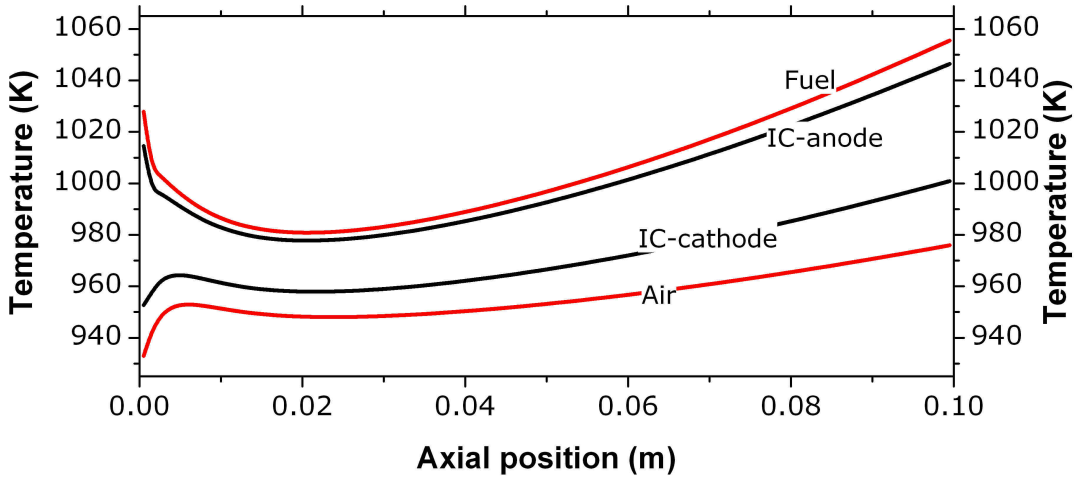

Figure 7.4: Temperature profile within flow channels and interconnect for cell operating at 0.7 V. The inlet fuel consists of 40%CH_4 and 60%H_2O at 800°C. Air stream is assumed to enter the cathode channel at 650°C.

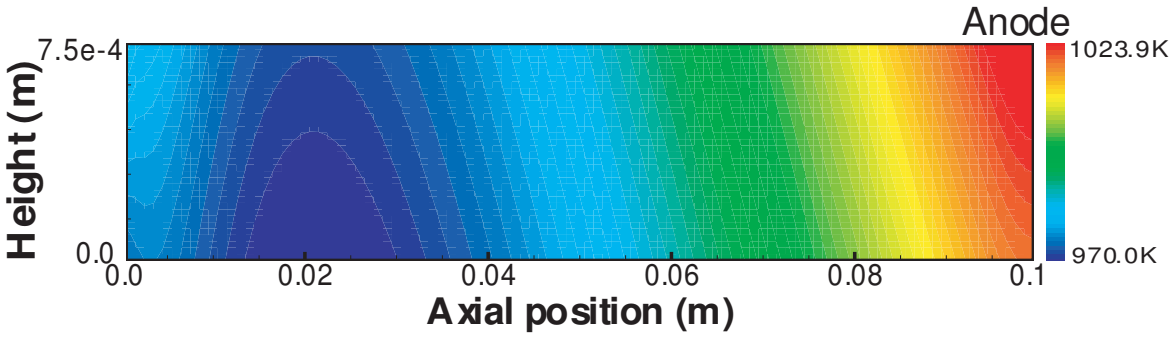

(a)

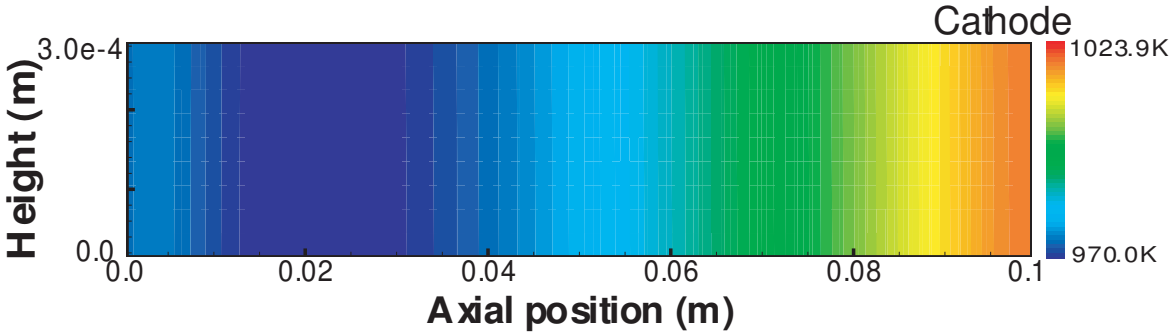

(b)

Figure 7.5: Temperature distribution within the anode and cathode for cell operating at 0.7 V. The inlet fuel consists of 40%CH_4 and 60%H_2O at 800°C. Air stream is assumed to enter the cathode channel at 650°C (a) anode, (b) cathode.

The temperature distribution in the fuel/air channels and the interconnects are shown in Fig. 7.4. Interestingly, the anode side interconnects are at lower temperature than the fuel temperature, nonetheless, the cathode side interconnects are at higher temperature than the air temperature. The higher temperature of cathode side interconnect compared to the air temperature is primarily due to the heat radiation from the cathode electrode to interconnect. Near the inlet the fuel stream virtually looses heat to the relatively cold air entering the cathode, further heat is consumed by the endothermic reforming reactions.

The temperature distribution within the anode and cathode is presented in Figs. 7.5(a) and 7.5(b). The decrease in temperature near the fuel inlet due to reforming also affects fuel utilization. For direct internal reforming longer cells are required to achieve better fuel utilization. It is apparent from Fig. 7.2 that, a 5 cm long cell would result in an increasing local current density near the channel exit, principally due to the increasing cell temperature and fuel and oxidant availability. The temperature increase down the channel is primarily due to the exothermic cell reactions; overpotential losses, shift reactions and the charge transfer reactions are exothermic in nature.

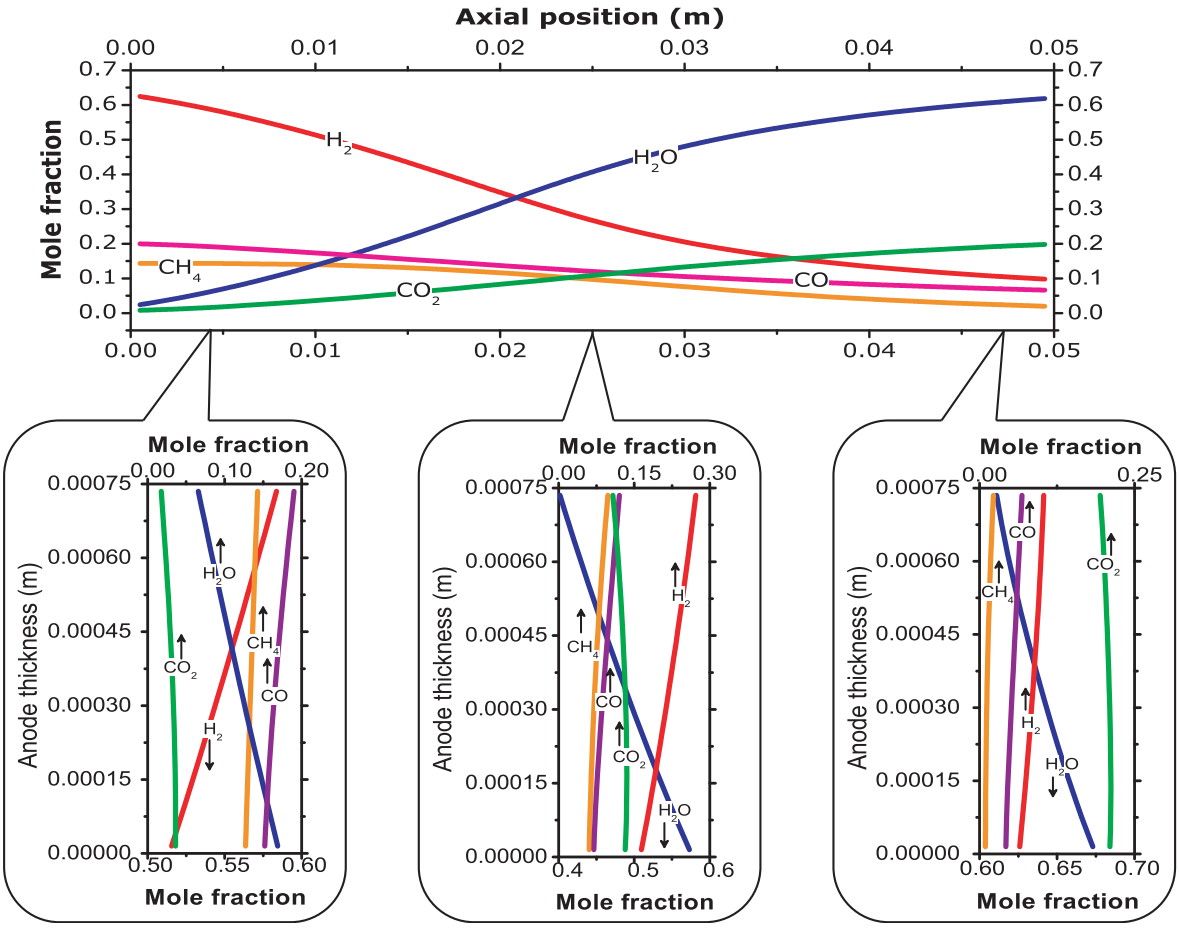

Figure 7.6: Species profiles within the fuel channel and anode. The inlet fuel consists of 14% CH_4, 63%H_2, 2% H_2O, 20% CO and traces of CO_2, which is 60% pre-reformed fuel resulting from an initial composition of 60% CH_4 and 40% H_2O. The drop down panels shows the species profiles across the anode thickness at various axial positions.

7.3.3 Species profiles

The species distribution within the fuel channel and the anode is shown in Fig. 7.6. The top panel displays the species distribution along the fuel channel, while the drop down panels depict the profiles across the anode thickness at selected axial positions. A 5 cm long cell is considered for this calculation. The inlet fuel in this case consists of 14% CH_4, 63%H_2, 2% H_2O, 20% CO, and traces of CO_2 (all % are vol). This mixture, essentially resulting from 60% vol. CH_4 and 40% vol. H_2O after 60% pre-reforming. CH_4, H_2, and CO are consumed along the cell length within the anode, while the product (H_2O and CO_2) concentration increases. CH_4 is primarily consumed by the reforming reactions, while H_2 is depleted by the electrochemical reactions. Although, CO can participate in charge transfer reactions, in the analysis carried out here, H_2 is considered to be the only electrochemically active species and hence the depletion of CO observed here is principally due to the shift reaction. H_2O and H_2 have opposite fluxes, as is evident from the drop down panels. H_2 has flux towards the three-phase boundary where it is consumed by the charge transfer reactions. At the same time

H_2O is produced at the three-phase boundary by the electrochemical oxidation of H_2, and the product H_2O diffuses towards the fuel channel, leading to a flux away from the three-phase boundary.

7.3.4 Surface coverages

Figure 7.7 displays the surface coverages of major surface adsorbed species, for a 5 cm long cell running on 14% CH_4, 63%H_2, 2% H_2O, 20% CO and traces of CO_2. The bottom panel shows the coverages along the three-phase boundary. Coverage of oxygen increases along the three-phase boundary down the channel length. It should be noticed that the coverage of oxygen is a result of dissociative adsorption of H_2O. Since the concentration of H_2O increases along the channel length, the coverages for oxygen also increases. Close to the channel inlet most of the surface is covered by CO and hydrogen. Nevertheless, coverages of both CO and hydrogen decreases down the three-phase boundary length. Though the mechanism is ineffective in predicting the carbon deposition quantitatively, qualitative agreement with experimental observations has been reported in the previous chapter.

Negligible amounts of C deposition can be ascertained near the inlet. Down the channel length the free Ni surface area increases, possibly due to increasing desorption rate with increasing temperatures, and to the consumption of CO and H_2 by shift and electrochemical reactions. The drop up panels present the coverages across the anode thickness at selected axial positions. In all cases hydrogen has lower coverage near the three- phase boundary compared to the electrode/channel interface, emphatically due to the electrochemical oxidation of hydrogen. But oxygen coverages show an opposite trend to that of hydrogen. Oxygen has higher coverage near the three-phase boundary, primarily due to the higher concentrations of H_2O close to the three-phase boundary. Carbon has a trend similar to that of hydrogen; low coverages near the TPB due to the suppression of coking by higher H_2O concentration.

7.3.5 Density, velocity, and pressure drop

The distribution of density and velocity in the air channel is shown in Fig.7.8(a). The density decreases close to the inlet due to the temperature increase and since there is not much of oxygen depletion near the inlet the velocity increases slightly. As the reforming begins the temperature again starts to decrease resulting in a slightly increased density. The density further decreases, since air is consumed down the channel. The velocity also tends to decrease down the channel but near the exit. Close to the exit velocity increases due to the increasing temperature. But decreases further due to O_2 depletion. However, it should be noticed that the velocity changes in the air channel are indeed negligible.

Figure 7.8(b) presents distribution of velocity and density in the fuel channel. Unlike in the cathode compartment, where there is a mass depletion due to the consumption of O_2 at

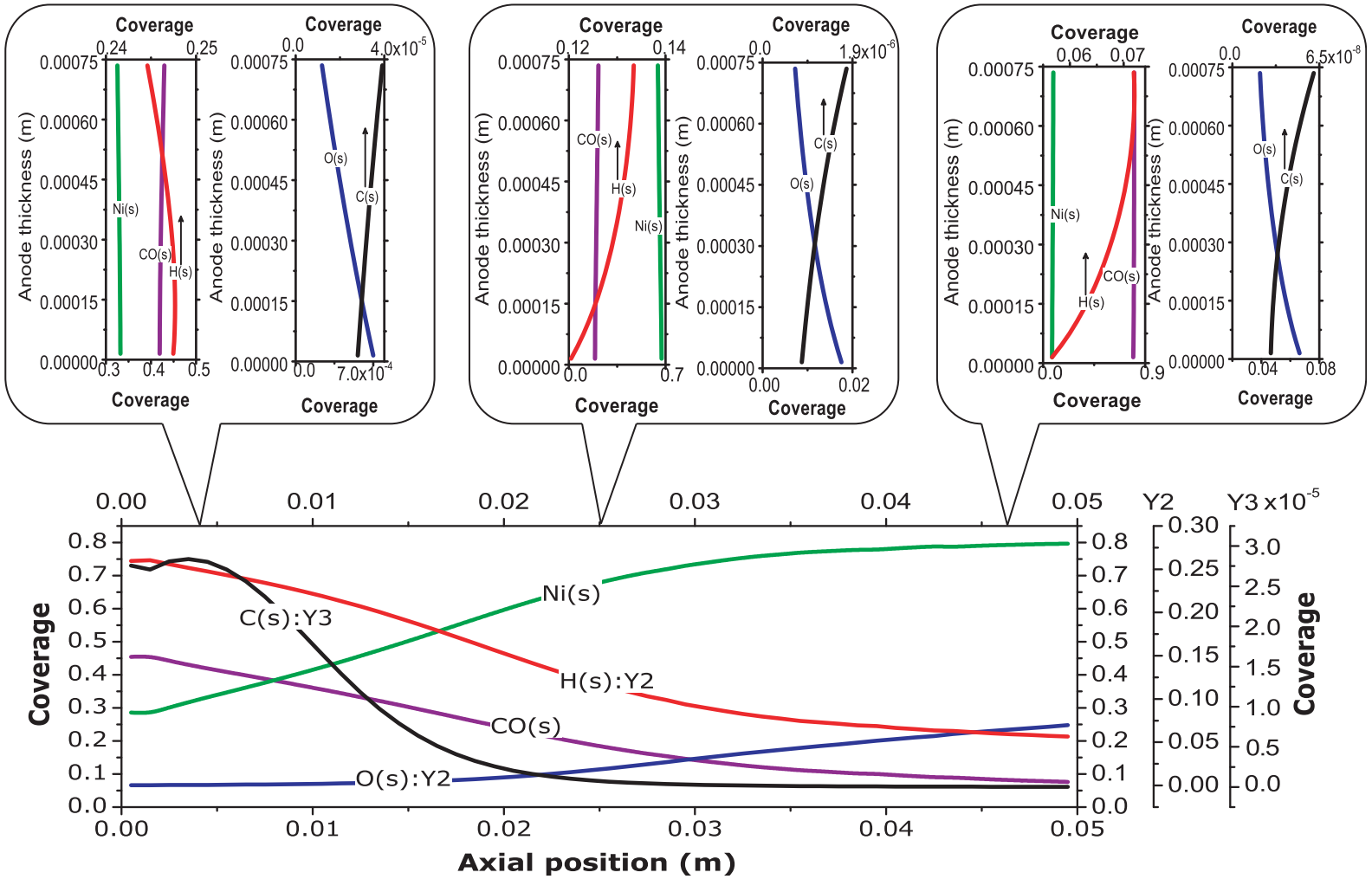

Figure 7.7: Surface coverages of major adsorbed species for a 5cm long cell running on 14% CH_4, 63%H_2, 2% H_2O, 20% CO and traces of CO_2. The bottom panal show the coverages along the three-phase boundary and the top panels display coverages across the anode thickness.

the three-phase boundary, mass is added into the anode compartment due to the electrochemical production of H_2O. In other words the mass depletion at the cathode side results in an equivalent mass addition at the anode side. Here density and velocity follow opposite trends. Density decreases down the channel due to the increasing temperature, while the velocity increases due to the increasing temperature and mass addition at the three-phase interface.

The pressure drop across the anode for a cell operating isothermally at 0.7 V is shown in Fig. 7.9. The anode is 750 μm thick and the inlet fuel consists of 40% CH_4 and 60% H_2O. The pressure drop principally follows the trend of current density. Higher current density regoins within the cell lead to higher pressure drop due to higher production of H_2O at the three-phase interface.

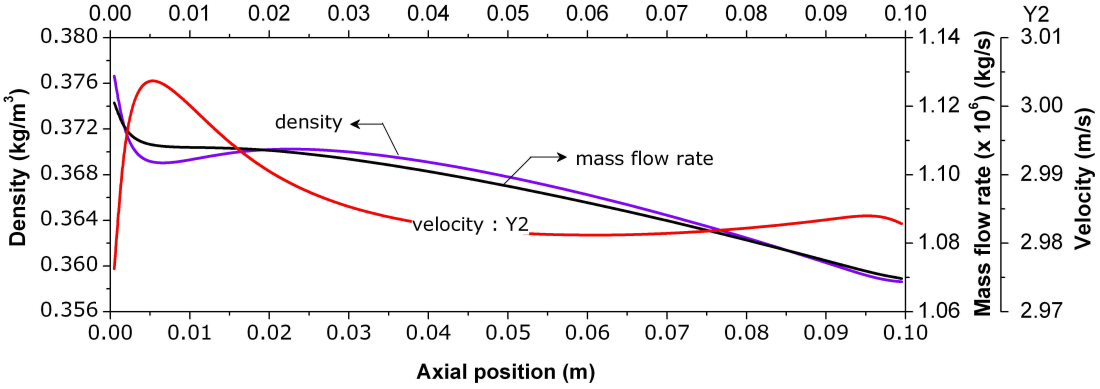

(a)

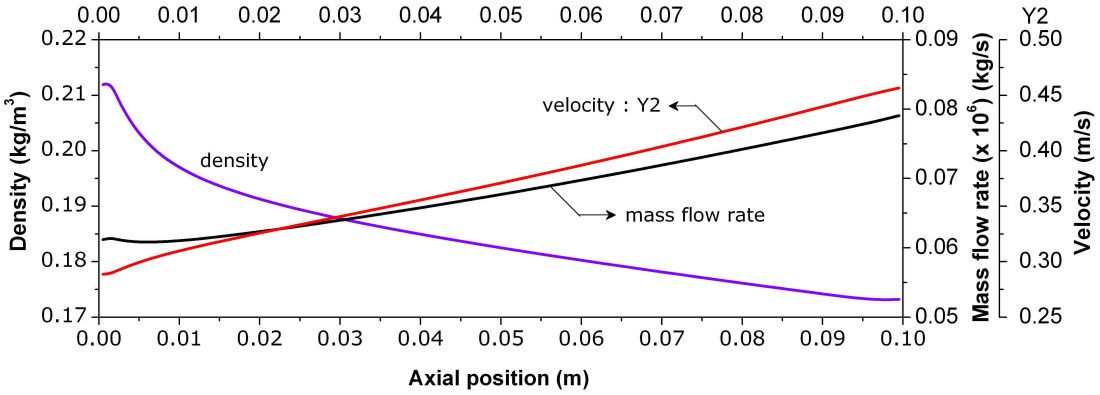

(b)

Figure 7.8: Velocity and density distributions within the flow channel. (a) Air channel, (b) Fuel channel. Air enters the cathode at ~ 2.975 m/s.

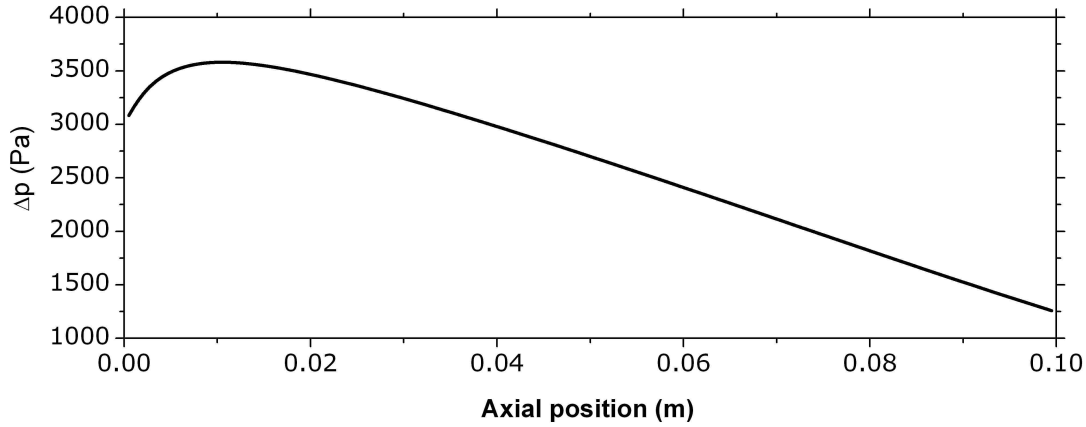

Figure 7.9: Pressure drop across the 750 μm anode for a cell operating at 0.7 V. Inlet fuel stream consists of 40% CH_4 and 60% water.

7.4 Efficiency analysis

Given a cell geometry, the performance of a SOFC is strongly dependent on the operating conditions and the inlet fuel composition. Since SOFCs offer a wide range of operating possibilities identifying the effect of operating conditions such as air flow rate, inlet fuel composition etc. on the efficiency and power density are critical for choosing appropriate operating conditions for SOFCs. For example varying levels of pre-reforming will result in different fuel utilization and power density. Operating in the region of maximum efficiency usually results in a very low power density, requiring large cell volume to deliver the required power output. Operating in the region of maximum power density will generally lead to low efficiency [118]. Hence often one has to operate in a region which delivers reasonable efficiency and power density [119]. On the other hand material cost can be optimized by judicious choice of catalyst loading and the cell geometry. For example an anode supported cell would be preferable choice for hydrocarbon fuels. But the amount of catalyst loading and anode thickness for optimal performance is a design parameter [120].

There are many discussions in the literature on the efficiency analysis of fuel cells. The efficiency of a cell is usually expressed as a product of thermodynamic efficiency η_{th}, voltage efficiency η_v, and the fuel utilization η_u [121, 118]

$$\eta = \eta_{th}\eta_v\eta_u. \tag{7.4}$$

The reversible voltage E_{rev} is defined as

$$E_{rev} = \frac{\Delta G}{n_e F}, \tag{7.5}$$

and defining the thermonuetral voltage or the reaction voltage E_{th} as

$$E_{\mathrm{th}}^{0} = \frac{\Delta H}{n_{\mathrm{e}} F}, \tag{7.6}$$

the thermodynamic efficiency of the fuel cell can be written as

$$\eta_{\mathrm{th}} = \frac{\Delta G}{\Delta H} = 1 - T\frac{\Delta S}{\Delta H} = \frac{E_{\mathrm{rev}}}{E_{\mathrm{th}}^{0}}. \tag{7.7}$$

The voltage efficiency or the part load efficiency is defined as

$$\eta_{\mathrm{v}} = \frac{E_{\mathrm{cell}}}{E_{\mathrm{rev}}}. \tag{7.8}$$

The fuel utilization, defined as the ratio of delivered current to stoichiometric current depends on the operating voltage, fuel and air flow rate, available specific area for internal reforming and the cell geometry [121]

$$\eta_{\mathrm{u}} = \frac{W\int_{0}^{L} i\mathrm{d}x}{\dot{n}_{\mathrm{fuel}} nF}. \tag{7.9}$$

With these definition Eq. 7.4 can be written as

$$\eta = \frac{E_{\mathrm{rev}}}{E_{\mathrm{th}}}\frac{E_{\mathrm{cell}}}{E_{\mathrm{rev}}}\eta_{\mathrm{u}}. \tag{7.10}$$

Based on a co-flow configuration, the effect of various parameters on cell performance has been studied systematically. The study covers the effect of (a) air flow rate, (b) anode thickness, (c) steam to carbon ratio, (d) specific area available for surface reactions, and (e) extend of pre-reforming on cell efficiency and power density. Though the model predicts many variables such as conversion, selectivity, temperature and species distribution, overpotential losses and polarization resistances, they are not discussed in detail here. In all cases calculations are carried for adiabatic as well as isothermal operation. In calculations modeling adiabatic operation the outer interconnect walls are assumed to be adiabatic. All calculations modeling isothermal operation are carried out for a constant temperature of 800°C. Furthermore, in all cases the cell is assumed to operate at a constant voltage of 0.7 V.

7.4.1 Air flow rate

Maintaining high air flow rates to keep the cell temperature within the limits of durable electrode performance is essential for long term operation of SOFCs. However, the amount of excess air required depends on the inlet fuel composition. For example an internally reforming cell requires less excess air than a cell operating on pure hydrogen fuel. However, it is well known that high operating temperature results in better cell performance, and hence an inordinate excess air flow rate can dramatically reduce the cell performance by lowering the

cell temperature. Therefore, one has to be very careful when choosing the amount of excess air, which can result in an optimum balance between cell performance and cell durability.

In the calculations carried out here, excess air is defined in terms of air number λ defined as

$$\lambda = \frac{\dot{n}_{\text{air}}}{\dot{n}_{\text{fuel}} L_{\text{min}}}, \tag{7.11}$$

where

$$L_{\text{min}} = \frac{O_{\text{min}}}{X^{o}_{O_2}}. \tag{7.12}$$

In the above equations $\dot{n}_{\text{fuel}}$ is the molar flow rate of the fuel stream, O_{min} is the minimum O_2 required for the complete oxidation of the inlet fuel and $X^{o}_{O_2}$ is the concentration of O_2 in the cathode stream.

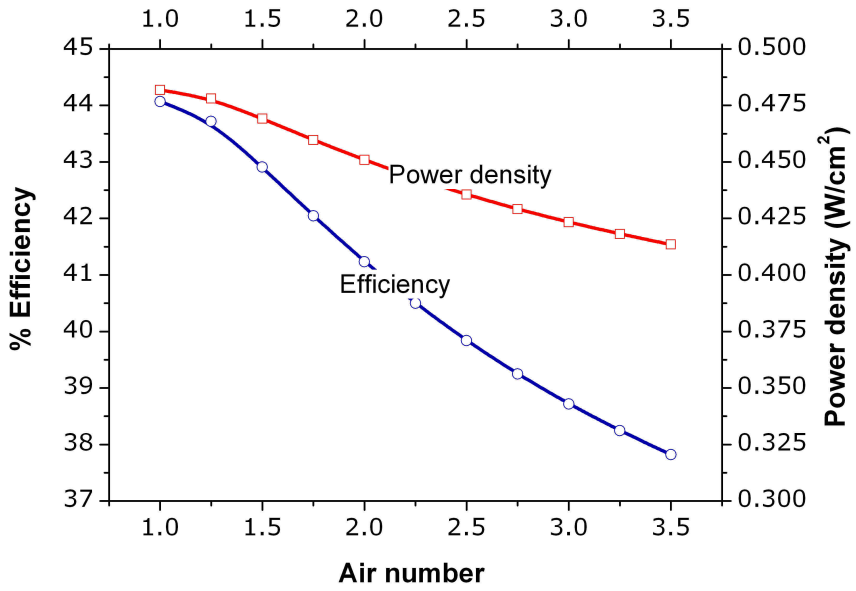

Figure 7.10: Efficiency and power density for adiabatic condition as a function of air number. Inlet fuel stream entering at 800°C consisting of 40% vol. CH_4 and 60 % vol. H_2O and cathode inlet stream (air) entering at 650°C.

Figure 7.10 shows the efficiency and power density for a fuel consisting of 40% vol. CH_4 and 60% vol. H_2O as a function of air number. Fuel and air streams are assumed to enter the cell at 800°C and 650°C, respectively. The MEA parameters and other operating parameters are listed in Tables 7.2 and 7.3. It is quite apparent from the figure that both efficiency and power density decrease with increasing air flow rate, since in the case of non isothermal operation an increase in air flow rate decreases the overall cell temperature resulting in reduced average current density and hence decreasing fuel utilization.

However, the trend reverses when the cell is operated isothermally (Fig. 7.11). In this case both efficiency and power density increase because of the reduced air depletion with an

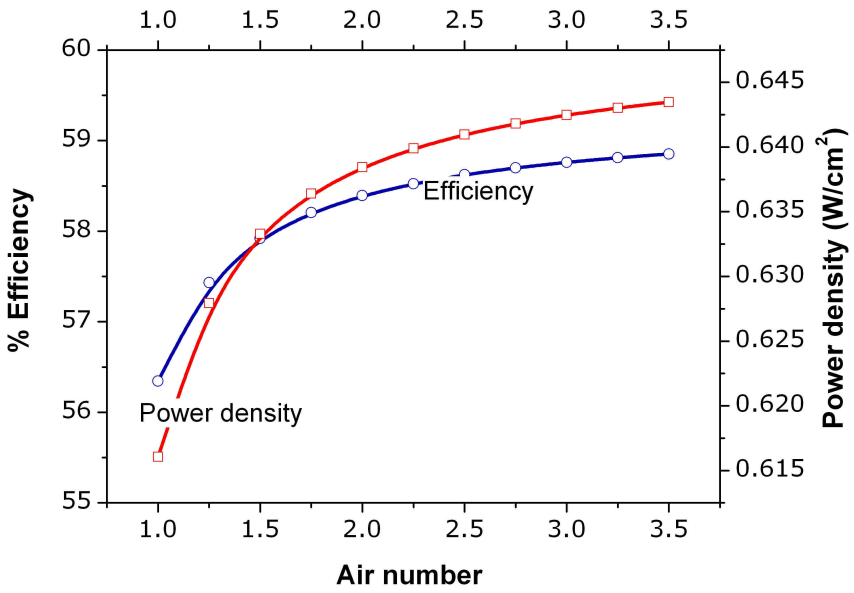

Figure 7.11: Efficiency and power density for isothermal condition (800°C) as a function of air number. Inlet fuel stream consists of 40% vol. CH_4 and 60% vol. H_2O, air is the cathode feed.

Table 7.2: Cell geometry and operating conditions for various cases under consideration

Sl.	MEA	l(cm)	Fuel inlet condition 800°C			Air Nr.	Comments
			CH_4%	H_2O%	υ(cm/s)		
(a)	Table 7.3	10	40	60	30	Variable	- - - - -
(b)	Table 7.3	10	40	60	30	1	Variable anode thickness
(c)	Table 7.3	10	- -	- -	30	3	Variable s/c ratio
(d)	Table 7.3	10	40	60	30	1	- - - - -
(e)	Table 7.3	5	- -	- -	30	5	Air inlet at 600°C and various levels of pre-reforming

increasing air flow rate. Furthermore, isothermal operation results in higher efficiency and power density compared to non-isothermal case. The maximum efficiency for non-isothermal operation is 44%, while isothermal operation results in a maximum efficiency of 59%. It should be noticed that since the cell is operating at constant voltage of 0.7 V and same inlet fuel composition for all cases, the vital factor for resulting power density and efficiency is the fuel utilization as defined by Eq. 7.9. Therefore, in an operating stack, each cell can lead to different levels of fuel utilization and hence different efficiency levels depending on the temperate distribution, which strongly depends on the cell's position within the stack and the temperatures of the adjacent cells.

Table 7.3: MEA parameters

Parameters	Values	Units
Anode		
Thickness (l_a)	0.750	mm
Average pore radius (r_p)	0.50	μm
Average particle diameter (d_p)	2.50	μm
Specific area (A_s)	1025	cm^{-1}
Porosity (ϵ)	0.35	
Tortuosity (τ)	3.80	
Charge transfer coefficient (β_a)	0.50	
Electrolyte		
Thickness (l_e)	25.0	μm
Cathode		
Thickness (l_c)	30.0	μm
Average pore radius (r_p)	0.50	μm
Average particle diameter (d_p)	2.50	μm
Porosity (ϵ)	0.35	
Tortuosity (τ)	3.80	
Charge transfer coefficient (β_a)	0.5	
Interconnect		
Thickness l_i	300	μm

7.4.2 Anode thickness

Though SOFC can be either of anode, electrolyte or cathode supported, in the case of cells running on hydrocarbon fuels, anode supported cells may be preferable to the others for the reasons of internal reforming. However, the optimal anode thickness required to support the cell mechanically and to achieve the desired level of internal reforming and optimal cell performance is rather a difficult task.

Figure 7.12 displays the influence of the anode thickness on efficiency and power density for a cell operating on 40% vol. CH_4 and 60% vol. H_2O under adiabatic conditions. Quite surprisingly there turns out to be an optimal anode thickness at ~0.5mm, maximizing the efficiency and power density in the case of adiabatic operation. In every case the fuel has to undergo internal reforming to produce H_2 and CO which further participates in the charge transfer reactions at the three-phase boundary. However, in the case of thin anodes the short diffusion path (~0.2-0.4 mm) available for the fuel before reaching the three-phase boundary limits the amount of H_2 and CO produced by internal reforming and hence leads to a low average current density, efficiency, and power density. As the thickness increases, the possibility for the fuel to undergo reforming to produce H_2 and CO also increases. However, the great extent of internal reforming achieved from the longer diffusion path also leads to larger temperature drops close to channel inlet and hence results in decreased performance. Thus, there turns out to be an optimal anode thickness where the efficiency and power density

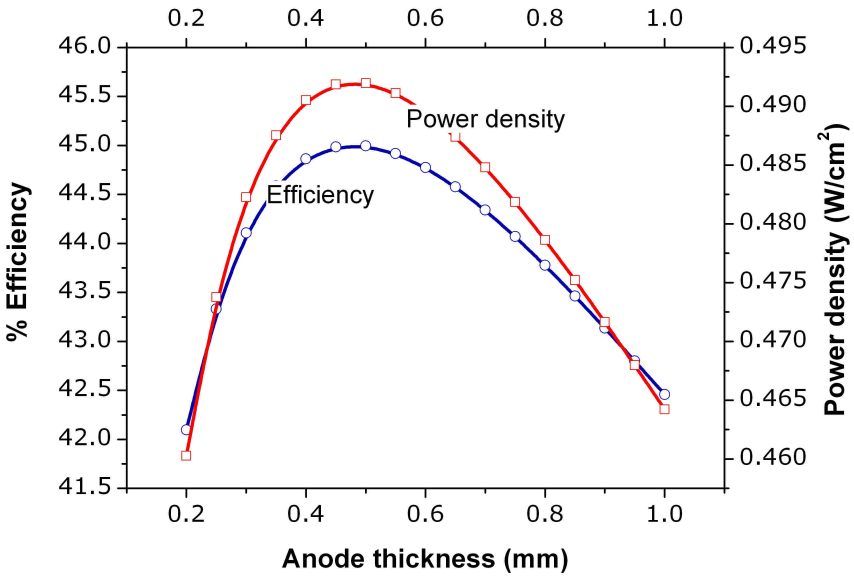

Figure 7.12: Effect of anode thickness on efficiency and power density for a cell operating under adiabatic conditions. The inlet fuel consists of 40% vol. CH_4 and 60% vol. H_2O entering at 800°C. Cathode inlet is assumed to be air at 650°C.

reaches a maximum. However, it should be noticed that the optimum thickness can vary with the operating conditions, such as fuel composition, inlet temperature, velocity etc.

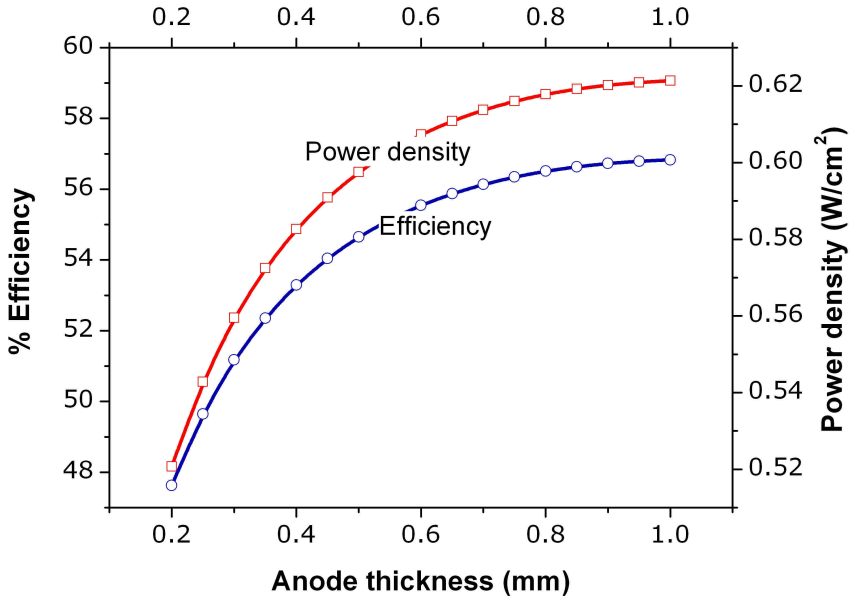

Figure 7.13: Effect of anode thickness on efficiency and power density for a cell operating under isothermal conditions. The inlet fuel consists of 40% vol. CH_4 and 60% vol. H_2O, air is the cathode stream.

Figure 7.13 presents the efficiency and power density as a function of anode thickness for the case of a cell operating isothermally and the same inlet fuel composition as in the adiabatic case. In this case both efficiency and power density increases with increasing anode thickness. Furthermore, isothermal operation results in better performance than adiabatic operation. A maximum efficiency of 59% is achievable with isothermal operation, while the maximum possible in the case of adiabatic operation is 45%.

7.4.3 Stem to carbon ratio

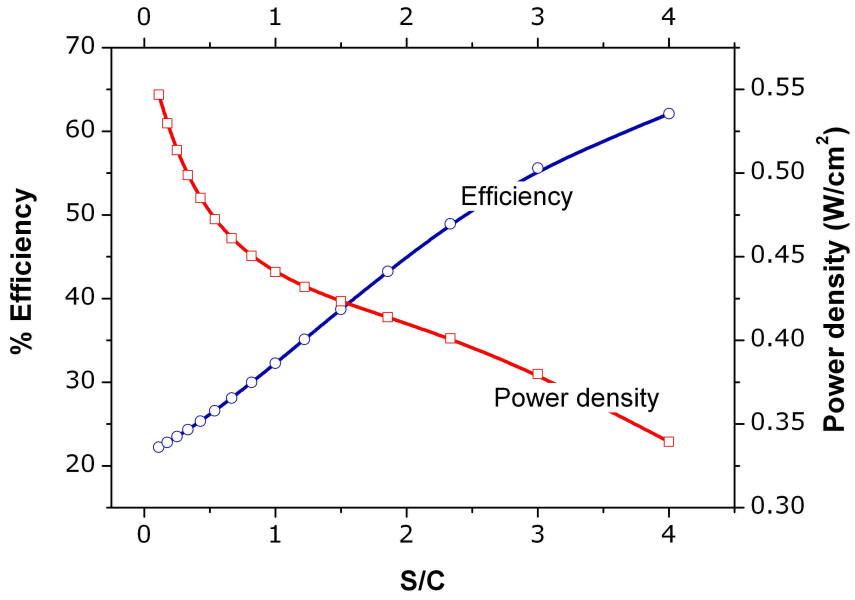

Figure 7.14: Efficiency and power density as a function of steam to carbon (s/c) ratio in the inlet fuel stream for a cell operating adiabatically. Fuel is assumed to enter at 800°C and air at 650°C.

It is quite well known that Ni based anodes are prone to coking while running on hydrocarbon fuels [13, 52, 16]. Therefore, it is quite important to have enough steam present in the inlet fuel to suppress coking. Figures 7.14 and 7.15 respectively present the influence of steam to carbon (s/c) ratio on the performance of an adiabatically and isothermally operating cell. In both cases the efficiency improves with increasing steam content in the inlet fuel stream, while the power density decreases with increasing steam content. The decrease in power density is due to fuel dilution effect; diluted fuel results in a lower average current density and for the cases studied here power density solely depends on the current density due to the constant operating voltage. Though the average current density decreases, the efficiency increases with increasing steam content. This is essentially counter intuitive. One would expect decreasing efficiency with increasing steam dilution, which is certainly true for the case of maximum efficiency analysis. However, one should notice that the analysis

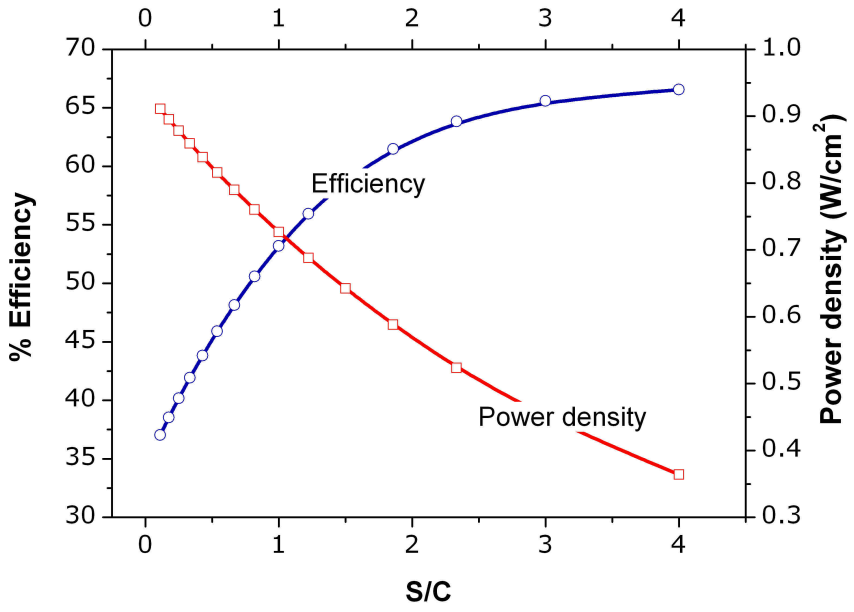

Figure 7.15: Efficiency and power density for as a function of steam to carbon ratio (s/c) in the inlet fuel stream for a cell operating isothermally at 800°C. For call cases the cathode stream is assumed to be air.

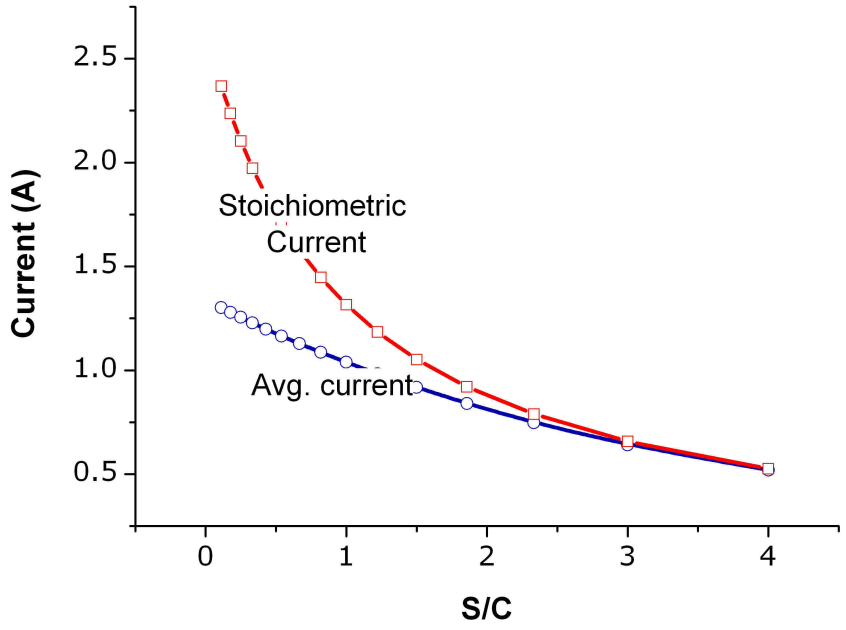

Figure 7.16: Average current and stoichiometric current for varying steam to carbon ratio.

carried out here is for a particular cell geometry, and the fuel utilization for a particular cell depends on the cell dimensions. From the definition of efficiency (Eq. 7.4) it is evident that

for a given cell potential, efficiency strongly depends on the fuel utilization, since the thermoneutral voltage E_{th} is always ~ 1.2 V. At low s/c ratios the stoichiometric current is much higher than the average current delivered by the cell, leading to low fuel utilization and hence low efficiency. However, as the fuel dilution increases the stoichiometric current approaches the delivered current resulting in increased fuel utilization and hence efficiency. Figure 7.16 shows the stoichiometric current and average current for the case of cell operating at 800°C.

Here, like in cases mentioned above isothermal operation results in improved cell performance. In the case of s/c ratio a higher efficiency resulting from the higher fuel utilization leads to reduced power density, which would require large cell areas to draw the required volumetric power density. On the other hand operating conditions providing high power density result in a very low efficiency. Therefore, one has to make a judicious choice of steam dilution, resulting in a balanced power density and efficiency.

7.4.4 Specific area

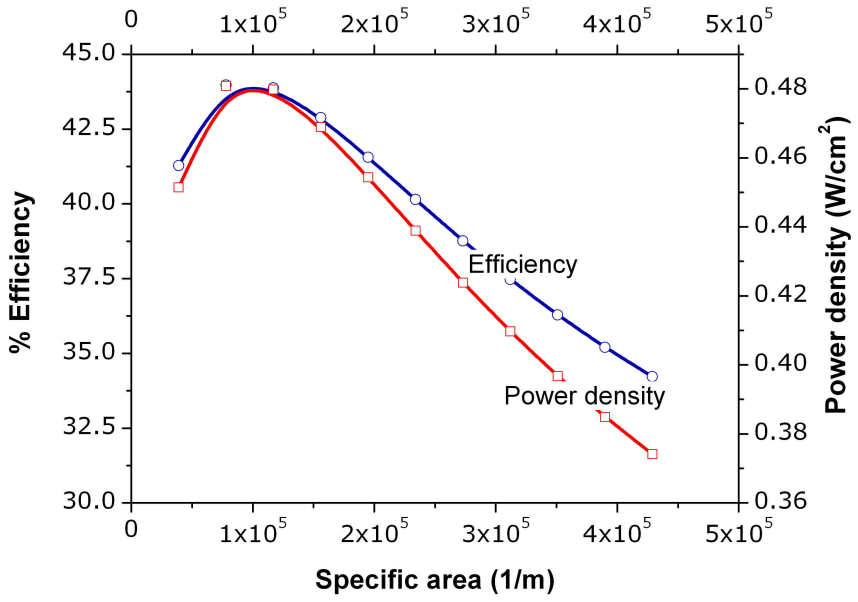

Figure 7.17: Effect of specific area on efficiency and power density for a cell operating adiabatically. Inlet fuel is assumed to consist of 40% vol. CH_4 and 60% vol. H_2O entering at 800°C, and the air stream is assumed to enter the cathode at 650°C.

For heterogeneous reactions to proceed, it is quite important to have sufficient catalytically active surface area. In literature, the amount of catalyst used in the anode usually is expressed in terms of weight percentage (wt%). However, from chemisorption measurements of sample anode, it is possible to get insight on the available active surface area. A large catalytically active surface area can be viewed as a correspondingly large amount of catalyst material present in the anode, and vise versa. Figure 7.17 shows the effect of specific area

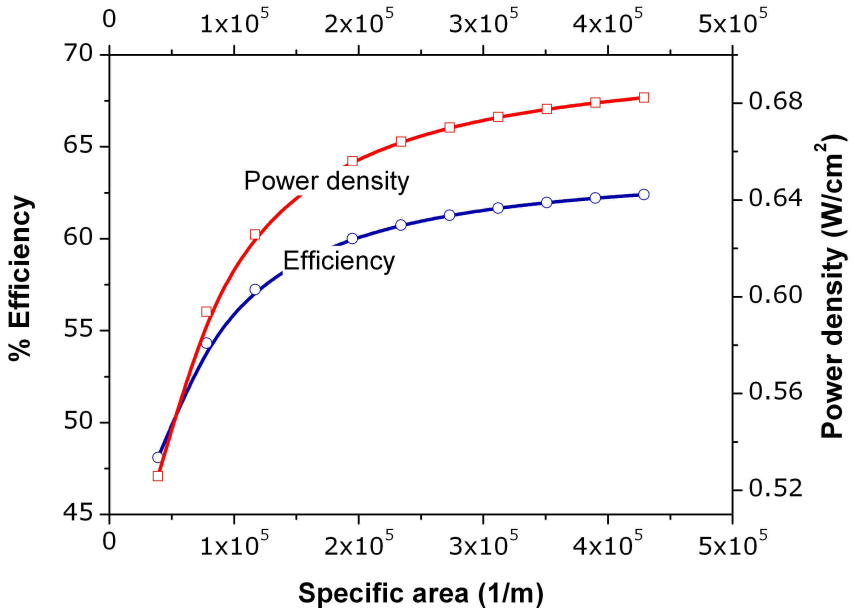

Figure 7.18: Effect of specific area on efficiency and power density for a cell operating isothermally. Inlet fuel is assumed to consist of 40% vol. CH_4 and 60% vol. H_2O entering at 800°C. Cathode stream is assumed to be air.

(area/volume) on the cell performance for a cell operated adiabatically. Both efficiency and power density are found to attain a maximum value at an available specific area of $\sim 1\times10^5$ (1/m). Large amount of catalysts can lead to excessive reforming thereby decreasing the temperature near the inlet of the cell, resulting in a decrease in performance. A poor availability of catalytically active area results in lower production of synthesis gas to participate in the charge transfer reactions, thereby resulting in a lower average current density.

However, in the case of isothermal operation, both power density and efficiency is found to increase with increasing specific area (Fig. 7.18). Moreover, isothermal operation results in better efficiency and power density compared to adiabatic operation. Therefore, it is quite possible to have varying amount of catalysts present in different unit cells of the stack, depending on its position within the stack to achieve maximum possible performance.

7.4.5 Pre-reforming

Though the focus of this thesis is on direct internal reforming, the existing applications use some extend of pre-reformed fuel. Therefore, a systematic study to understand the influence of non-reformed and pre-reformed fuels on cell efficiency is carried out. It is well known that direct internal reforming can result in reduced cost and increased overall efficiency of the system. However, it is quite convincing from Fig. 7.19 that, the efficiency of the fuel cell is higher for pre-reformed fuel. Both efficiency and power density increases with extent of pre-reforming for both adiabatic and isothermal case (Fig. 7.20).

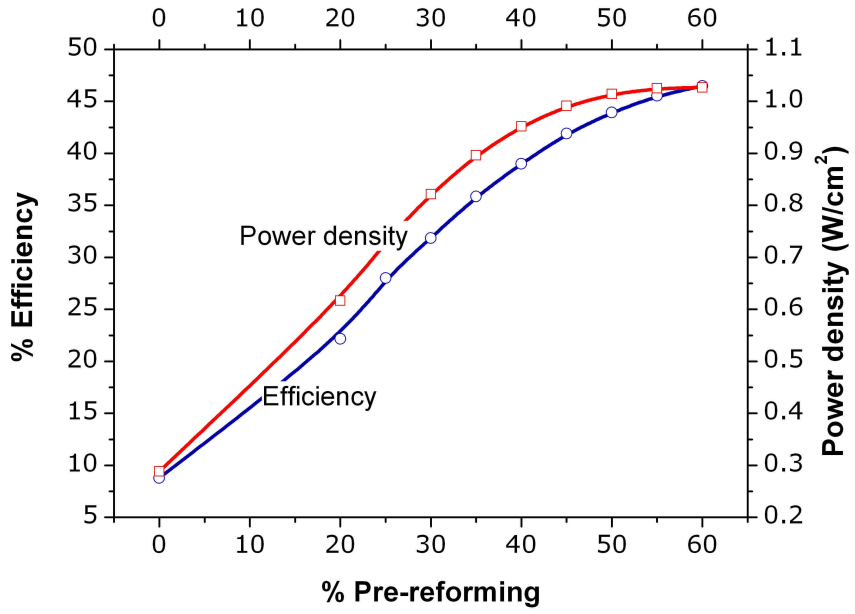

Figure 7.19: Effect of pre-reforming on efficiency and power density under adiabatic condition. In call cases the pre-reformed fuel is assumed to enter at 800°C and air at 600°C. The non-reformed fuel is assumed to consist of 60% vol. CH_4 and 40 % vol. H_2O.

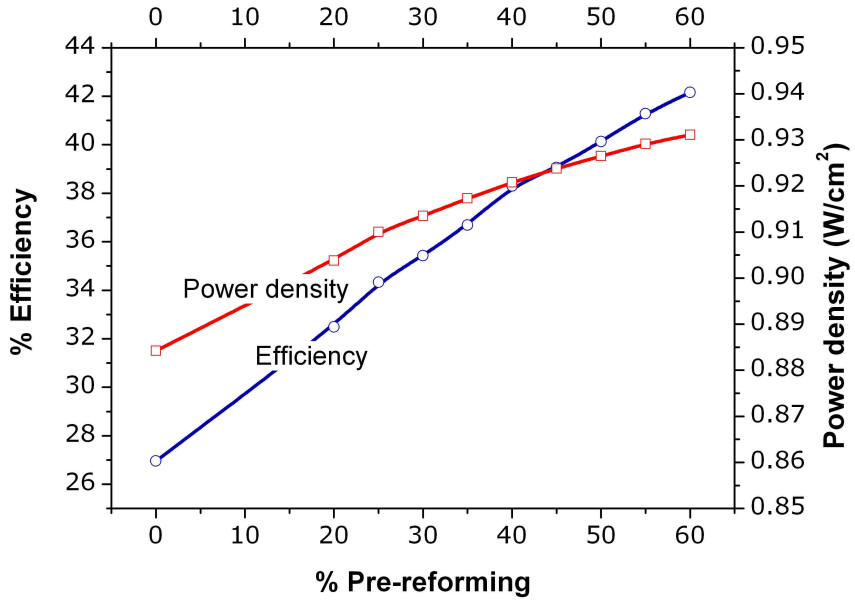

Figure 7.20: Effect of pre-reforming on efficiency and power density under isothermal condition (800°C). The non-reformed fuel is assumed to consist of 60% vol. CH_4 and 40 % vol. H_2O.

In both cases the non-reformed fuel is assumed to consist of 60% vol. CH_4 and 40% vol. H_2O. Unlike in other cases, adiabatic operation results in better performance of the cell

with increasing extent of pre-reforming. For example with 60% pre-reforming, adiabatic operation results in ~45% efficiency, while isothermal operation results in ~42% efficiency. However, with the lowest extend of pre-reforming considered here (20%), adiabatic operation results in lower efficiency and power density than isothermal operation. With increasing extent of pre-reforming, the H_2 content of inlet fuel increases, which results in higher cell temperatures leading to higher performance. While the non-reformed fuel results in internal reforming leading to temperature drop and hence lower power density and efficiency. Furthermore, due to the short reactor length considered here, the fuel utilization efficiency turns out to be lower for non-reformed fuel. This also leads to the lowering of overall efficiency. However, it should be noticed that with increasing levels of pre-reforming, increasing amounts excess air to keep the cell temperature within the limits would be required, and the system should be designed to utilize the waste heat produced by the cell.

7.5 Summary

Based on detailed models of transport and chemistry the effect of various parameters on cell performance for a particular cell geometry has been analyzed systematically. The most important factor for optimal cell performance has been found to be the resulting temperature profile within the cell. Judicious choice of steam dilution of the inlet fuel has to be made, that can well suppress the coking, while achieving reasonable efficiency and power density. As a remarkable outcome, excessive amount of catalysts and highly thick anodes has been found to have detrimental effect on cell performance in the case of direct internal reforming. Furthermore, though direct internal reforming is known to increase the overall efficiency of the system, the efficiency of the fuel cell itself is found to be higher for the case of pre-reformed fuel. In all cases, except for the case of pre-reformed fuel, isothermal conditions resulted in better cell performance. Therefore, in the case of direct internal reforming, it is quite important to design the cell in a way to achieve more or less isothermal operation of the stack, which can result in higher performance.

Chapter 8

Summary and outlook

Numerical modeling combined with experimental validation is extremely important for fuel cell research. Accurate numerical models describing physico-chemical processes are expected to be cost effective in the further development of SOFC technology. Although there is a plethora of numerical modeling and simulation in SOFC literature, those with experimental validation covering a wider range of operating conditions are scarce. This thesis describes numerical simulation and its experimental validation based on detailed description of transport processes, elementary heterogeneous chemistry, and electrochemistry. Transport through porous medium was described by the Dusty Gas Model (DGM).

The accuracy of various porous medium transport models such as Dusty Gas Model (DGM), Mean Transport Pore Model (MTPM), Modified Fick Model (MFM), Modified Maxwell-Stefan Model (MMS), and Generalized Maxwell Stefan Model (GMS) under reaction conditions were investigated and compared with experimental results. For comparison purpose third party experimental data was used in this work [64]. The experimental setup consisted of a 0.75 mm thick porous Ni/YSZ anode sandwiched between two flow channels of 6.25 mm^2 cross sectional area. One of the channels denominated as the fuel channel was fed with a gas mixture of 20% CH_4, 2.8% H_2O, and 77.2% Ar. While the other channel denominated as electrolyte channel was fed with a gas mixture of ~50% H_2O or CO_2, ~2% H_2O, and 48% Ar. The setup allowed the transport of chemical species between the two flow channels through the porous medium. As CH_4 diffuses across the porous medium it reacts with the counter diffusing reforming gas. While the inlet composition was kept constant, the flow rate was changed from 50 to 150 sccm. The range of flow rates were so chosen to operate under a kinetic regime rather than at equilibrium. Various porous medium transport model predictions such as DGM, MTPM, MFM, MMS, and GMS coupled with elementary reaction mechanism and 1D channel flow models were compared with the result of experimental measurements. Except GMS all other models considered Knudsen diffusion. All models, except MMS accounted for the viscous transport. GMS model failed to predict some cases. Although, in certain cases GMS predictions were accurate for one of channel exit concentrations, it failed to predict the other channel exit concentrations. In general, DGM and MFM

lead to almost identical results which were found to match the experimental results closer than the predictions by the other models. Similarly, MTPM and MMS predictions were almost the same.

Irrespective of the large body of experimental data available on solid oxide fuel cell performance, those which complement the parameters and variables studied here are really scarce. Therefore, an approach based on button cell modeling followed by planar cell modeling was adopted. The button cell modeling guaranteed physically realistic electrochemical model parameters which were then extended to planar cell modeling. As a base case for deducing electrochemical model parameters such as exchange current density, charge transfer coefficient etc. the experiments reported by Liu and Barnett [38] have been modeled using the commercial CFD code FLUENT coupled with user defined functions (UDFs). Electrochemistry model, heterogeneous chemistry model and porous medium transport model are implemented into FLUENT with the help of UDFs, while FLUENT solved the equations describing the flow field. For all operating conditions the model well predicted the experimental observations for high current density region. However, the model predicted open circuit potential (OCV) at higher operating temperatures drastically exceeded the experimental observation. A comparison with equilibrium predictions revealed that the over prediction of OCV by the computational model was primarily due to the erroneous prediction of surface carbon by the multi-step heterogeneous chemistry mechanism. This basically lead to non-equilibrium fuel composition at open circuit conditions and hence the Nernst equation failed to predict the thermodynamic equilibrium potential. However, the model predictions were satisfactory for short circuit conditions. Anodic overpotential showed a noticeable difference from the expected behavior. The anodic overpotentials displayed an abrupt increase at very low current densities and then followed a valley before increasing further at higher current densities. However, this behavior was not detected for low operating temperatures. At OCVs carbon deposition was largest for higher temperatures, and a flow of current was found to mitigate coking. Carbon formation and its subsequent reaction with H_2O was found to play a key role in the resulting surface coverages of other surface adsorbed species at low current densities. Higher dilution with H_2O resulted in higher surface coverages of H and lower coverages of CO compared to fuel with lower steam dilution. As observed in the experiment of Lin et al. [39] the concentration of all reaction products were found to increase at low current densities. However, at higher current densities the concentration of H_2O and CO started to decrease. The evaluated activation energy for the oxidation of H_2O was found to be in good agreement with the experimental finding of Bieberle [11].

The electrochemical parameters deduced from the modeling of button cell experiments were used for planar cell modeling. Thereby ensuring physically realistic model parameters to assist performance predictions, where there is no direct experimental observation to compare with. Based on a co-flow configuration, a number of geometrical and operating parameters has been subjected to study their influence on the resulting cell performance, and

the distribution of various dependent variables. On one hand local properties such as current density, reversible potential, species profiles, and surface coverages have been analyzed and on the other hand overall cell efficiency and power density were studied. Temperature and fuel depletion act counter-actively on the cell's electrochemical performance. Even under fuel rich conditions a drop in local temperature brought down the local current density. This effect was convincingly observed in the case of internal reforming. Internal reforming in co-flow configuration always leads to decrease in temperature near the channel inlet. However, the temperature increased further down the channel due to exothermic cell reactions. Though an increasing temperature should result in an increasing current density, high fuel utilization, increased fuel dilution, and air depletion brings down the current density near the channel exit. Under isothermal operating conditions, however, the current density peaks near the channel inlet, and drops steadily further down the channel due to increased fuel dilution and air depletion.

Since the MEA is quite thin radial uniformity in temperature was observed throughout. However, considerable temperature variation was observed along the axial direction due to internal reforming. The concentration profiles of the species show that H_2 and H_2O always have opposite fluxes. Within the anode, H_2 had a flux towards the three-phase interface where it was consumed, and H_2O had a flux away from the three-phase interface where it was produced electrochemically. However, the profiles of the species concentration within the channel depend on the inlet fuel composition. For example feed rich in H_2 will result in opposite profiles for H_2 and H_2O within the anode, while a feed rich in CH_4 will result in a different profile due to internal reforming. On the surface the main species were found to be hydrogen and CO. Oxygen coverage was also observed in the anode, which principally resulted from the dissociative adsorption of H_2O. Furthermore, the oxygen surface coverage was found to increase down the axial position as a result of increased production of H_2O by electrochemical reactions.

It is quite important to consider the effects of temperature when predicting achievable efficiency and power density of the cell since each unit cell in a stack behaves differently depending on the thermal boundary conditions resulting from the thermal interactions with the neighboring cells. Therefore, the efficiency analysis was carried out for both isothermal and adiabatic conditions, assuming the overall behavior of the stack can be represented by these two extreme thermal boundary conditions. For a given cell geometry, increasing the anode thickness beyond certain limits resulted in adverse cell performance due to the higher extend of internal reforming and the temperature drop thereby. A similar situation was identified for the case of specific catalyst area available for heterogeneous reactions within the anode. The specific active catalytic area directly corresponds to catalyst loading. However, isothermal operation resulted in increased cell performance with increasing anode thickness and specific catalyst area. In SOFC operation it is quite common to deliver the air stream at lower temperature and high flow rate to prevent the cell from overheating due to exothermic

cell reactions. However, higher air flow rates resulted in lower performance due to lower overall temperature in the cell. Although internal reforming is known to result in increased overall efficiency of the system, for the cell itself the efficiency was found to be higher for pre-reformed fuels due to increased fuel utilization. Steam dilution in the inlet fuel was found to have counter-acting effects on the cell performance. While the efficiency increased, the power density decreased with increasing steam dilution of the inlet fuel. The power density decreased mainly due to the diminution of average current density due to fuel dilution, while the efficiency increased because of the diminishing relative difference between stoichiometric current and average current with increasing s/c.

The models presented in thesis are much faster in execution time compared to elliptical CFD models. However, the assumption of plug flow in the channels can leave out certain details of mass and heat transfer when the flow channel dimensions are larger. Furthermore, the inclusion of detailed models for heterogeneous chemistry and porous media transport to simulate a complete fuel cell stack can be computationally very expensive. Especially the evaluation of species fluxes using DGM requires the inversion of an $N \times N$ matrix during every iteration. The work presented in thesis can be extended to simulate a complete stack, by further reducing the transport models. For instance, a fully one dimensional model can be derived by leaving out the details of porous media transport and evaluating the concentration over potentials by analytical expression derived for the case of H_2 fuel. A collection of steady state one dimensional models can be used to simulate transient stacks, by decoupling the temperature equation from the rest of the system, since the time constants for other cell processes are much faster compared to temperature. This methodology is already successfully used for the simulation of automotive catalytic converters [122] and catalytic combustion in gas turbines [123] in our research group. The results presented here are a first step towards a better understanding of the behavior of SOFCs operated with hydrocarbon fuels by coupling detailed models of all relevant physico-chemical processes occurring in a single cell.

Zusammenfassung

Brennstoffzellen sind elektrochemische Einheiten, die chemische in elektrische Energie umwandeln. Im Gegensatz zu anderen Brennstoffzellen sind die Festoxidbrennstoffzellen (*Solid Oxide Fuel Cells, SOFC*) aufgrund ihrer hohen Betriebstemperatur auch für verschiedene Brennstoffe auf Kohlenwasserstoffbasis wie Methan, Ethan, Propan, Butan und Erdgas geeignet, die innerhalb der Zelle reformiert werden können. Mittlerweile steigt auch das Interesse an der Verwendung von flüssigen Brennstoffen wie Methanol und Ethanol für portable Anwendungen. Interne Reformierung kann entweder direkt an der Nickelanode innerhalb der SOFC-Einheit oder an einem separaten Reformierkatalysator erfolgen. Obwohl die interne Reformierung ökonomisch attraktiv ist, bereitet sie noch gravierende Probleme, so dass bislang gebaute SOFCs eine gewisse Vorreformierung benötigen, um die sonst auftretende Leistungsabnahme und verminderte Lebensdauer der Brennstoffzelle zu vermeiden. Die mechanische Stabilität der Brennstoffzelle wird erreicht, indem eine Komponente dicker ausgeführt wird; die Zellen werden folglich in anoden-, kathoden- und elektrolytgestütze Bauarten unterteilt. Im Falle von Kohlenwasserstoffen als Brennstoff werden häufig anodengestütze SOFCs verwendet, da in ihnen eine bessere interne Reformierung erreicht wird.

In dieser Arbeit werden vor allem die elektrochemische Charakterisierung und Leistungsprobleme in Bezug auf die direkte interne Reformierung in anodengestützten Zellen betrachtet. Daneben werden auch vorreformierte Brennstoffe diskutiert. Da Erdgas als optimaler Brennstoff für stationäre SOFC-Anwendungen gilt und da Methan der Hauptbestandteil von Erdgas ist, wird hier hauptsächlich Methan als Brennstoff ausgewählt.

Im ersten Kapitel dieser Dissertation wird einleitend der Entwicklungsstand bei Elektrodenmaterial, Brennstoffen und Brennstoffaufbereitung für aktuell verwendete SOFCs dargelegt. Da der Schwerpunkt dieser Arbeit auf anodengestützen SOFCs liegt, werden die Werkstoffe der Anode ausführlich behandelt. Vor- und Nachteile der internen Reformierung werden in Kapitel 1.2.2 besprochen. Allgemein können die Gesamtkosten der SOFC durch die Verlegung der teuren externen Brennstoffreformierung in das Innere der Zelle vermindert und die Gesamteffizienz erhöht werden. Die interne Reformierung kann andererseits zu Problemen durch Verunreinigung der Anode führen. Deshalb wird meist zumindest ein Teil des Brennstoffes vorreformiert, anstatt die Kohlenwasserstoffe direkt in die Zelle einzuleiten. Die

Struktur der Anode der Zelle bietet allerdings genügend Möglichkeiten für Reformierungschemie. Die Brennstoffmischung wird vom brennstofführenden Kanal durch molekulare Diffusion, Knudsendiffusion und Druckgradienten zur Dreiphasengrenzfläche transportiert. Die elektrochemische Reaktion an der Dreiphasengrenzfläche produziert H_2O und CO_2, die sich mit dem eintretenden Brennstoff mischen und so zur heterogenen Reformierungschemie führen. Die Produkte der elektrochmischen Reaktion werden zum Strömungskanal hin und der Brennstoff in Richtung der Dreiphasengrenzfläche transportiert. Die Reaktionsprodukte verdünnen den Brennstoff mit zunehmender Länge der SOFC, wodurch die elektrische Stromdichte sinkt. Eine niedrigere Stromdichte kann auch durch eine Verringerung des Sauerstoffgehalts im Luftstrom des Kathodenkanals hervorgerufen werden. In Kapitel 2 werden die Grundlagen der heterogenen Katalyse und ihre Bedeutung für SOFCs besprochen. Probleme, die durch Kohlenstoffablagerung während der Alkanreformierung in der SOFC entstehen, werden ebenfalls diskutiert. Ein erstmals verfolgter, neuer Ansatz besteht in der Anwendung eines detaillierten heterogenen Reaktionsmechanismus, um die katalytischen chemischen Reaktionen in der Anode zu modellieren. Alle bislang durchgeführten Modellierungen von SOFCs verwendeten globale Modelle zur Beschreibung der Reformierungschemie der Anode. Der in unserer Gruppe entwickelte, auf dem elementaren Geschehen basierende Mechanismus der Methanreformierung über Nickel ist für höhere Temperaturen im Bereich 500°C-1800°C in dieser Arbeit erweitert worden. Der Mechanismus umfaßt 42 Reaktionen zwischen 6 Gasphasenspezies und 12 auf der Oberfläche adsorbierten Spezies. Die Reaktionsgeschwindigkeiten werden in modifizierter Arrheniusform ausgedrückt. Bei einigen ist eine zusätzliche Funktion zur Modellierung der Bedeckungsabhängigkeit der Aktivierungsenergie hinzugefügt. Der aus Elementarreaktionen bestehende Mechanismus, schließt die Beschreibung der globalen Geschehnisse wie Wasserdampfreformierung, trockene Reformierung, Wasser-Gas-Konvertierung, umgekehrte Wasser-Gas-Konvertierung und Boudouard-Reaktion mit ein.

In der Modellierung von Brennstoffzellen ist die elektrochemische Ladungsübertragung nach wie vor der am wenigsten verstandene Aspekt. Selbst in den einfachsten Fall, der Wasserstoffoxidation, sind mehrere plausible Reaktionspfade vorgeschlagen worden. Wie bei den meisten in der Literatur vorgestellten Simulationen im Zusammenhang mit Brennstoffzellen wird auch in der vorliegenden Arbeit die Elektrochemie durch den phänomenologischen Butler-Volmer-Formalismus beschrieben. Der hier verwendete Butler-Volmer-Formalismus beruht jedoch auf einer Chemie mittels Übertragung von Elementarladungen und unter der Annahme, dass Wasserstoff das einzig elektrochemisch aktive Molekül ist. Diese Vereinfachung wird dadurch gerechtfertigt, dass in dem Fall, bei dem CO und H_2 zusammen in einem elektrochemischen System vorkommen, die elektrochemische Oxidation von H_2 gegenüber der von CO dominiert. Es wird weiterhin angenommen, dass die elektrochemische Reaktion nur an der Dreiphasengrenzfläche stattfindet, welche aus Anode, Gasphase und dem Elektrolyten gebildet wird. In der Realität kann diese Dreiphasengrenze

einige Mikrometer in die Anode hineinreichen. Trotzdem ist die Annahme einer eindimensionalen Phasengrenze im Falle von anodengestützten Brennstoffzellen gerechtsfertigt, da die Eindringtiefe nur einen Bruchteil der tatsächlichen Anodendicke ausmacht.

In Kapitel 3 werden die Prinzipien der Modellierung elektrochemischer Reaktionen hinsichtlich SOFCs angesprochen. Des Weiteren werden verschiedene irreversible Verluste wie Aktivierungsverlust sowie ohmsche und konzentrationsbedingte Verluste erläutert. Die Aktivierungsverluste, die durch die Geschwindigkeit der Ladungsübetragung bestimmt werden, sind stark von der Brennstoffzusammensetzung, der Stromdichte und der Temperatur abhängig. Die Stromdichte wiederum ist von der Betriebsspannung abhängig. Insgesamt sind die Aktivierungsverluste auf der kathodischen Seite der SOFC wesentlich größer als die auf der anodischen. Die ohmschen Verluste werden durch die Temperatur beeinflußt und sind stark vom Material des Elektrolyten abhängig. Zwar tragen auch die Elektroden zum elektrischen Widerstand bei, deren Einfluß ist jedoch gegenüber dem Einfluß des Widerstands des Ionentransports im Elektrolyten vernachlässigbar. Deshalb werden in dieser Arbeit die ohmschen Verluste in den Elektroden vernachlässigt. Die konzentrationsbedingten Verluste werden von den Diffusionsgrenzen für den gasförmigen Fluß im porösen Material ausgelöst. Im Falle von H_2 als Brennstoff ist es möglich, einen analytischen Ausdruck für die konzentrationsbedingten Verluste unter der Annahme equi-molarer Gegendiffusion herzuleiten. Die Umstände sind bei kohlenwasserstoffbasierten Brennstoffen komplizierter. In diesem Fall kann H_2 auch im Anodenraum durch Reformierung gebildet werden. Deshalb werden in dem hier vorgestellten Ansatz die Transportlimitierungen in porösen Medien detailliert mit dem *Dusty Gas* Modell behandelt. Die Berücksichtigung der Konzentrationsverluste beim Lösen der elektrochemischen Gleichungen erübrigt sich damit.

Die numerischen Modelle werden in Kapitel 4 behandelt. Zur Beschreibung dienen elliptische Differentialgleichungen, wobei der Transport insgesamt in zwei Raumdimensionen behandelt wird, mit der Strömung durch Anoden- bzw. Kathodenkanal als eindimensionale Propfenströmung. Der Transport durch die Elektroden wird ebenfalls als eindimensionales Problem behandelt, jedoch orthogonal zur Strömungsrichtung. Mathematisch bilden die Gleichungen ein differential-algebraisches Gleichungssystem, das numerisch gelöst werden muß. Dafür wird die Methode der *Finite Volumen* angewandt. Das Teilsystem algebraischer Gleichungen (elektrochemische Modellgleichungen) kann jedoch vom Rest des Gleichungssystems entkoppelt und mit einem modifizierten Newtonalgorithmus gelöst werden. Der Newtonalgorithmus konvergiert im allgemeinen innerhalb von 3-4 Iterationen. Zur Lösung des restlichen differential-algebraischen Gleichungssystems (*Differential Algebraic Equation*, DAE) wird der numerische Löser LIMEX [117] verwendet. Die Lösungsverfahren für jedes Gleichungssystem werden in den jeweiligen Kapiteln diskutiert, in denen sie verwendet werden. Meist wird ein Raumschrittverfahren (*space marching* Algorithmus) verwendet. Konvektive Terme im Gaskanal werden mit dem *Upwind*-Differenzenverfahren

berechnet. Dies bedeutet, dass die Lösung der Erhaltungsgleichungen an jeder axialen Position im Kanal von der Lösung des im Kanal stromaufwärts angrenzenden Gitterabschnitts abhängt. Die Anfangsbedingungen für jeden axialen Knoten werden entsprechend der konvergierten Lösung des direkt stromaufwärts gelegenen gewählt.

Die in dieser Arbeit vorgestellte Simulation einer Knopfzelle (*button cell*) wurde unter Verwendung des kommerziell erhältlichen CFD-Programms FLUENT [1] durchgeführt. Daran angekoppelt wurden benutzerdefinierte Funktionen (*user defined functions*, UDFs) als Schnittstelle zu DETCHEM [2], einem in unserer Gruppe entwickelten Programmpaket zur Simulation reaktiver Strömungen. Während der Iterationen werden die Konzentrationen und thermodynamischen Zustandsvariablen vom *Fluent-Solver* abgerufen, die wiederum benutzt werden, um mit den von DETCHEM zurückgesendeten Werten zu rechnen.

Flachzellen-SOFCs werden mit einem vereinfachten Strömungsmodell bezüglich des Transports im Anoden-bzw. Kathodenkanal beschrieben. Modelle für den Transport in den porösen Medien wie *Dusty Gas Modell* (DGM), *Modifiziertes Ficksches Diffusionsmodell* (MFM), *Mean Transport Pore Modell* (MTPM), *Modifiziertes Maxwell-Stefan Modell* (MMS) und *Verallgemeinertes Maxwell-Stefan Modell* (GMS) werden ausführlich in Kapitel 4.2 behandelt. Die Anwendbarkeit der verschiedenen Transportmodelle für die Vorgänge in der SOFC wird in Kapitel 5 dargelegt. Insgesamt stimmen die Vorhersagen von DGM und MFM gut mit experimentellen Beobachtungen überein. In allen Fällen ergaben DGM und MFM annähernd identische Ergebnisse. Bei der Entwicklung von DGM und MTPM sind viskose Transportprozesse, die sich aus Druckgradienten ergeben, detailliert mitbetrachtet worden. Jedoch behandeln die beiden den Permeationstransport unterschiedlich. Im DGM sind die porösen Wände als riesige Moleküle (*Dust*) veranschaulicht, die einheitlich im Raum verteilt sind und die durch nicht definierte äußere Kräfte bewegungslos an einem Ort festgehalten werden. Bei MTPM wird angenommen, dass der Transport in der Gasphase in einem Porensystem erfolgt, das durch zylinderförmige Kapillaren mit einer Radienverteilung um den Mittelwert $\bar{r}$ abgebildet wird. Dem viskosen Transport ist bei der Umsetzung von MFM besondere Beachtung geschenkt worden. MTPM und MMS geben auch die experimentellen Ergebnisse qualitativ gut wieder, jedoch schlechter als DGM und MFM.

Die elektrochemischen Parameter sind für die Modellierung von Brennstoffzellen offensichtlich wichtig. Die Kenndaten der elektrochemischen Leistung, die Experimente mit Knopfzellen (button cells) erbrachten, können dabei helfen, elektrochemische Modellparameter herzuleiten. Der hier angepasste Modellierungsansatz, dessen Parameter durch Kalibrierung des Modells anhand der Daten des button-cell-Experiments entstanden, wird anschließend für die Modellierung von flachen Zellen verwendet. Im Gegensatz zu mit Wasserstoff betriebenen button cells, für die es in großem Umfang Daten aus Experimenten verfügbar sind, sind nur wenige Ergebnisse für Methan über einen weiten Temperaturbereich

erhältlich. Experimente mit einer button cell von Liu und Barnett [38] dienen als Grundlage für die Abschätzung der elektrochemischen Parameter des Modells (Kapitel 6).Im Rahmen dieser Arbeit wurde ermittelt, dass für die korrekte Berechnung der Leerlaufspannung bei Verwendung von trockenem Methan als Brennstoff die genaue Vorhersage der Menge an Kohlenstoff auf der Oberfläche entscheidend ist. Allgemein gibt das Modell die experimentellen Daten sehr gut wieder. Abweichungen zwischen Experiment und Modell treten in der Leerlaufspannung, die durch die mangelhafte Vorhersage der Kohlenstoffmenge auf der Oberfläche verursacht werden, auf. Weiterhin werden verschiedene irreversible Verluste und die Bedeckungen der Oberfläche mit den wichtigsten Molekülen und Molekülfragmenten analysiert. Ein nicht erwartetes Verhalten zeigt sich bei der anodischen Überspannung. Bei dem in der vorliegenden Arbeit behandelten Problem nimmt die anodische Überspannung mit steigender Stromdichte zunächst ab. Nach dem Erreichen eines Minimums nimmt sie wieder zu. Ähnliches Verhalten ist bei Experimenten [116], bei denen trockenes Methan verwendet wurde, berichtet worden. Dagegen zeigt die kathodische Überspannung jedoch die übliche Zunahme mit steigender Stromdichte und sinkender Temperatur. Kohlenmonoxid und Wasserstoff sind die vorherrschenden adsorbierten Spezies auf der Oberfläche. Die hohe Betriebstemperatur führt zu Kohlenstoffablagerungen bei Leerlaufspannung. Der Kohlenstoff auf der Oberfläche beeinflusst die Profile der anderen auf der Oberfläche adsorbierten Moleküle. Die Produktkonzentration im Gas, das aus dem Anodenkanal strömt, nimmt bei niedrigen Stromdichten mit steigender Stromdichte zu, wie auch im Experiment beobachtet worden ist.

Innerhalb einer SOFC-Batterie hängt das Verhalten jeder einzelnen Zelle von der Temperatur ihrer Umgebung ab (Randbedingung). Die Temperaturprofile von inneren und äußeren Zellen können sehr verschieden sein. Als Grenzfälle kann man dabei das unterschiedliche Verhalten innerhalb des SOFC-Stapels als isotherm bzw. adiabatisch betrachten. Darauf aufbauend untersucht Kapitel 7 den Einfluss der verschiedenen Betriebsbedingungen und geometrischen Parameter auf Temperatur- und Speziesverteilung, wie Stromdichte, reversible Potentiale, Überspannungen, Wirkungsgrad und Leistungsdichte. Insbesondere werden der Einfluss der Dicke der Anode, der spezifischen Katalysatorfläche, der Strömungsgeschwindigkeit der Luft, des Wasserdampf-Kohlenstoffverhältnisses (S/C) und der Vorreformierung eingehend diskutiert. Das Stromdichteprofil hängt sowohl stark von der örtlichen Temperatur als auch von der örtlichen Brennstoffzusammensetzung ab. Es konnte gezeigt werden, dass selbst bei brennstoffreichen Bedingungen der Einfluss der Temperatur stärker als der der Konzentration des Brennstoffs sein kann. Bei Reformierung innerhalb der SOFC kommt es zu einer Abkühlung am Eingang der Zellen, was auch die Simulation zeigt. Dies führt zu einem Abfall der Stromdichte. Eine erhebliche Änderung der Temperatur entlang der Zelle ist beobachtet worden. Die Temperatur entlang der Dicke der MEA ist jedoch fast uniform. Die Wandtemperatur der Kathodeseite ist aufgrund von Wärmestrahlung und der

Elektrodenamordnung höher als die Temperatur in der Gasphase des Kanals. Der Druckabfall über der Anode folgt im Wesentlichen der Stromdichte. Er wird hauptsächlich durch die Massenzunahme an der Dreiphasengrenze und die Diffusionslimitierung in dem porösen Material verursacht. Zonen mit einer hohen Stromdichte führen zu einem höheren lokalen Druckverlust. Die Oberflächenprofile entlang der Dreiphasengrenze zeigen, dass die Bedeckung mit atomaren Sauerstoff durch dissoziative Adsorption von Wasser aufgrund der zunehmenden Wasserproduktion entlang des Kanals steigt. Auch sind mit zunehmender Länge des Kanals mehr und mehr Adsorptionsplätze auf der Nickeloberfläche verfügbar. Eine vernachlässigbare Bedeckung mit Kohlenstoff kann nahe des Zelleingangs beobachtet werden. Jedoch sind all diese Tendenzen stark von der Brennstoffzusammensetzung abhängig.

Es wird allgemein akzeptiert, dass die interne Reformierung gegenüber externen, vorgeschalteten Reformern Kosten sparen kann und die Reformierung innerhalb der SOFC-Einheit oder sogar an der Anode selbst unter Ausnutzung der von der Zelle erzeugten Wärme erfolgen kann, was zu einer weiteren Erhöhung des Wirkungsgrades des Systems führt. Jedoch ist der Wirkungsgrad der einzelnen Zelle bei der Verwendung eines vorreformierten Brennstoffes höher. Der Wirkungsgrad ist insgesamt abhängig von der Zusammensetzung des Brennstoffgemisches, den Betriebsbedingungen und den Zellabmessungen.

Adiabatische und isotherme Betriebsweise führen zu auffallend unterschiedlichen Trends. Eine höhere Strömungs-geschwindigkeit der Luft führt bei adiabatischer Betriebsweise zu einer Abnahme der Leistungsdichte und Effizienz. Bei isothermer Betriebsweise hingegen führt eine Erhöhung des Luftflusses zu einer Erhöhung der Leistungsdichte und Effizienz. Für jede vorgegebene Brennstoffzusammensetzung gibt es bestimmte spezifische Katalysatoroberflächen und Anodendicken, bei denen die maximale Effizienz und Leistungsdichte erreicht werden. Die Verdünnung des Brennstoffes (variierende S/C-Verhältnisse) führt zu entgegengesetzten Trends bei Wirkungsgrad und Leistungsdichte. Diskutiert wird außerdem der Einfluss anderer Betriebsparameter wie der Strömungsgeschwindigkeit der Luft und der Grad der Vorreformierung. In Kapitel 8 werden die in dieser Dissertation vorgestellten Arbeiten zusammengefasst.

Appendix

Surface reaction mechanism

	Reaction	A^*(cm,mol,s)	β	E_a^*(kJ mol^{-1})
1.	H_2+NI(s)+NI(s)→H(s)+H(s)	$1.000\times10^{-02\dagger}$	0.0	0.00
2.	O_2+NI(s)+NI(s)→O(s)+O(s)	$1.000\times10^{-02\dagger}$	0.0	0.00
3.	CH_4+NI(s)→CH_4(s)	$8.000\times10^{-03\dagger}$	0.0	0.00
4.	H_2O+NI(s)→H_2O(s)	$0.100\times10^{-00\dagger}$	0.0	0.00
5.	CO_2+NI(s)→CO_2(s)	$1.000\times10^{-05\dagger}$	0.0	0.00
6.	CO+NI(s)→CO(s)	$5.000\times10^{-01\dagger}$	0.0	0.00
7.	H(s)+H(s)→NI(s)+NI(s)+H_2	$2.545\times10^{+19}$	0.0	81.21
8.	O(s)+O(s)→NI(s)+NI(s)+O_2	$4.283\times10^{+23}$	0.0	474.95
9.	CH_4(s)→CH_4+NI(s)	$8.705\times10^{+15}$	0.0	37.55
9.	H_2O(s)→H_2O+NI(s)	$3.732\times10^{+12}$	0.0	60.79
10.	CO_2(s)→CO_2+NI(s)	$6.447\times10^{+07}$	0.0	25.98
11.	CO(s)→CO+NI(s)	$3.563\times10^{+11}$	0.0	111.27
	$\theta_{CO(s)}$			-50.00‡
12.	H(s)+O(s)→OH(s)+NI(s)	$5.000\times10^{+22}$	0.0	97.90
13.	OH(s)+NI(s)→H(s)+O(s)	$1.781\times10^{+21}$	0.0	36.09
15.	H(s)+OH(s)→H_2O(s)+NI(s)	$3.000\times10^{+20}$	0.0	42.70
16.	H_2O(s)+NI(s)→H(s)+OH(s)	$2.271\times10^{+21}$	0.0	91.76
17.	OH(s)+OH(s)→H_2O(s)+O(s)	$3.000\times10^{+21}$	0.0	100.00
18.	H_2O(s)+O(s)→OH(s)+OH(s)	$6.373\times10^{+23}$	0.0	210.86
19.	C(s)+O(s)→CO(s)+NI(s)	$5.200\times10^{+23}$	0.0	148.10
20.	CO(s)+NI(s)→C(s)+O(s)	$1.354\times10^{+22}$	-3.0	116.12
	$\theta_{CO(s)}$			-50.00‡
21.	CO(s)+O(s)→CO_2(s)+NI(s)	$2.000\times10^{+19}$	0.0	123.60
	$\theta_{CO(s)}$			-50.00‡
22.	CO_2(s)+NI(s)→CO(s)+O(s)	$4.653\times10^{+23}$	-1.0	89.32
23.	HCO(s)+NI(s)→CO(s)+H(s)	$3.700\times10^{+21}$	0.0	0.00
	$\theta_{CO(s)}$			50.00‡
24.	CO(s)+H(s)→HCO(s)+NI(s)	$4.019\times10^{+20}$	-1.0	132.23
25.	HCO(s)+NI(s)→CH(s)+O(s)	$3.700\times10^{+24}$	-3.0	95.80
26.	CH(s)+O(s)→HCO(s)+NI(s)	$4.604\times10^{+20}$	0.0	109.97
27.	CH_4(s)+NI(s)→CH_3(s)+H(s)	$3.700\times10^{+21}$	0.0	57.70
28.	CH_3(s)+H(s)→CH_4(s)+NI(s)	$6.034\times10^{+21}$	0.0	61.58
29.	CH_3(s)+NI(s)→CH_2(s)+H(s)	$3.700\times10^{+24}$	0.0	100.00
30.	CH_2(s)+H(s)→CH_3(s)+NI(s)	$1.293\times10^{+22}$	0.0	55.33
31.	CH_2(s)+NI(s)→CH(s)+H(s)	$3.700\times10^{+24}$	0.0	97.10
32.	CH(s)+H(s)→CH_2(s)+NI(s)	$4.089\times10^{+24}$	0.0	79.18

	Reaction	A^*(cm,mol,s)	β	E_a^*(kJ mol^{-1})
33.	CH(s)+NI(s)→C(s)+H(s)	$3.700\times10^{+21}$	0.0	18.80
34.	C(s)+H(s)→CH(s)+NI(s)	$4.562\times10^{+22}$	0.0	161.11
35.	CH_4(s)+O(s)→CH_3(s)+OH(s)	$1.700\times10^{+24}$	0.0	88.30
36.	CH_3(s)+OH(s)→CH_4(s)+O(s)	$9.876\times10^{+22}$	0.0	30.37
37.	CH_3(s)+O(s)→CH_2(s)+OH(s)	$3.700\times10^{+24}$	0.0	130.10
38.	CH_2(s)+OH(s)→CH_3(s)+O(s)	$4.607\times10^{+21}$	0.0	23.62
39.	CH_2(s)+O(s)→CH(s)+OH(s)	$3.700\times10^{+24}$	0.0	126.80
40.	CH(s)+OH(s)→CH_2(s)+O(s)	$1.457\times10^{+23}$	0.0	47.07
41.	CH(s)+O(s)→C(s)+OH(s)	$3.700\times10^{+21}$	0.0	48.10
42	C(s)+OH(s)→CH(s)+O(s)	$1.625\times10^{+21}$	0.0	128.61

* Arrhenius parameters for the rate constant written in the form:

$$k = AT^{\beta}\exp(-E/RT)$$

† Sticking coefficient. For example in reaction (1), the value 0.01 is the initial sticking coefficient S_i^0 for the adsorption of H_2 on Ni surface. This can be converted to the conventional rate constant by Eq. 2.15. The initial sticking coefficient can also be modified by parameters β and E_a to account for the temperature dependency. In this case the initial sticking coefficient can be calculated from Eq. 2.14. For more details refer section section 2.2.1

‡ Coverage dependent activation energy. Order of the reaction and the activation energy can be made coverage dependent by using the parameters μ and ϵ in Eq. 2.4. For example reaction (20) has an additional coverage dependency on CO by -50kJ/mol, which means if the surface is completely covered with the species CO, then the activation energy of the reaction reduces by 50kJ/mol. In the case of reaction (20) the activation energy becomes 66.12 kJ/mol if the surface is completely covered with CO.

Total surface site density $\Gamma = 2.6 \times 10^{-9}$mol/cm^2

Bibliography

Bibliography

[1] Fluent Inc., Lebanon, NH 03766. Fluent user manual 6.1, www.fluent.com.

[2] O. Deutschmann, S. Tischer, C. Correa, D. Chatterjee, S. Kleditzsch, and V. M. Janardhanan. DETCHEM software package, 2.0 ed., www.detchem.com, Karlsruhe, 2004.

[3] J. Larminie and A. Dicks. Fuel cell systems explained. 2nd edition. John Wiley and Sons Ltd, West Sussex, England, 2003.

[4] K. A. Adamson, A. Baker, and D. Jollie. Opening doors to fuel cell commercialisation: Fuel cell systems: A survey of world wide activity. Technical Report, Fuel cell today 2004.

[5] A. Weber and E. I. Tiffée. Materials and concepts for solid oxide fuel cells (SOFCs) in stationary and mobile applications. *J. Power Sources* 127, (2004) 273–283.

[6] Y. Matsuzaki and I. Yasuda. Electrochemical properties of reduced temperature SOFCs with mixed ionic and electronic conductors in electrodes and/or interlayers. *Solid State Ionics* 152-153, (2002) 463–468.

[7] J. R. Wilson, W. Kobsiriphat, R. Mendoza, H. Y. Chen, J. M. Hiller, D. J. Miller, K. Thornton, P. W. Voorhees, S. B. Adler, and S. A. Barnett. Three-dimensional reconstruction of a solid-oxide fuel-cell anode. *Nature materials* 5, (2006) 541–544.

[8] R. N. Basu, G. Blass, H. P. Buchkremer, D. Stver, F. Tietz, E. Wessel, and I. C. Vinke. Simplified processing of anode-supported thin film planar solid oxide fuel cells. *J. European Ceramic. Soc.* 25, (2005) 463–471.

[9] P. Charpentier, P. Fragnauda, D. Schleicha, and E. Gehainb. Preparation of thin film SOFCs working at reduced temperature. *Solid State Ionics* 135, (2000) 373–380.

[10] W. Zhu and S. Deevi. A review on the status of anode materials for solid oxide fuel cells. *Materials Sci. Eng. A* 362, (2003) 228–239.

[11] A. Bieberle. The Electrochemistry of Solid Oxide Fuel Cell Anodes: Experiments, Modeling, and Simulations. Ph.D. thesis, Swiss Federal Institute of Technology 2000.

[12] EG&G Services Parsons, Inc.Science Applications International Corporation. Fuel Cell Handbook, 5th edition 2000.

[13] J. H. Koh, Y. S. Yoo, J. W. Park, and H. C. Lim. Carbon deposition and cell performance of Ni-YSZ anode support SOFC with methane fuel. *Solid State Ionics* 149, (2002) 157–166.

[14] B. A. Boukamp. The amazing perovskite anode. *Nature materials* 2, (2003) 294–296.

[15] S. Tao and J. T. Irvine. A redox-stable efficient anode for solid-oxide fuel cells. *Nature materials* 2, (2003) 320–323.

[16] S. McIntosh, H. He, S. Lee, O. C. Nunes, V. V. Krishnan, J. M. Vohs, and R. J. Gorte. An Examination of Carbonaceous Deposits in Direct-Utilization SOFC Anodes. *J. Electrochem. Soc.* 151, (2004) A604–A608.

[17] S. Lee, J. M. Vohs, and R. J. Gorte. A study of SOFC anodes based in Cu-Ni and Cu-Co bimetallics in CeO_2-YSZ. *J. Electrochem. Soc.* 151, (2004) A1319–A1323.

[18] E. P. Murray, T. Tsai, and S. A. Barnett. A direct-methane fuel cell with a ceria-based anode. *Nature* 400, (1999) 649–651.

[19] N. Nagakawa, H. Sagara, and K. Kato. Catalytic activity of Ni-YSZ-CeO_2 anode for the steam reforming of methane in a direct internal reforming solid oxide fuel cell. *J. Power Sources* 92, (2001) 88–94.

[20] A. C. Co, S. J. Xia, and V. I. Birss. A kinetic study of oxygen reduction reaction at $LaSrMnO_3$-YSZ composite electrodes. *J. Electrochem. Soc.* 152, (2005) A570–A576.

[21] E. Maguire, B. Gharbage, F. Marquesb, and J. Labrinchab. Cathode materials for intermediate temperature SOFCs. *Solid State Ionics* 127, (2000) 329–335.

[22] H. Tu and U. Stimming. Advances, aging mechanisms and lifetime in solid-oxide fuel cells. *J. Power Sources* 127, (2004) 284–293.

[23] T. Tsai and S. A. Barnett. Effect of LSM-YSZ cathode on thin-electrolyte solid oxide fuel cell performance. *Solid State Ionics* 93, (1997) 207–217.

[24] M. Juhl, S. Primdahl, C. Manon, and M. Mogensen. Performance/structure correlations for composite SOFC cathodes. *J. Power Sources* 61, (1996) 173–181.

[25] R. Williford and P. Singh. Engineered cathodes for high performance SOFCs. *J. Power Sources* 128, (2004) 45–53.

[26] P. Holtappels and C. Bagger. Fabrication and performance of advanced multi-layer SOFC cathodes. *J. European Cerm. Soc.* 22, (2002) 41–48.

[27] S. Jiang. Issues on development of (La,Sr)MnO3 cathode for solid oxide fuel cells. *J. Power Sources* 124, (2003) 390–402.

[28] S. P. S. Badwal, R. Deller, K. Foger, Y. Ramprakash, and J. P. Zhang. Interaction between chromia forming alloy interconnects and air electrode of solid oxide fuel cells. *Solid State Ionics* 99, (1997) 297–310.

[29] W. Zhu and S. Deevi. Opportunity of metallic interconnects for solid oxide fuel cells: a status on contact resistance. *Mat. Research Bulletin* 38, (2003) 957–972.

[30] T. Ishihara and N. M. S. abd O. Yamamoto. High temperature solid oxide fuel cells fundamentals, design and applications. Elsvier, Amsterdam, The Netherlands, 2003.

[31] W. Zhu and S. Deevi. Development of interconnect materials for solid oxide fuel cells. *Mat. Sci. Eng. A* 348, (2003) 227–243.

[32] J. W. Fergus. Metallic interconnects for solid oxide fuel cells. *Mat. Sci. Eng. A* 397, (2005) 271–283.

[33] L. Jian, P. Jian, X. Guangyuanb, W. Shunxu, and X. Jianzhong. Heat resistant alloys as interconnect materials of reduced temperature SOFCs. *J. Power Sources* 157, (2006) 368–376.

[34] J. W. Fergus. Lanthanum chromite-based materials for solid oxide fuel cell interconnects. *Solid State Ionics* 171, (2004) 1–15.

[35] Z. Zeng and K. Natesan. Corrosion of metallic interconnects for SOFC in fuel gases. *Solid State Ionics* 167, (2004) 9–16.

[36] Y. Matsuzaki and I. Yasuda. Electrochemical properties of a SOFC cathode in contact with a chromium-containing alloy separator. *Solid State Ionics* 132, (2000) 271–278.

[37] A. Atkinson, S. Barnett, R. J. Gorte, J. T. S. Irvine, A. J. Mcevoy, M. Mogensen, S. C. Sighal, and J. Vohs. Advanced anodes for high-temperature fuel cells. *Nature* 3, (2004) 17–27.

[38] J. Liu and S. A. Barnett. Operation of anode-supported solid oxide fuel cells on methane and natural gas. *Solid State Ionics* 158, (2003) 11–16.

[39] Y. Lin, Z. Zhan, J. Liu, and S. A. Barnett. Direct operation of solid oxide fuell cells with methane fuel. *Solid State Ionics* 176, (2005) 1827–1835.

[40] Z. Zhan and S. A. Barnett. A octane fueled solid oxide fuel cell. *Science* 308, (2005) 844–847.

[41] B. C. H. Steele. Running on natural gas. *Nature* 400, (1999) 619–621.

[42] N. M. Sammes, R. J. Boersma, and G. A. Tompsett. Micro SOFC system using butane fuel. *Solid State Ionics* 135, (2000) 487–491.

[43] T. Hibino, A. Hashimoto, K. Asano, M. Yano, M. Suzuki, and M. Sano. An intermediate temperature solid oxide fuel cell providing high performance with hydrocarbons than with hydrogen. *Electrochem. Solid State Lett.* 5, (2002) A242–A244.

[44] Z. Shao, S. M. Haile, J. Ahn, P. D. Ronney, Z. Zhan, and S. A. Barnett. A thermally self sustained micro solid oxide fuel cell stack with high power density. *Nature* 435, (2005) 795–798.

[45] R. M. Ormerod. High temperature solid oxide fuel cells fundamentals design and applications. Elsevier, 2003.

[46] B. Feng, C. Y. Wang, and B. Zhu. Catalysts and performances for direct methanol low temperature (300-600°C) solid oxide fuel cell. *Electrochem. Solid State Lett.* 9, (2006) A80–A81.

[47] G. O. Lauvstad, R. Tunold, and S. Sunde. Electrochemical oxidation of CO on Pt and Ni point electrodes in contact with an yttria- stabilized zirconia electrolyte. *J. Electrochem. Soc.* 149, (2002) E497–E505.

[48] Y. Matsuzaki and I. Yasuda. Electrochemical oxidation of H_2 and CO in a H_2-H_2O-CO-CO_2 system at the interface of a Ni-YSZ cermet electrode and YSZ electrolyte. *J. Electrochem. Soc.* 147, (2000) 1630–1635.

[49] S. P. Jiang and S. P. S. Badwal. Hydrogen oxidationat the Nickel and Platinum electrodes on Yttria-Tetragonal Zirconia electrolyte. *J. Electrochem. Soc.* 144, (1997) 3777–3784.

[50] E. A. Liese and R. S. Gemmen. Performance comparison of internal reforming against external reforming in a solid oxide fuel cell, gas turbine hybrid system. *ASME* 127, (2005) 86–90.

[51] K. Kendall. Hopes for a flame-free future. *Nature* 404, (2000) 233–235.

[52] C. M. Finnerty, N. J. Coe, R. H. Cunningham, and R. M. Ormerod. Carbon formation on and deactivation of nickel-based/zirconia anodes in solid oxide fuel cells running on mehtane. *Catalysis Today* 46, (1998) 137–145.

[53] Z. Cheng, S. Zha, L. Aguilar, and D. Wand. A solid oxide fuel cell running on H_2S/CH_4 fuel mixtures. *Electrochem. Solid State Lett.* 9, (2006) A31–A33.

[54] B. C. H. Steele and A. Heinzel. Materials for fuel-cell technologies. *Nature* 414, (2001) 345–352.

[55] R. A. van Santen and M. Neurock. Molecular heterogeneous catalysis. WILEY-VCH Verlag GmbH & Co. KGaA, Weinheim, 2006.

[56] R. J. Kee, M. E. Coltrin, and P. Blarborg. Chemically reacting flow. John Wiley & Sons, Inc, 2003.

[57] T. Takeguchi, R. Kikuchi, T. Yano, K. Eguchi, and K. Murata. Effect of precious metal addition to Ni-YSZ cermet on reforming of CH_4 and electrochemical activity as SOFC anode. *Catalysis Today* 84, (2003) 217–222.

[58] S. H. Clarke, A. L. Dicks, K. Pointon, T. A. Smith, and A. Swann. Catalytic aspects of steam reforming of hydrocarbons in internal reforming fuel cells. *Catalysis Today* 38, (1997) 411–423.

[59] H. Timmerman, D. Fouquet, A. Weber, E. I. Tiffée, U. Hennings, and R. Reimert. Internal reforming of methane at Ni/YSZ and Ni/CGO SOFC cermet anodes. *Fuel Cells* 6, (2006) 307–313.

[60] M. L. Toebes, J. H. Bitter, A. J. Dillen, and K. P. Jong. Impact of structure and reactivty of nickel particles on the catalytic growth of carbon nanofibers. *Catalysis Today* 76, (2002) 33–42.

[61] I. Alstrup and M. Teresa Tavares. The kinetics of carbon formation from CH4 + H2 on a silica-supported nickel catalyst. *Journal of Catalysis* 135, (1992) 147–155.

[62] J. Xu and G. F. Froment. Methane stean reforming, Methanation and water-gas shift: I Intrinsic kinetics. *AIChE J.* 35, (1989) 88–95.

[63] J. Xu and G. F. Froment. Methane stean reforming II: Diffusional limitaions and reactor simulation. *AIChE J.* 35, (1989) 97–103.

[64] E. S. Hecht, G. K. Gupta, H. Zh, A. M. Dean, R. J. Kee, L. Maier, and O. Deutschmann. Methane reforming kinetics within a Ni-YSZ SOFC anode support. *Appl. Catal. A. General* 295, (2005) 40–51.

[65] J. Zhu, J. G. Ommen, and L. Lefferts. Reaction scheme of partial oxidation of methane to synthesis gas over yttrium-stabilized zirconia. *J. Catalysis* 225, 388–397.

[66] A. M. Sukeshini, B. Habibzadeh, B. P. Becker, C. A. Stoltz, B. W. Eichhorn, and G. S. Jackson. Electrochemical oxidation of H_2, CO, and CO/H_2 mixtures on patterned Ni anodes on YSZ electrolytes. *J. Electrochem. Soc.* 153, (2006) A705–A715.

[67] J. Mizusaki, H. Tagawa, T. Saito, T. Yamamura, K. Kamitani, K. Hirano, S. Ehara, T. Takagi, T. Hikita, M. Ippommatsu, S. Nakagawa, and K. Hashimoto. Kinetics of the reaction at the nickel pattern electrode on YSZ in H_2-H_2O atmospheres. *Solid State Ionics* 70-71, (1994) 52–58.

[68] P. Holtappels, I. C. Vinke, L. G. J. de Haart, and U. Stimming. Reaction of hydrogen/water mixtures on nickel-zirconia cermet electrodes: II AC polarization characteristics. *J. Electrochem. Soc.* 146, (1999) 2976–2982.

[69] B. de Boer. SOFC Anode: hydrogen oxidation at porous nickel and nickel/yttria stabilized zirconia cermet electrodes. Ph.D. thesis, University of Twente, The Netherlands 1998.

[70] M. Vogler, W. G. Bessler, J. Warnatz, A. Bieberle, and L. J. Gauckler. Towards an understanding of Ni anodes in solid oxide fuel cells: Electrochemical modeling and experimental validation using patterned anodes. In 7th European SOFC Forum, Lucerne, Switzerland. 2006 .

[71] W. G. Bessler, D. G. Goodwin, and J. Warnatz. The influence of equilibrium potential on electrochemical kinetics of SOFC anodes. In 7th European SOFC Forum, Lucerne, Switzerland. 2006 .

[72] A. Bieberle, L. P. Meier, and L. J. Gauckler. The Electrochemistry of Ni Pattern Anodes Used as Solid Oxide Fuel Cell Model Electrodes. *J. Electrochem. Soc.* 148, (2001) A646–A656.

[73] H. Zhu, R. J. Kee, V. M. Janardhanan, O. Deutschmann, and D. G. Goodwin. Modeling elementary heterogeneous chemistry and electrochemistry in solid oxide fuel cells. *J. Electrochem. Soc.* 152, (2005) A2427–A2440.

[74] V. M. Janardhanan and O. Deutschmann. CFD analysis of solid oxide fuel cell with internal reforming: coupled interaction of transport, heterogeneous catalysis and electrochemical processes. *J. Power Sources* 162, (2006) 1192–1202.

[75] P. Costamagna, A. Selimovic, M. D. Borghi, and G. Agnew. Electrochemical model of the integrated planar oxide fuel cell (IP-SOFC). *Chem. Engg. Journal* 102, (2004) 61–69.

[76] S. Chan, K. Khor, and Z. Xia. A complete polarization model of a solid oxide fuel cell and its sensitivity to the change of cell component thickness. *J. Power Sources* 93, (2000) 130–140.

[77] R. J. Kee, H. Zhu, and D. G. Goodwin. Modeling electrochemistry and solid oxide fuel cells: II Research challenges. *J. Comb. Soc. Japan* 47, (2005) 276–289.

[78] H. Zhu and R. J. Kee. A general mathematical model for analyzing the performance of fuel-cell membrane-electrode assemblies. *J. Power Sources* 117, (2003) 61–74.

[79] W. G. Bessler. Gas concentration impedance of solid oxide fuel cell anodes. I. Stagnation point flow geometry. *J. Electrochem. Soc.* (in press).

[80] T. L. Nguyen, T. Honda, T. Kato, Y. Iimura, K. Kato, A. Negishi, K. Nozaki, M. Shiono, A. Kobayashi, K. Hosoda, Z. Cai, and M. Dokiya. Fabrication and characterisation of anod supported tubular SOFCs with zirconis based electrolyte for reduced temperature operation. *J. Electrochem. Soc.* 151, (2004) A1230–A1235.

[81] P. Aguiara, C. Adjimana, and N. Brandona. Anode-supported intermediate temperature direct internal reforming solid oxide fuel cell. I: model-based steady-state performance. *J. Power Sources* 138, (2004) 120–136.

[82] A. J. Bard and L. R. Faulkner. Electrochemical methods fundamentals and applications. John Wiley & Sons, Inc, 2001.

[83] S. H. Chan, X. J. Chen, and K. A. Khor. Cathode micromodel of solid oxide fuel cell. *J. Electrochem. Soc.* 151, (2004) A164–A172.

[84] R. E. Williford, L. A. Chick, G. D. maupin, and S. P. Simner. Diffusion limitations in porous anodes of SOFCs. *J. Electrochem. Soc.* 150, (2003) A1067–A1072.

[85] S. Chan, X. Chen, and K. Khor. A simple bilayer electrolyte model for solid oxide fuel cells. *Solid State Ionics* 158, (2003) 29–43.

[86] C. W. Tanner and A. V. Virkar. A simple model for interconnect design of planar solid oxide fuel cells. *J. Power Sources* 113, (2003) 44–56.

[87] Z. T. Xia, S. H. Chan, and K. A. Khor. An Improved Anode Micro Model of SOFC. *J. Electrochem. Soc.* 7, (2004) A63–A65.

[88] P. W. Li, L. Schaefer, and M. K. Chyu. A Numerical Model Coupling the Heat and Gas Species Transport Processes in a Tubular SOFC. *J. Heat Transfer* 126, (2004) 219–229.

[89] J. Billingham, A. C. King, R. C. Copcutt, and K. Kendall. Analysis of a model for a loaded, planar, solid oxide fuel cell. *J. Appl. Math* 60, (2000) 574–601.

[90] K. Keegan, M. Khaleel, L. Chick, K. Recknagle, S. Simner, and J. Deibler. Analysis of a Planar Solid Oxide Fuel Cell Based Automotive Auxiliary Power Unit. Technical Report, SAE, 2002-01-0413 2002.

[91] A. Burt, I. Celik, R. Gemmenb, and A. Smirnov. A numerical study of cell-to-cell variations in a SOFC stack. *J. Power Sources* 126, (2004) 76–87.

[92] P. Aguiar, C. Adjiman, and N. Brandon. Anode-supported intermediate-temperature direct internal reforming solid oxide fuel cell II. Model-based dynamic performance and control. *J. Power Sources* 147, (2005) 136–147.

[93] N. Autissier, D. Larrain, J. V. Herle, and D. Favrat. CFD simulation tool for solid oxide fuel cells. *J. Power Sources* 131, (2004) 313–319.

[94] M. Lockett, M. Simmons, and K. Kendall. CFD to predict temperature profile for scale up of micro-tubular SOFC stacks. *J. Power Sources* 131, (2004) 243–246.

[95] A. Selimovic, M. Kemm, T. Torisson, and M. Assadi. Steady state and transient thermal stress analysis in planar solid oxide fuel cells. *J. Power Sources* 145, (2005) 463–469.

[96] K. P. Recknagale, R. E. Williford, L. A. Chick, D. R. Rector, and M. A. Khaleel. Three-dimensional thermo-fluid electrochemical modeling of planar SOFC stacks. *J. Power Sources* 113, (2003) 109–114.

[97] R. Krishna. Problems and pitfals in the use of the Fick formulation for intraparticle diffusion. *Chem. Engg. Sci.* 48, (1993) 845–861.

[98] P. Schneider. Multicomponent isothermal diffusion and forced flow of gases in capillaries. *Chem. Engg. Sci.* 33, (1978) 1311–1219.

[99] M. Novak, K. Ehrhardt, K. Klausacek, and P. Schneider. Dynamics of non-isobaric diffusion in porous catalysts. *Chem. Engg. Sci.* 43, (1988) 185–193.

[100] R. B. Bird, W. E. Stewart, and E. N. Lightfoot. Transport phenomena. 1st edition. John Wiley & Sons, 1960.

[101] R. J. Kee, G. Dixon-Lewis, J. Warnatz, M. E. Coltrin, and J. A. Miller. A fortran computer code package for the evaluation of gas-phse multicomponent transport properties. Technical Report, Sandia report, SAND86-8246 1986.

[102] R. Krishna. A simplified procedure for the Solution of dusty gas model equations for steady state transport in non-reacting systems. *Chem. Eng. J* 35, (1987) 75–81.

[103] J. Baer. Dynamics of Fluids in Porous Media. American Elsevier, New York, 1972.

[104] R. Jackson. Transport in porous catalysts. Elsevier, Amsterdam, 1977.

[105] E. A. Mason and A. P. Malinauskas. Gas transport in porous media, The Dusty Gas Model. Elsevier, Amsterdam, 1983.

[106] E. A. Manson, A. P. Malinaskus, and R. B. Evans. Flow and diffusion of gases in porous media. *J. Chem. Phys.* 46, (1967) 3199–3216.

[107] R. B. Evans and G. M. Watson. Gaseous diffusion in porous media, effects of pressure gradients. *J. Chem. Phys.* 36, (1962) 1894–1902.

[108] D. Arnost and P. Schneider. Dynamic transport of multicomponent mixtures of gases in porous solids. *Chem. Eng. J* 57, (1995) 91–99.

[109] R. E. Hayes and S. T. Kolaczkowski. Introduction to catalytic combustion. Gordon and Breach Science Publishers, Amsterdam, 1997.

[110] D. L. Damm and A. G. Fedorov. Radiation heat transfer in SOFC materials and components. *J. Power Sources* 143, (2005) 158–165.

[111] D. L. Damm and A. G. Fedorov. Spectral Radiative Heat Transfer Analysis of the Planar SOFC. *ASME* 2, (2005) 258–262.

[112] S. Murthy and A. G. Fedorov. Radiation heat transfer analysis of the monolith type solid oxide fuel cell. *J. Power Sources* 124, (2003) 453–458.

[113] J. D. J. VanderSteen and J. G. Pharoah. Modeling Radiation Heat Transfer With Participating Media in Solid Oxide Fuel Cells. *ASME* 62, (2006) 62–67.

[114] Z. Shao and S. M. Haile. A high performance cathode for next generation solid oxide fuel cells. *Nature* 431, (2004) 170–173.

[115] F. Zhao and A. V. Virkar. Dependence of polarization in anode supported solid oxide fuel cells on various cell parameters. *J. Power Sources* 141, (2005) 79–95.

[116] M. Ihara, A. Abudula, H. Komiyama, and K. Yamada. Anodic reaction mechanism determining the threshold current density for the CO_2 production in SOFC with dry methane fuel. In B. Thorstensen, ed., 2nd European SOFC Forum, Oslo/Norway, volume 2. 1996 637–646.

[117] P. Deuflhardt, E. Hairer, and J. Zugk. One step and extrapolation methods for differential-algebraic systems. *Numerische Mathematik* 51, (1987) 501–516.

[118] H. Zhu and R. J. Kee. Thermodynamics of SOFC efficiency and fuel utilization as functions of fuel mixtures and operating conditions. *J. Power Sources* 161, (2006) 957–964.

[119] E. Gorbova, A. Demin, B. Zhuravlev, and P. Tsiakaras. Peculiarities of a charge transport in a co-ionic electrolyte. In Proceedings of International Hydrogen Energy Congress and Exhibition. 2005 .

[120] Y. Jiang and A. V. Virkar. Fuel composition and diluent effect on gas transport and performance of anode supported SOFCs. *J. Electrochem. Soc.* 150, (2003) A942–A951.

[121] J. Hartvigsen, S. Elangovan, and A. Khandkar. Selection of SOFC stack operating point for optimal balance of efficiency and power. In P. Stevens, ed., 3rd European solid oxide fuel cell forum, Nates-France. 1998 517–524.

[122] J. Braun, T. Hauber, H. Többen, J. Windmann, P. Zacke, D. Chatterjee, C. Correa, O. Deutschmann, L. Maier, S. Tischer, and J. Warnatz. Three-dimensional simulation of the transient behavior of a three-way catalytic converter. *SAE Technical paper 2002-01-0065* .

[123] S. Tischer and O. Deutschmann. Recent advances in numerical modeling of catalytic monolith reactors. *Catalysis Today* 105, (2005) 407–413.

Index

Index